NUMERICAL ANALYSIS AND WIND TUNNEL VALIDATION OF WIND DEFLECTORS FOR ROOFTOP SOLAR PANEL RACKS

by

Michael Yatsco

Submitted in Partial Fulfillment of the Requirements

for the Degree of

Master of Science

in the

Mechanical Engineering

Program

YOUNGSTOWN STATE UNIVERSITY

May, 2011

NUMERICAL ANALYSIS AND WIND TUNNEL VALIDATION OF WIND DEFLECTORS FOR ROOFTOP SOLAR PANEL RACKS

By

Michael Yatsco

I hereby release this thesis to the public. I understand that this thesis will be made available from the OhioLINK ETD Center and the Maag Library Circulation Desk for public access. I also authorize the University or other individuals to make copies of this thesis as needed for scholarly research.

Signature:

Michael Yatsco, Student Date

Approvals:

Dr. Yogendra Panta, Thesis Advisor Date

Dr. Ganesh Kudav, Thesis Advisor Date

Dr. Hazel Marie, Committee Member Date

Dr. Peter J. Kasvinsky, Dean of School of Graduate Studies and Research Date

ABSTRACT

Solar power since the past decade has become one of the very promising energy alternatives to the non-renewable forms of energy such as coal and natural gas. Solar panels that harvest solar power do not require the amount of space compared to other forms of renewable energy like wind turbines. In addition, solar panels have virtually an unlimited source of power derived from the sun and it can even be installed on the rooftops of buildings. One problem that arises with the placement of solar panel racks on the rooftops of buildings is occasional high wind loads the racks experience, requiring an efficient and optimized wind management system, sometimes known as wind deflectors. Wind deflectors not only prevent the solar panels from wind loads, but also ensure the safety of civilians and the surrounding property. This thesis employs the combinatorial utilization of experimental wind tunnel tests to validate the computational fluid dynamics (CFD) code embedded in ANSYS Fluent Software for analysis, design, and optimization of the wind deflector. The work in this thesis includes the consideration and detailed analysis of wind loads on the solar panels due to high wind speeds, leading to the design of an optimized wind deflector to prevent such loads. Research study comprehends physical modeling, mathematical modeling, and numerical simulation validated by wind tunnel tests to analyze the wind loads on scaled models. Extensive experimental data and simulation results were thoroughly analyzed and it was concluded that an elliptic-profiled wind deflector with fins positioned before the solar panels can reduce the wind loads by approximately 50%.

ACKNOWLEDGEMENTS

I would like to thank all the people that helped make the attainment of this Master's degree possible. It would not have been possible without their help. First and foremost I would like to thank my thesis advisors Dr. Yogendra Panta and Dr. Ganesh Kudav for their guidance and insight during my research and the writing of my thesis. Because of them, I had the chance to work with state of the art equipment and gaining real world experience while pursuing my Master's degree. The knowledge that I gained utilizing this equipment helped me to obtain a full-time job in the summer of 2010. Also, without their help I would not have been able to attend graduate school and for that I am extremely grateful. More specifically, I would like to thank Dr. Panta for the time he spent for editing and proofreading my thesis and helping me to develop better writing skills and technical figures. His insight and thoughtful responses have been extremely beneficial in the completion of this thesis. I have learned a great deal from his wealth of knowledge in the subject matter and I look to improve upon the lessons that I have learned in my future activities.

I would like to thank Dr. Hazel Marie for being in my thesis committee and for being instrumental in my studies as I pursued my undergraduate and graduate degrees. I would like to thank the chair of the Mechanical Engineering Department, Dr. Daniel Suchora. His help with my acceptance into the program enabled me to achieve my goal of attending graduate school and obtaining a Master's in Mechanical Engineering. I would also like to thank Maureen Brajer for her help with making my transition from an undergraduate to a graduate student, as seamless and painless as possible. I would like to

thank Mark Harvey for his role as my undergraduate assistant for my research. He was instrumental in getting me up to speed with the computer software. His help with both the numerical simulations and wind tunnel experiments was greatly appreciated. I would not have been able to do it alone. I am deeply thankful to Drs. Panta and Kudav for providing me financial support through their research grant on "*Estimation of lift-loads on inclined roof-top solar panel and measures to reduce such loads*" with Northern States Metals Inc. for my graduate study.

Last, but not least, I would like to thank my parents: Mom, Dad, and Rich. I would not be the person I am today if it was not for them pushing me to realize my full potential and supporting me in my endeavors. Thank you.

Thank you all from the bottom of my heart!

TABLE OF CONTENTS

LIST OF FIGURES

LIST OF TABLES

NOMENCLATURE

$\vec{A}$	Surface area vector
$\vec{A}_f$	Area of face, f
$\frac{\partial \rho}{\partial t}$	Rate of change of density within the control volume
∇	Vector operator in Cartesian coordinates $= \frac{\partial}{\partial x}\hat{i} + \frac{\partial}{\partial y}\hat{j} + \frac{\partial}{\partial z}\hat{k}$
$\nabla \cdot \left(\rho \vec{V}\right)$	Net flow across boundaries of the control volume
$\nabla \phi_f$	Gradient of ϕ at face f
dF_{Bi}	Differential body force component
f	Face of a meshed cell
F_{RD}	Respective drag or lift force for rack models with a deflector
F_R	Respective drag or lift force for models without a deflector
F_{CFD}	Respective CFD result for drag or lift force
F_{EXP}	Respective experimental result for drag or lift force
Γ_ϕ	Diffusion coefficient for ϕ
G_k	Generation of turbulent kinetic energy due to the mean velocity gradient
G_b	Generation of turbulent kinetic energy due to buoyancy
N_{faces}	Number of faces enclosing cell

p	Local thermodynamic pressure
ρ	Density
ϕ_f	Value of ϕ convected through face, f
$\rho_f \vec{v}_f \cdot \vec{A}_f$	Mass flux through the face, f
S_k	User defined source term
S_ε	User defined source term
S_ϕ	Source of ϕ per unit volume
S_{Mi}	Momentum source term component
σ_{ii}	Normal viscous stress terms
τ_{ij}	Shear viscous stress terms
u, v, w	x-, y-, and z-components of the velocity, respectively
$\vec{V}$	Total velocity vector of the fluid
μ	Dynamic or absolute viscosity of the fluid
μ_t	Turbulent viscosity
V	Cell volume
υ	Kinematic viscosity
$\vec{v}$	Velocity vector
Y_M	Contribution of the fluctuating dilatation in compressible turbulence to the overall dissipation rate

CHAPTER 1

INTRODUCTION

Energy consumption is increasing on a daily basis. The energy production comes from multiple forms of renewable and nonrenewable sources. According to the U.S. Energy Information Administration (EIA), the U.S. produced more than 4.1 billion kWh of electricity in 2008. This production includes both, renewable and nonrenewable forms of energy. From the 4.1 billion kWh of energy that was produced, more than 90% of the energy came from nonrenewable sources, with the remaining 10% of energy being produced from renewable sources. Natural gas and coal were the main fuels used for energy production; the two sources combined for more than 69% of the net energy production. **Figure 1.1** displays the breakdown of the U.S. energy production from the different sources. One of the big drawbacks to the use of nonrenewable fuels for energy production is the pollution from the burning and combustion of these sources. The pollution comes in the form of NO_x, SO_2, and CO_2 emissions; known as the by-products of a combustion reaction. The restrictions that are placed on companies are only going to get stricter as time goes on. Economic, reliable, efficient, and renewable forms of energy are desired as the populations, technologies, and economies of the world grow. Some of the main energy sources presently used throughout the world are detrimental to the environment and are non-renewable. As the restrictions on greenhouse gas emissions become more stringent, the price for these sources will increase as a result of newer and

more advanced technologies are utilized to combat these emissions. These circumstances put focus on developing cleaner, more efficient, and renewable forms of energy. Also, as the sources of energy become depleted, the price for these fuels will increase. One such form of renewable energy is solar power, which can be captured by solar panels. Coupled with the fact that solar panels have virtually no environmental impact, they are very attractive renewable sources [Spratley, 1998].

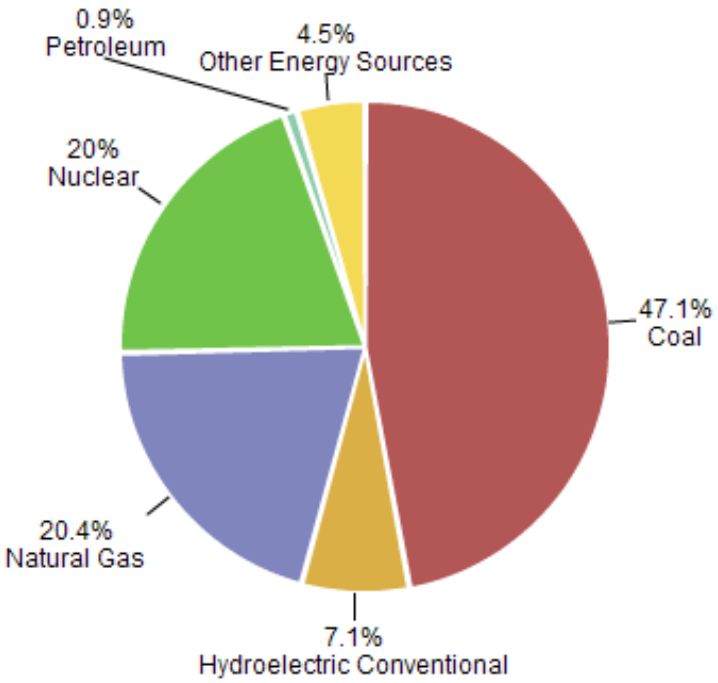

Figure 1.1 Energy production breakdown in the United States for the various forms of energy [U.S. - EIA, 2011].

There are multiple ways to mount solar panels, but the two most common are to the ground or on the roof. Problems with ground-mounted solar panel racks, is the need for land, which, in turn, costs additional money. The more logical and money saving option would be to mount the solar panel racks on the roof of a building. Not only does this reduce the need for additional land, but it enables the solar panels to be installed in

densely populated locations where space is at a premium. Another advantage of installing the racks on the roof is the ease of installation. There is no need to dig holes for the support beams for the solar panel racks, which would be needed if the racks were installed on the ground. The solar panel racks can be installed on any type of roof such as tar, gravel, or rubber. Obviously, the installation would have to coincide with local and state building codes. Although, there are many advantages to using solar panels, there are still a couple of drawbacks. One of the drawbacks is the investment payback around five to ten years depending on the size and location of the installation. Another disadvantage is the lack of research for renewable energies; renewable energy sources have only started to become popular since the last decade. Given that the popularity has increased, the use of advanced engineering methods, techniques, and analysis has followed suit. Also, it is required by law that the use of any type of addition, modification, construction, or object that will be used for public use needs to be deemed safe via a building permit.

There are many factors that draw attention and demand for the research of solar panel racks. One factor is the surrounding environment in which the solar panel racks will be installed, but more specifically, the magnitude and direction of wind the racks will experience. Depending on the location and the position of the solar panel racks, the magnitude of the wind speed and direction will vary. **Figure 1.2** is a maximum wind map of the United States.

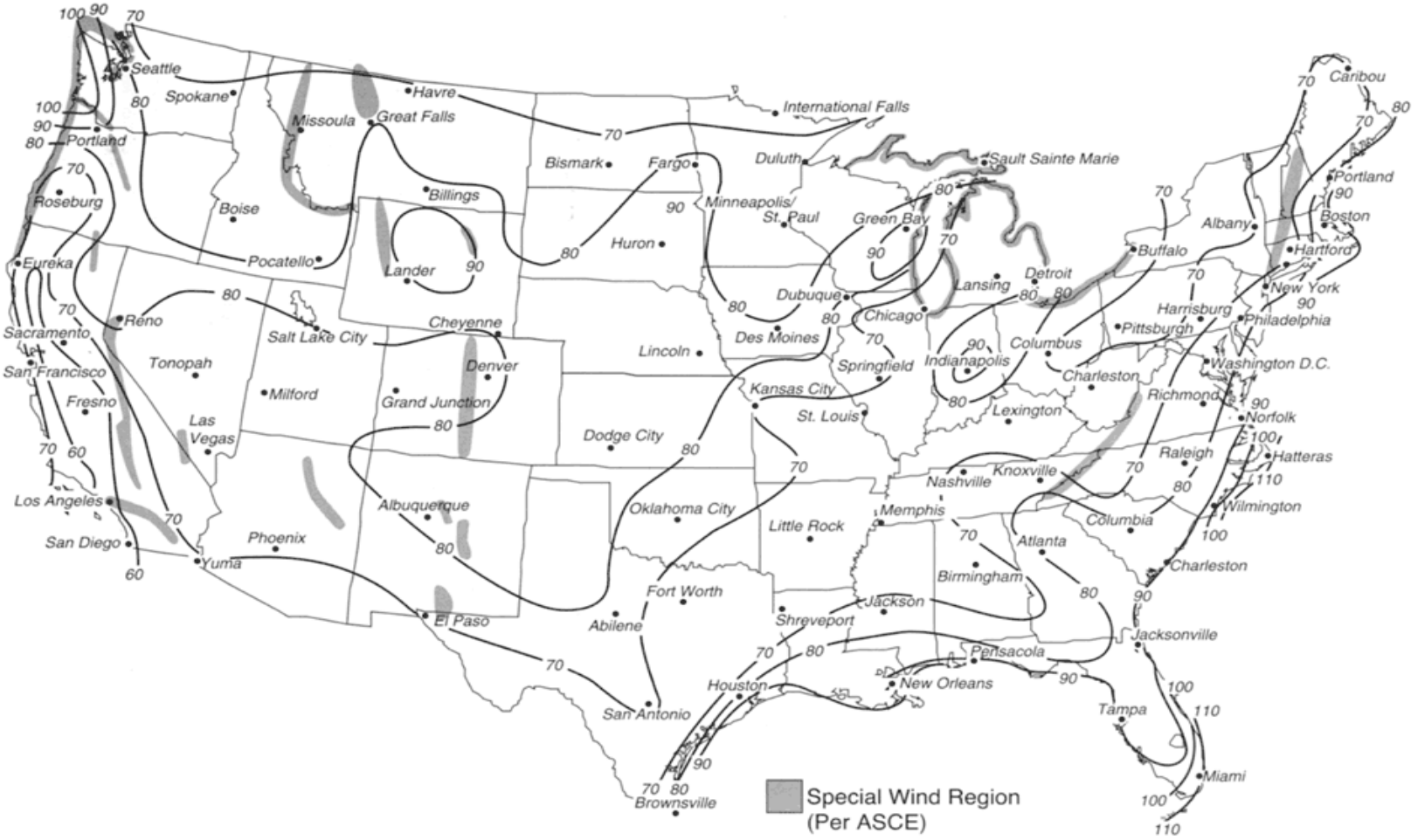

Figure 1.2 Maximum Wind map of the United States for the contiguous 48 states

1.2 Maximum Wind map of the United States for the contiguous 48 states [NAFCO

There are two main and often used ways to investigate the high speed effects on the solar packs. These two methods include experimental and computational analyses. The experimental method, in the case of this thesis work, involves wind tunnel analysis and computer validation. The two positives to using wind tunnel experimentation to do investigations is the fact that wind tunnels have been proven and used for a long time and is more accurate than computational analysis. The drawbacks to using a wind tunnel are the price, size, and set-up of a wind tunnel experiment. Not only is it expensive to build a wind tunnel, but the test itself can be very expensive. Also, depending on the scale of the test model, it can take multiple hours or days to set-up a wind tunnel test. However, in recent years computational computer programs have grown in popularity due to their ease of use, speed, and ability to handle complex geometries. One negative aspect about the use of computational programs is the fact that it is a fairly new technology and still needs to be validated like wind tunnel analysis.

1.1 Literature Review

The purpose of this section is to discuss several articles that were reviewed for the construction of this thesis. The primary focus of this thesis was to investigate the aerodynamic forces such as lift and drag over solar panel racks and to develop an optimized wind management system to reduce these forces. Scientists and engineers have used experimental methods and numerical techniques in order to determine the forces on aeronautical systems, automobiles, and other photovoltaic systems, otherwise known as solar panels.

An existing photovoltaic (PV) system installed on the top of Federal Office Building located in Carbondale, Illinois was studied earlier [Gong and Kulkarni, 2004]. The goal of their research was to optimize the current system that has been in place since 1978. The authors examined two parameters in order to optimize the current system. The two parameters were the array surface tilt angle and size. The optimum angle of tilt at the time of the PV system installation was determined to be 42^{o}. Further they made the surface tilt of the PV array equal to that of the location latitude as suggested by another study [Mathew, 1983]; the latitude for Carbondale, Illinois is $37^{o}46'$. Later this information was widely used to study surface tilt angles from 22^{o} to 48^{o} [Gong and Kulkarni, 2004]. It should also be noted that the azimuth angle is the position of the PV array with respect to true north, south, east, and west coordinates. The optimum surface tilt angle was determined by tracking the monthly PV output for the range of angles stated above. **Figure 1.3** displays the way the azimuth angle is measured with respect to the object in question. The PV output did increase as the tilt angle increased, but during the summer months, it was found that the PV output decreased once the tilt angles passed 30^{o}. Based on this information, the two authors concluded that the optimum surface tilt angle for PV output was 30^{o}; which is close to the latitude for Carbondale, Illinois.

A previous study reported several wind tunnel experiments were successfully conducted to analyze wind uplift on scaled, commercial solar panel models [Chung et al., 2006]. The study considered some parameters such as the lifted solar panel model and an installed guide plate. The parameters were tested at various wind speeds, ranging from 20 m/s to 50 m/s. The lifted model was tested at ground level for the range of speeds stated above in order to determine the baseline. The lifted model was tested at 0.2 meters

and 0.4 meters for the same range of speeds. The guide plate dimensions were not changed throughout the experiment, with the exception of the angle of attack. The angle of attack was varied from $\pm 45^{o}$, 0^{o}, and 90^{o}. They concluded that lifting the model would be best suited to reduce the wind uplift. However, the authors noted that further studies would be needed to investigate the vibration of the supporting structures. The most significant reduction in wind uplift occurred with the guide plate model. The orientation of the guide plate in which this reduction occurred was 90^{o}.

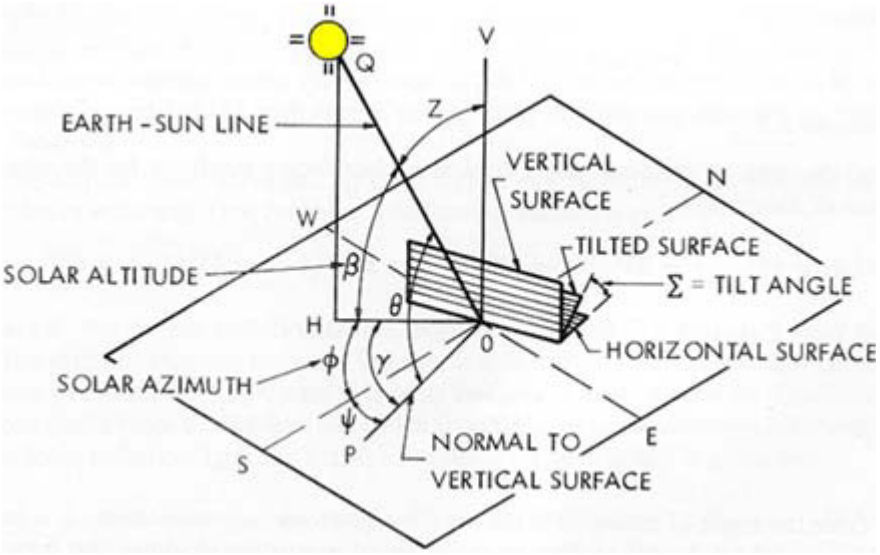

Figure 1.3 The solar azimuth angle for a photovoltaic array situated in the Northern hemisphere [AIA, 2010]

A recent study revealed the usefulness of wind tunnel experiments and CFD analysis for roof-mounted solar photovoltaic arrays [Meroney and Neff, 2010]. The purpose of the research was to find a correlation between the CFD simulations and wind tunnel experiments. The numerical analysis was used to determine lift and drag forces

and overturning moments on different solar photovoltaic arrays. Three different turbulence models, RNG, standard k-ε, and k-Ω were used for the study. The results from the numerical analysis were compared and validated with the data obtained from wind tunnel experiments.

All the wind tunnel models were tested at the same speed, roughly 10 m/s. The models investigated included single and multiple arrays, with and without deflectors. Also, different deflector models were tested. In all, ninety-two different types of models were tested in this study.

The RNG and k-Ω turbulence models were found to have the best agreement with the wind tunnel results. The k-Ω model proved to be the most accurate, when compared with the wind tunnel results, for the overturning moment. The k-ε turbulence model deviated the greatest from the wind tunnel results for the three measured loads.

1.2 Wind Management System for Solar Panel Racks

Solar panel companies often employ the use of a ballast to help anchor the solar panel racks on the top of the roof. The ballast distribution of the rack is an inefficient design because it adds additional weight to the top of the roof, increasing the cost of the installation and engineering analysis. Also, the additional ballast could cause the weight per foot (wt/ft) of the system to exceed the buildings' allowable limits. Therefore, a more efficient way of anchoring the solar panel racks to the roof was investigated. The result of the investigation was a wind management system, basically a wind deflector. The wind deflector was recommended to be placed behind and on the sides of the solar panel racks in order to reduce the side wind effects.

The wind deflector idea was thought of after realizing the need to reduce or completely eliminate the use of ballast. Although the wind deflector itself will add additional weight to the roof, it is a negligible amount compared to the ballast only approach to managing the wind forces on the solar panel racks. Multiple deflector designs were created, trialed, experimented and analyzed using the CFD software before a final design was picked and further research completed; including the help of wind tunnel experiments. These models are discussed further in **Chapter 2**. The final design of the deflector was investigated, analyzed, and validated with computational and wind tunnel experimentation.

1.3 Scope of Work

The primary goal of this thesis was to research wind deflector designs for rooftop solar panel racks manufactured by Northern States Metals (NSM) in Youngstown, Ohio. The solar panels will be installed in areas that experience high wind gusts that could cause damage to the solar panel racks and put multiple people in danger who walk or live below or around such buildings. There are two main methods associated with modern techniques that will be employed and their results will be discussed in this thesis; computational and wind tunnel experiments.

The computational analysis consisted of utilizing widely used, modern CFD software and coupled with a computer aided design (CAD) software to model, mesh, and numerically simulate a solution to complex fluid dynamics problems. The CFD program that was utilized to set-up and run the analysis was ANSYS. ANSYS is a commercially available software package that contains multiple sub-programs that help the user to pre-

process, simulate, and post-process a model. The CFD program that is embedded within ANSYS that runs the simulation is ANSYS Fluent. ANSYS DesignModeler and SolidWorks were used to pre-process the model for the creation of the geometries of the solar panel racks and deflectors. ANSYS DesignModeler was used for the development of the 2-D models whereas SolidWorks was used to create the 3-D models. The computer simulated models are discussed in more detail in Chapter 2.

The experimental analysis consisted of conducting multiple wind tunnel tests of quarter scale rooftop solar panel racks and wind deflectors. The wind tunnel, along with the models as suggested and demanded by this work, was provided by Northern States Metals. The lift and drag forces were measured using load cells that were connected to a data acquisition system and modules that were purchased from National Instruments (NI). The load cells had different orientations in order to measure the two forces; namely lift (vertical) and drag (horizontal) forces. The results that were obtained from the wind tunnel analysis were then used to verify the CFD simulations.

1.4 Thesis Structure

The materials presented in this thesis are organized in a manner that starts with the physical model of the solar panel racks and the deflector used in the wind tunnel experiments and CFD simulations discussed in **Chapter 2**. In **Chapter 3**, is a discussion of the mathematical models employed during the numerical simulation section of the thesis. The Chapter on the mathematical models includes the basic governing equations used to model fluid flow and turbulence characteristics of wind at high speeds. These equations include continuity, Navier-Stokes, and the k-ε turbulence model. In **Chapter 4,**

the methodology and techniques are described for the numerical simulation performed in ANSYS Fluent commercially available CFD software. Wind tunnel testing is described in **Chapter 5.** Results from computational simulation and experimental testing are reported in **Chapter 6**, followed by concluding remarks and recommendations for future work in **Chapter 7**. References cited and appendices for additional wind tunnel test models and computer simulation results are listed afterwards.

CHAPTER 2

PHYSICAL MODELING

Varieties of wind deflector profiles for the solar panel racks were fabricated by NSM and donated to YSU for wind tunnel testing. In terms of geometrical scales of these models, two sizes were studied; namely full scale and quarter scale models. There were two main models presented, full scale and quarter scale models. The full scale solar panel racks and corresponding wind deflectors were provided as computer models and were only used for CFD simulation purposes. The full scale models were excluded from the wind tunnel testing due to their size as compared with the wind tunnel testing space. However, the quarter scale solar panel racks and deflectors were tested by wind tunnel experiments and were run with computer simulations, which were later used for CFD code validation of full scale models. Quarter scale computer models were generated by utilizing the geometrical measurements of full scale models for the CFD simulation portion of the research. The quarter scale models were experimentally tested in a wind tunnel, as well as CFD simulations. All solar panel racks that were investigated in this study were at an inclination of 10^{o} with respect to the horizontal axis.

2.1 Models for Wind Tunnel Testing

There were six different models that were tested in the wind tunnel: single rack only, single rack with deflector, deflector only on the single rack length board, three racks only, three racks with deflector, and deflector only on the three rack length board; one board length is 4 ft. long. These models are shown in **Figures 2.1-2.5** (not to scale).

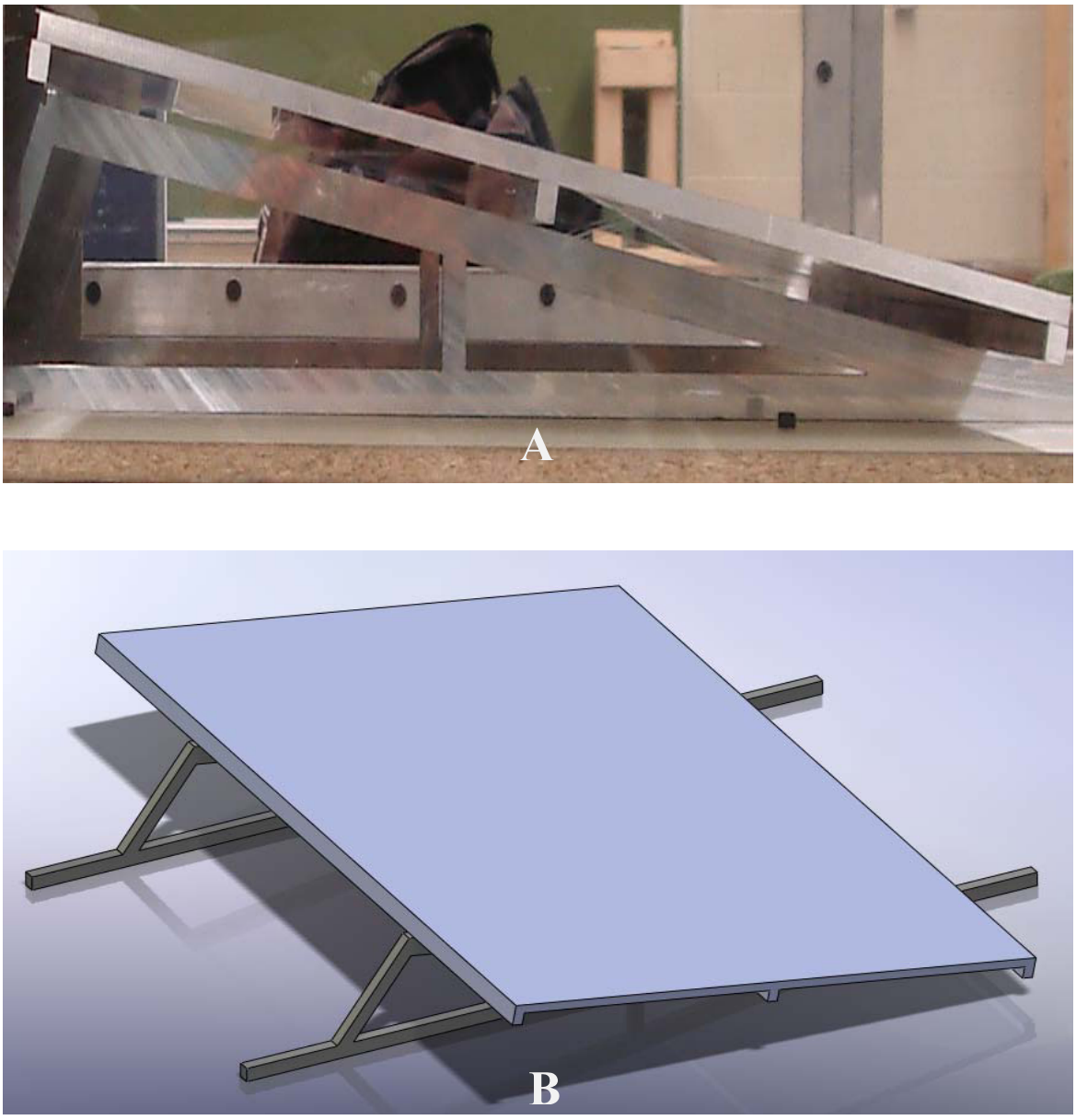

Figure 2.1 Quarter scale, single rack only (A) Photograph, and (B) SolidWorks Model

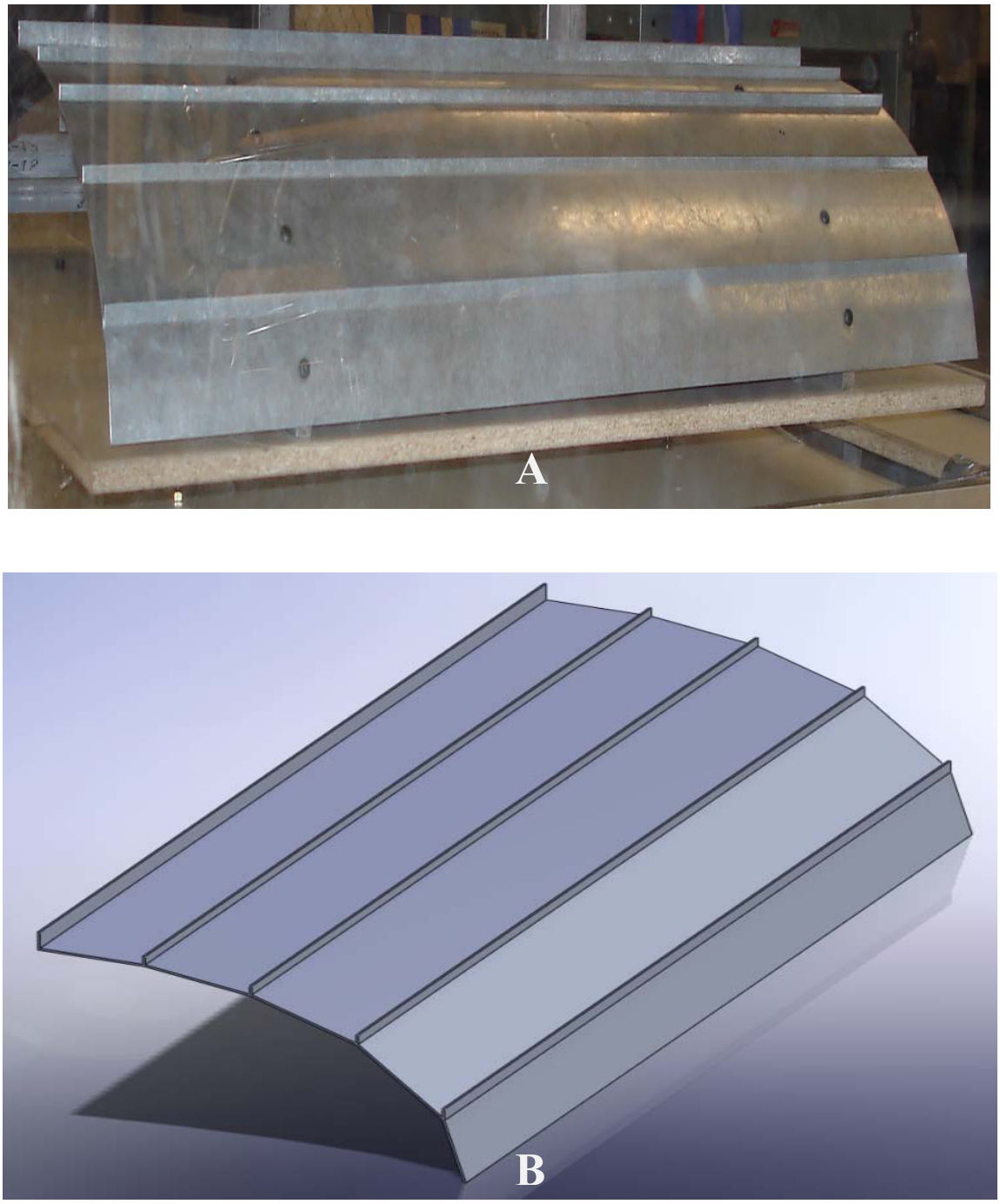

Figure 2.2 Quarter scale, deflector only (A) Photograph and (B) SolidWorks Model
(The same deflector was tested on the single- and 3 rack- length boards.)

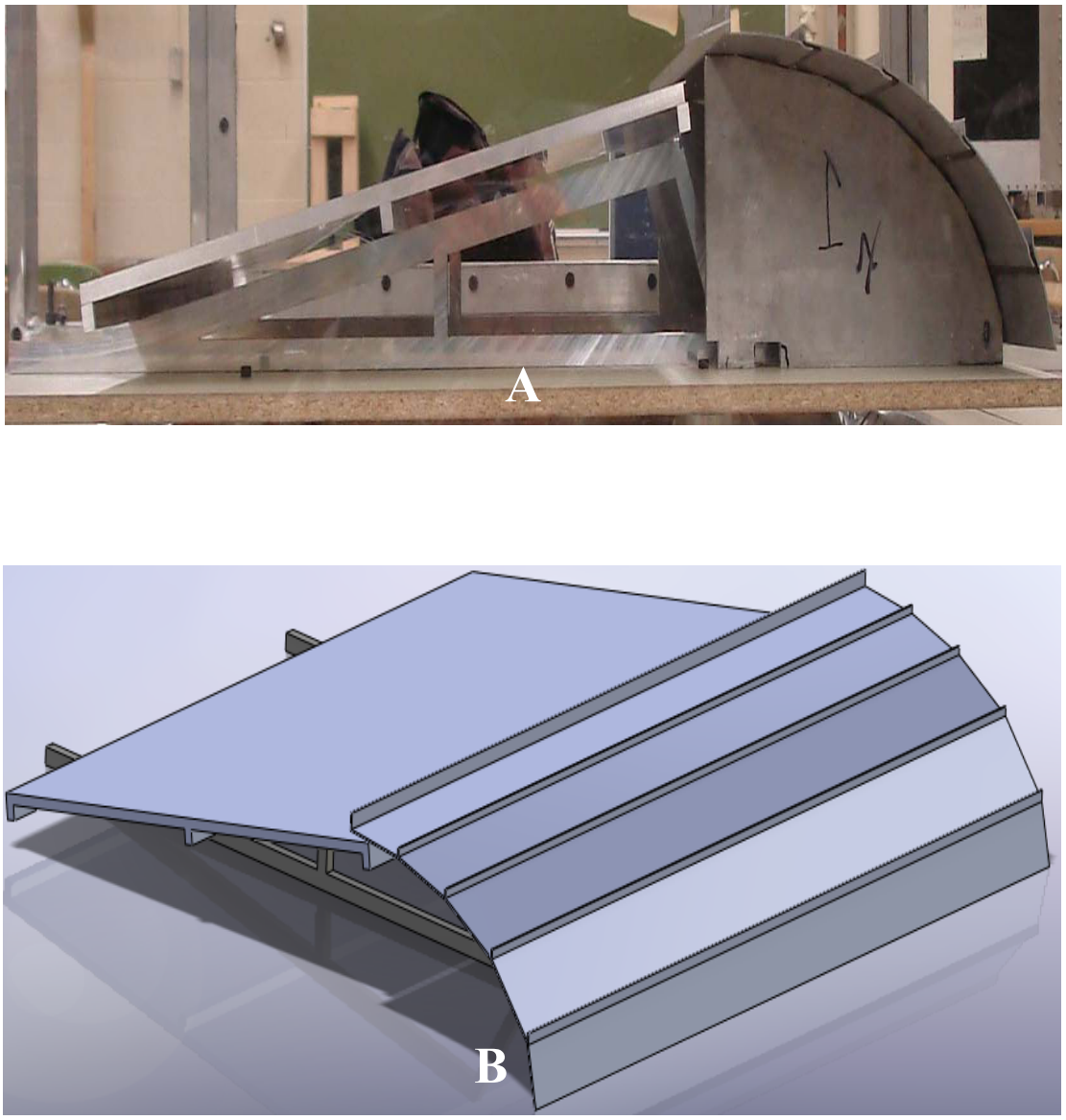

Figure 2.3 Quarter scale single rack with a deflector (A) Photograph, and (B) SolidWorks Model

Figure 2.4 Quarter scale, 3 racks only *(SolidWorks Model, Photograph is not shown)*

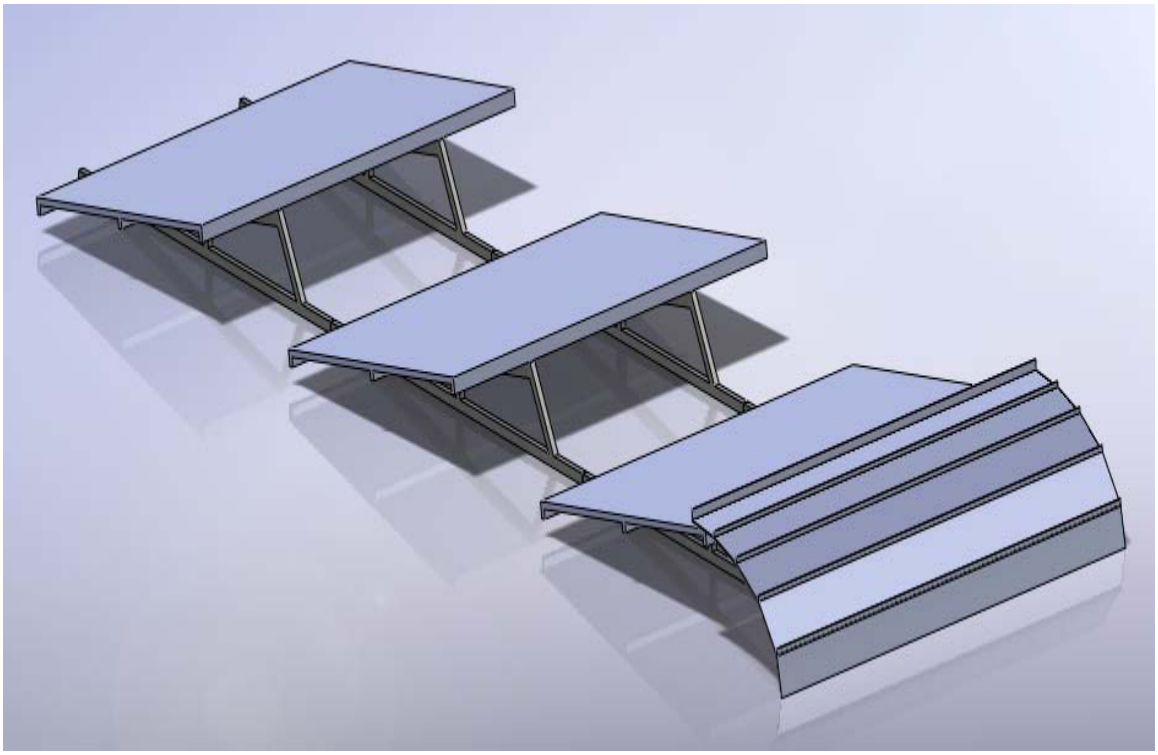

Figure 2.5 Quarter scale, 3 racks with a deflector *(SolidWorks Model, Photograph is not shown)*

As previously mentioned, ANSYS Fluent was employed for quarter scale model simulations in order to directly compare and validate the wind tunnel experiements. ANSYS Fluent 2-D studies were performed for full scale models, which were validated with ANSYS Fluent 3-D studies and wind tunnel test calibrations.

2.2 Models for Computational Simulation

There were two types of models that were tested using ANSYS Fluent, 2-D and 3-D. The 3-D models were initialy used to help determine the most efficient and suitable deflector design. Once an optimum design was chosen, the rack and deflector models were converted to 2-D in order to simplify the simulation process. Although the 3-D models are closer to real world situations, these types of models were recommended for future work. The recommendations were made due to the time constraints of the project. The 2-D studies took less time when compared with the 3-D models and had an allowable level of error.

3-D Models

Several models were created in SolidWorks and then imported into ANSYS in order to be meshed. The first deflector model was a simple, vertical wall that was oriented perpendicular to the wind flow. This model served as a building block for all the other models that were developed. The SolidWorks model of the vertical deflector is shown in **Figure 2.2**.

The other deflector models that were tested and studied, in order of least effective to most effective, are as follows: vertical (**Figure 2.6**), inclined (**Figure 2.7**), quarter circle (**Figure 2.8**), elliptic (**Figure 2.9**), elliptic with 2 inch lip (**Figure 2.10**), and

elliptic with 2 inch lip and fins (**Figure 2.11**). The single rack, with the respective deflector geometries is found in each individual figure (**Figures 2.7 – 2.11**). For more detailed drawings of **Figures 2.1 – 2.11**, refer to **Figures A.1 – A.12** in the **Appendix.**

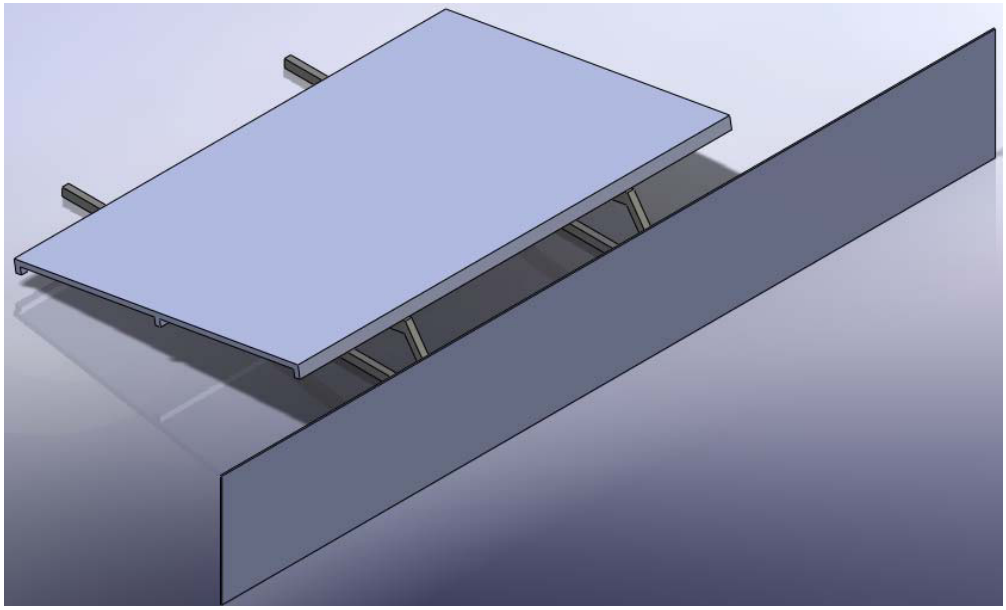

Figure 2.6 Vertical wall deflector at an angle $\theta = 90^{o}$ from horizontal axis

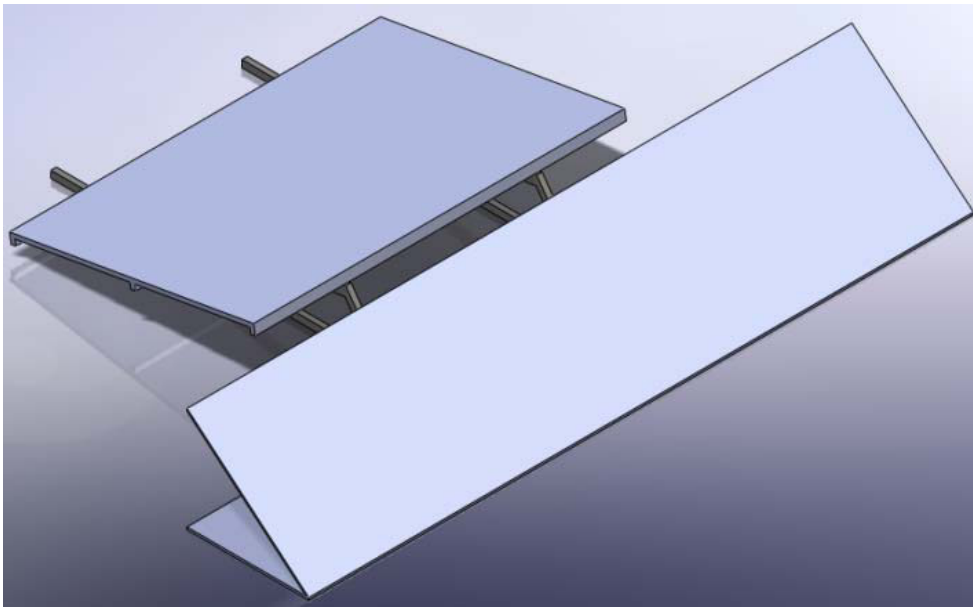

Figure 2.7 Inclined deflector at an angle $\theta = 40^{o}$ from horizontal axis

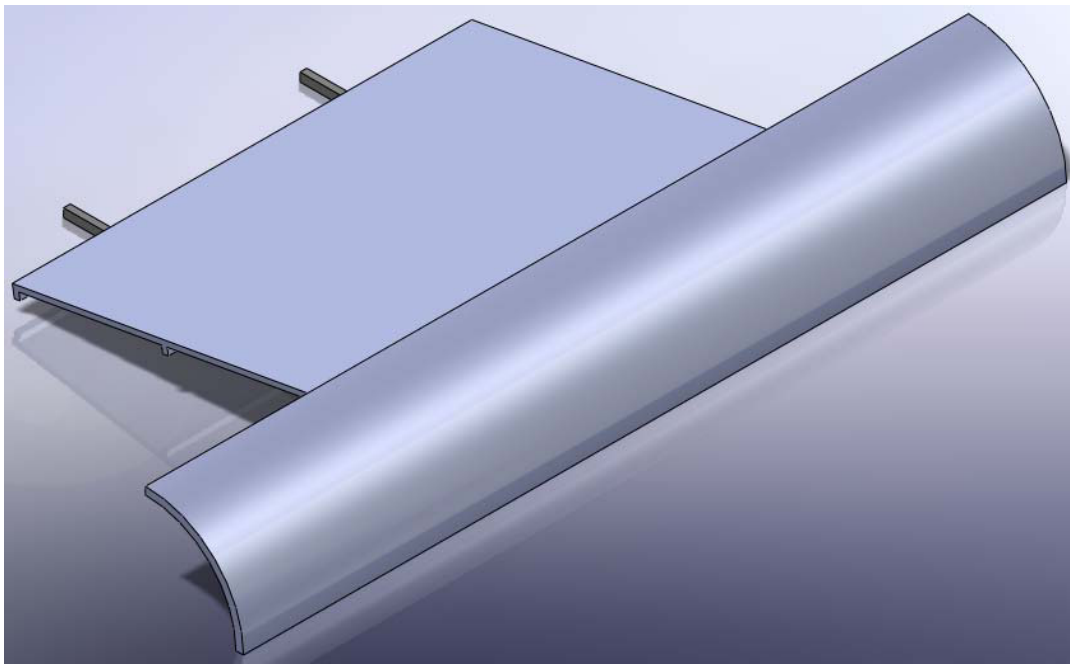

Figure 2.8 Quarter circle deflector

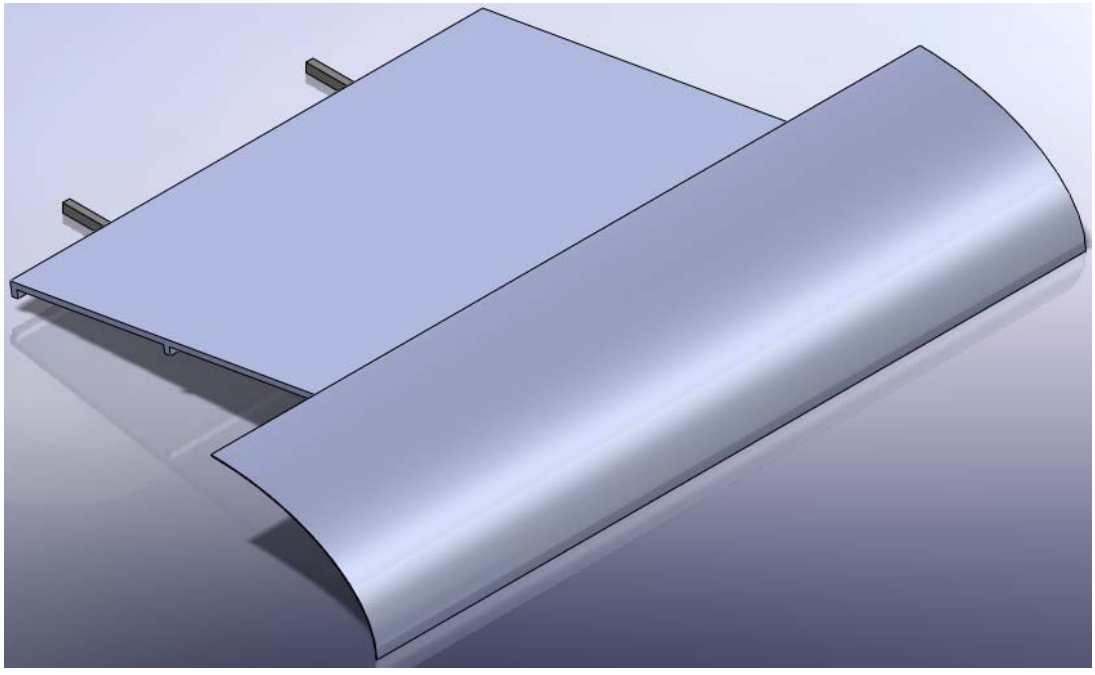

Figure 2.9 Elliptic deflector

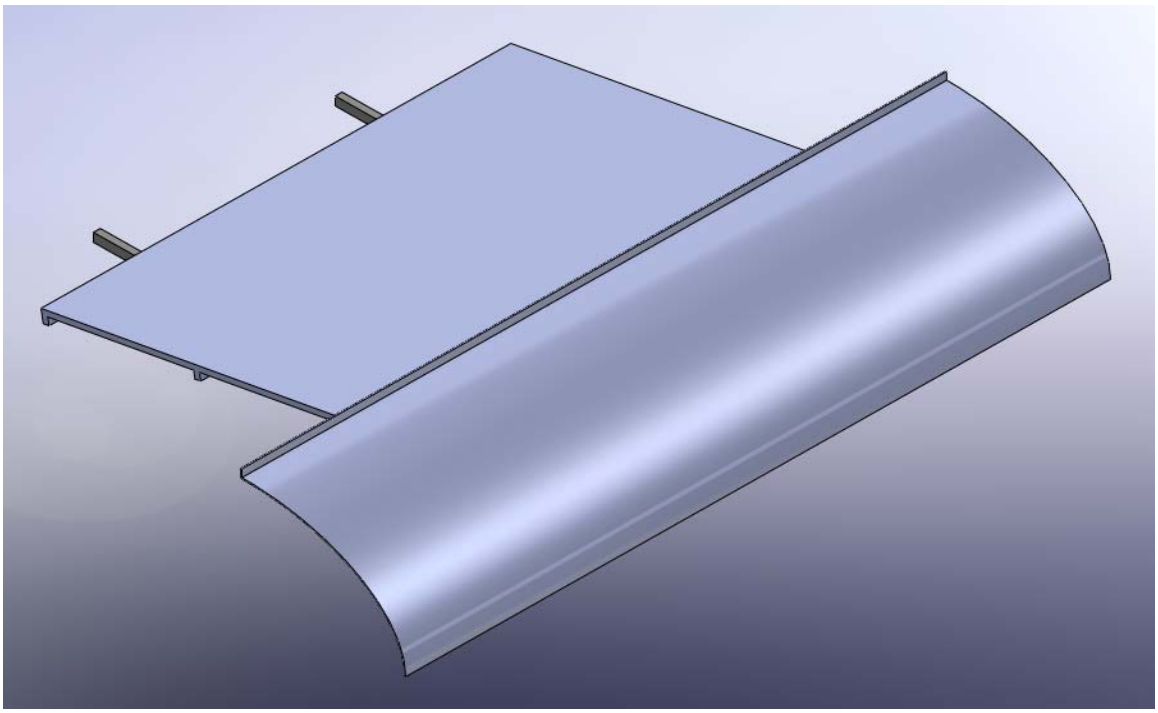

Figure 2.10 Elliptic deflector with 2 inch lip

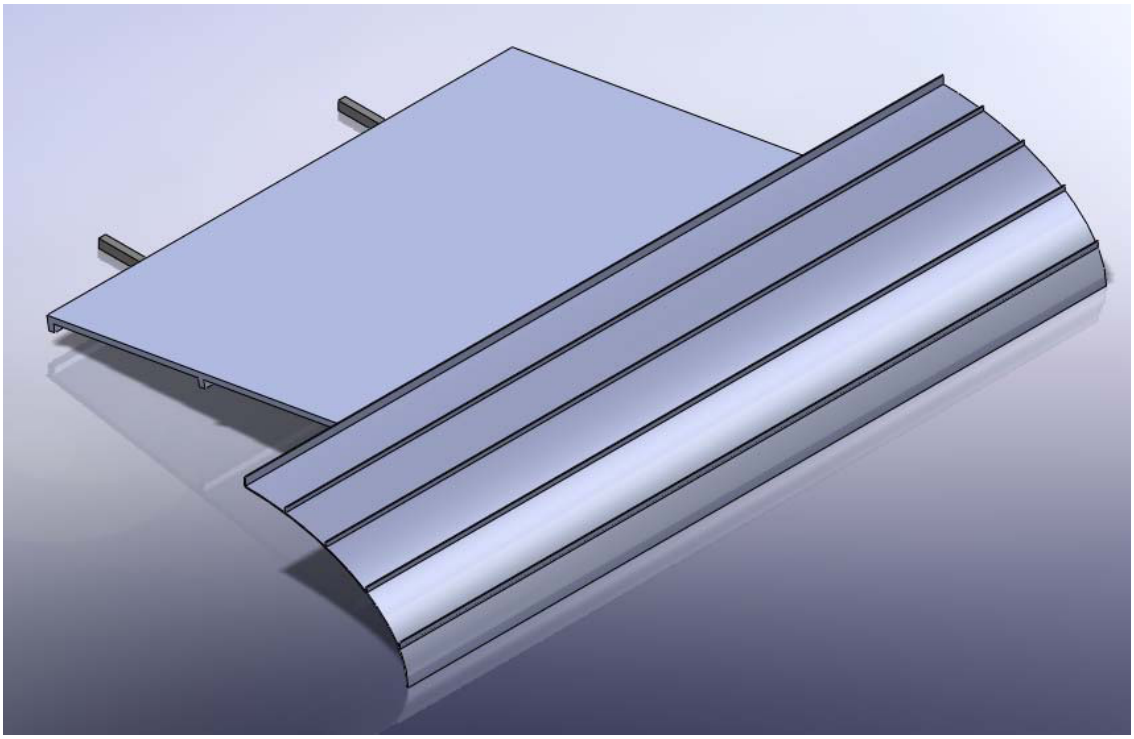

Figure 2.11 Elliptic deflector with 2 inch lip and fins

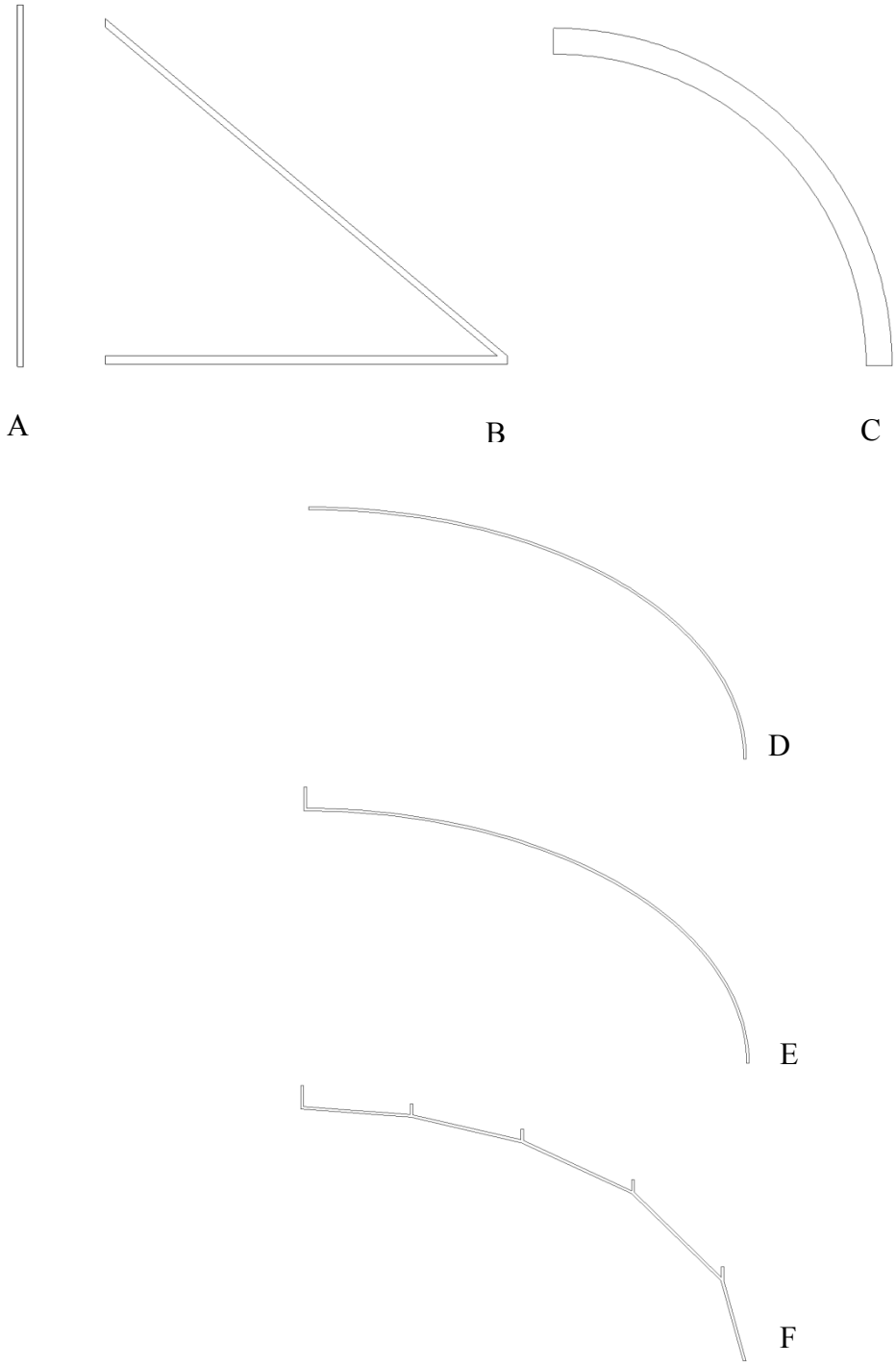

Figure 2.12 Side profiles of the deflectors (A) wall, (B) inclined, (C)quarter circle, (D)elliptic, (E) elliptic with 2 inch lip, and (F) elliptic with 2 inch lip plus fins

The side profiles of the deflector designs are enlarged and shown above in order to provide an improved representation of the deflector design. Please note that side profiles of the deflectors shown in Figure **2.12** are not to scale with respect to one another and are only for illustrative purposes. A typical array of 5 racks, with the appropriate flow field enclosure, is shown in **Figure 2.13**. It should be noted that the length of the flow field did not change for the simulation of one rack with and without the deflector.

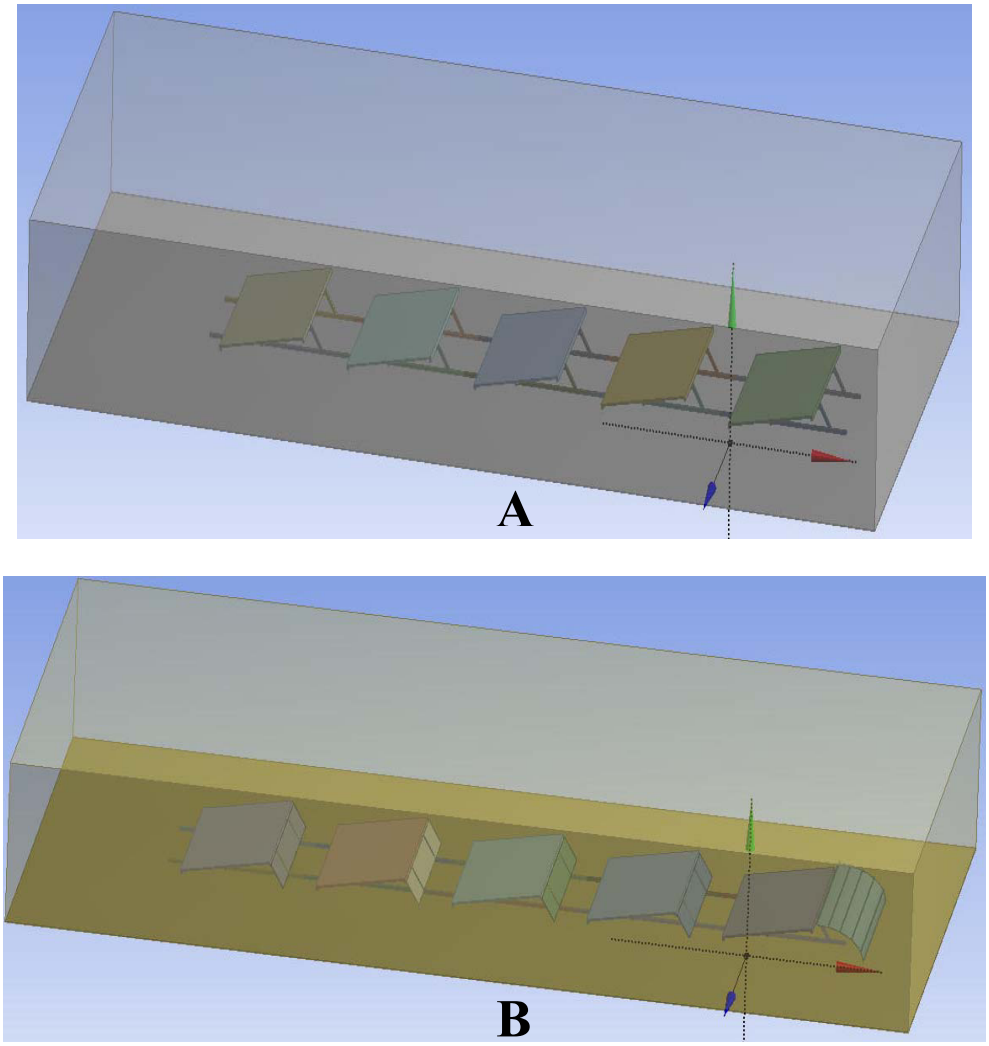

Figure 2.13 Three dimensional five racks array inside the fluid domain in front of solar panel racks (A) without finned-elliptic deflector, and (B) with finned-elliptic deflector

The models were meshed using the auto-mesh feature found in ANSYS Meshing with over 500,000 quadrilateral and triangular mesh elements. This mesh scheme utilizes both types of meshing elements and enables the model to be meshed quickly without sacrificing quality. For meshing purposes, the meshed elements were maintained as a fixed size function for the rack and deflector. This mesh feature enabled the mesh elements near a chosen place to start with a tiny element and then gradually grow as the elements reached the fluid domain. The size function feature helped to maintain good, quality mesh elements.

2-D Models

There were two main types of 2-D models that were simulated, full-scale and quarter-scale. The full scale models consisted of a single rack with and without a deflector, and five racks with and without a deflector. The length, height, and leading edge of the flow field for these full scale models were, respectively, twenty, ten, and four times the length of a single rack. The same type of meshing scheme used for the 3-D models was used for the full scale and quarter scale 2-D models. An example of the meshed flow field can be found in **Figure A.13**. The quadrilateral and triangular mesh elements are clearly visible in **Figure A.13**. The fixed size function feature was attached to the surfaces of the solar panel racks and deflector as shown. The mesh elements started at 0.00001 meters and then gradually grew outward to fill the entire flow field; every subsequent mesh element was 2% bigger than its previous element.

The quarter scale solar panel racks and deflectors were modeled and simulated in the computer using CFD codes to mimic the conditions of the wind tunnel testing. The racks and deflector were placed on a lifted platform along with a floor 2 inches below and

separate from the wind tunnel floor. The load cells that existed in the wind tunnel were not included in the 2-D computer simulation models because doing so would result in there being a "wall" between the platform and gap. This "wall" would cause the results to be erroneous due to incorrect modeling of the physical wind tunnel conditions; the same can be said for the support legs of the solar panel.

CHAPTER 3

MATHEMATICAL MODELING

The mathematical models consist of a set of governing equations that are used for a closed-form solution and are also embedded within ANSYS Fluent to analyze and describe the physical phenomena in a given fluid domain. There exist multiple governing equations that each has their own given characteristics to solve for certain values that are based upon the user's interest. The purpose of this chapter is to introduce and describe the governing equations of the fluid domain with the k-ε model used in this thesis for the aerodynamic analysis of the rooftop solar panel racks. A mathematical model is utilized in order to model the wind forces of flowing air on rooftop solar panel racks with and without deflectors.

In this thesis, rooftop solar panel racks with and without wind deflectors were modeled. Three fundamental equations are used to model the fluid flow over a model placed on a roof. The three equations used are the continuity, momentum, and generalized Navier-Stokes equations. A turbulent model was used in order to account for turbulent flow that exists with high wind speeds. The standard k-ε turbulence model is assumed as the most common and widely accepted model for the turbulence nature of flow simulations in CFD.

The following appropriate assumptions were made when using the governing equations for fluid flow over, around, and through the rooftop solar panel racks with and without wind deflectors:

- Turbulent flow – as the winds speed are high
- Incompressible flow – for negligible change in density of air flow
- Steady flow – as time dependent analysis is not considered.
- Newtonian fluid - wind having Newtonian fluid behavior for shear stress

3.1 Continuity Equations

The law of conservation of mass for fluid flow states that the rate of mass leaving a control volume is equal to the rate of mass entering the control volume. In other words, mass is always conserved in a control volume. The statement, expressed mathematically is shown in **Equation 3.1** which is further reduced into **Equation 3.2**.

$$\frac{\partial \rho}{\partial t} + \nabla \cdot \left(\rho \vec{V}\right) = 0 \tag{3.1}$$

Where,

$\frac{\partial \rho}{\partial t} \equiv$ rate of change of density within the control volume

$\nabla \equiv$ vector operator in Cartesian coordinates $= \frac{\partial}{\partial x}\hat{i} + \frac{\partial}{\partial y}\hat{j} + \frac{\partial}{\partial z}\hat{k}$

$\nabla \cdot \left(\rho \vec{V}\right) \equiv$ net flow across boundaries of the control volume

For incompressible flow, the continuity equation reduces to:

$$\nabla \cdot \left(\rho \vec{V}\right) = 0 \tag{3.2}$$

3.2 Momentum Equations

The conservation of momentum equation is obtained by applying principles of Newton's second law of motion to the fluid domain. Newton's second law states that the net force on a particle, or an object, is equal to the time rate of change of its linear momentum. This law can be applied to a fluid particle moving through 3-dimensional space. The result is three equations, each with respect to the x-,y-, and z- directions as shown in **Equations 3.3-3.5**.. Basically, the net force on the particle, or object, in the x-direction is equal to the time rate of change of its linear momentum in the x- direction. The same holds true for the y- and z- directions. The law, in mathematical terms, with respect to the three coordinate axes (x, y, z) is as follows:

$$\frac{\partial(\rho u)}{\partial t} + \nabla \cdot \rho \vec{V} u = dF_{Bx} + \frac{\partial \sigma_{xx}}{\partial x} + \frac{\partial \tau_{yx}}{\partial y} + \frac{\partial \tau_{zx}}{\partial z} + S_{Mx} \tag{3.3}$$

$$\frac{\partial(\rho v)}{\partial t} + \nabla \cdot \rho \vec{V} v = dF_{By} + \frac{\partial \tau_{xy}}{\partial x} + \frac{\partial \sigma_{yy}}{\partial y} + \frac{\partial \tau_{zy}}{\partial z} + S_{My} \tag{3.4}$$

$$\frac{\partial(\rho w)}{\partial t} + \nabla \cdot \rho \vec{V} w = dF_{Bz} + \frac{\partial \tau_{xz}}{\partial x} + \frac{\partial \tau_{yz}}{\partial y} + \frac{\partial \sigma_{zz}}{\partial z} + S_{Mz} \tag{3.5}$$

Where,

$\vec{V} \equiv$ total velocity vector of the fluid

$u, v, w \equiv$ x-, y-, and z-components of the velocity, respectively

$\sigma_{ii} \equiv$ normal viscous stress terms

$\tau_{ij} \equiv$ shear viscous stress terms

$dF_{Bi} \equiv$ differential body force component

$S_{Mi} \equiv$ momentum source term component

3.3 Navier-Stokes Equations

The viscous stresses and the rate of angular deformation, or in other words the rate of shearing strain, are directly proportional to one another for a Newtonian fluid. Since air is considered to be a Newtonian fluid, it is possible to express the viscous stresses in terms of velocity gradients. These expressions are **Equations 3.6-3.11** below:

$$\tau_{xy} = \tau_{yx} = \mu\left(\frac{\partial v}{\partial x} + \frac{\partial u}{\partial y}\right) \tag{3.6}$$

$$\tau_{yz} = \tau_{zy} = \mu\left(\frac{\partial w}{\partial y} + \frac{\partial v}{\partial z}\right) \tag{3.7}$$

$$\tau_{zx} = \tau_{xz} = \mu\left(\frac{\partial u}{\partial z} + \frac{\partial w}{\partial x}\right) \tag{3.8}$$

$$\sigma_{xx} = -p - \frac{2}{3}\mu\nabla\cdot\vec{V} + 2\mu\frac{\partial u}{\partial x} \tag{3.9}$$

$$\sigma_{yy} = -p - \frac{2}{3}\mu\nabla\cdot\vec{V} + 2\mu\frac{\partial v}{\partial y} \tag{3.10}$$

$$\sigma_{zz} = -p - \frac{2}{3}\mu\nabla\cdot\vec{V} + 2\mu\frac{\partial w}{\partial z} \tag{3.11}$$

Where,

$p \equiv$ local thermodynamic pressure

$\mu \equiv$ dynamic or absolute viscosity of the fluid

It should also be noted that the kinematic viscosity, υ, can be substituted for μ, the ratio of the dynamic viscosity of the fluid by its density, ρ.

The kinematic viscosity equation is shown in **Equation 3.12**.

$$\upsilon = \frac{\mu}{\rho} \tag{3.12}$$

Equations of viscous stress, **Equations 3.6–3.11,** are then combined with the differential equations of motion, **Equations 3.3–3.5**, resulting in the Navier-Stokes equations for each x-, y-, and z- component. The equations are as follows:

$$\rho\frac{Du}{Dt}=\rho g_x-\frac{\partial p}{\partial x}+\frac{\partial}{\partial x}\left[\mu\left(2\frac{\partial u}{\partial x}-\frac{2}{3}\nabla\cdot\vec{V}\right)\right]+\frac{\partial}{\partial y}\left[\mu\left(\frac{\partial u}{\partial y}+\frac{\partial v}{\partial x}\right)\right]+\frac{\partial}{\partial z}\left[\mu\left(\frac{\partial w}{\partial x}+\frac{\partial u}{\partial z}\right)\right] \quad (3.13)$$

$$\rho\frac{Dv}{Dt}=\rho g_y-\frac{\partial p}{\partial y}+\frac{\partial}{\partial x}\left[\mu\left(\frac{\partial u}{\partial y}+\frac{\partial v}{\partial x}\right)\right]+\frac{\partial}{\partial y}\left[\mu\left(2\frac{\partial v}{\partial y}-\frac{2}{3}\nabla\cdot\vec{V}\right)\right]+\frac{\partial}{\partial z}\left[\mu\left(\frac{\partial v}{\partial z}+\frac{\partial w}{\partial y}\right)\right] \quad (3.14)$$

$$\rho\frac{Dw}{Dt}=\rho g_z-\frac{\partial p}{\partial z}+\frac{\partial}{\partial x}\left[\mu\left(\frac{\partial w}{\partial x}+\frac{\partial u}{\partial z}\right)\right]+\frac{\partial}{\partial y}\left[\mu\left(\frac{\partial v}{\partial z}+\frac{\partial w}{\partial y}\right)\right]+\frac{\partial}{\partial z}\left[\mu\left(2\frac{\partial w}{\partial z}-\frac{2}{3}\nabla\cdot\vec{V}\right)\right] \quad (3.15)$$

Above, **Equations 3.13 – 3.15** can be further reduced when a flow is assumed to be incompressible and has a constant viscosity. These assumptions were the same for flow over the wind deflectors only, rooftop solar panel racks only, and the combination of racks with wind deflectors. The reduced form, and more recognizable form of the Navier-Stokes equations, can be found in **Equations 3.16 – 3.18**.

$$\rho\left(\frac{\partial u}{\partial t}+u\frac{\partial u}{\partial x}+v\frac{\partial u}{\partial y}+w\frac{\partial u}{\partial z}\right)=-\frac{\partial p}{\partial x}+\mu\left(\frac{\partial^2 u}{\partial x^2}+\frac{\partial^2 u}{\partial y^2}+\frac{\partial^2 u}{\partial z^2}\right)+\rho g_x \quad (3.16)$$

$$\rho\left(\frac{\partial v}{\partial t}+u\frac{\partial v}{\partial x}+v\frac{\partial v}{\partial y}+w\frac{\partial v}{\partial z}\right)=-\frac{\partial p}{\partial y}+\mu\left(\frac{\partial^2 v}{\partial x^2}+\frac{\partial^2 v}{\partial y^2}+\frac{\partial^2 v}{\partial z^2}\right)+\rho g_y \quad (3.17)$$

$$\rho\left(\frac{\partial w}{\partial t}+u\frac{\partial w}{\partial x}+v\frac{\partial w}{\partial y}+w\frac{\partial w}{\partial z}\right)=-\frac{\partial p}{\partial z}+\mu\left(\frac{\partial^2 w}{\partial x^2}+\frac{\partial^2 w}{\partial y^2}+\frac{\partial^2 w}{\partial z^2}\right)+\rho g_z \quad (3.18)$$

Taking into account the assumptions stated earlier in this Chapter, the equations can be reduced further. Also, only two-dimensional flow was considered. The simplified Navier-Stokes equations are expressed as **Equations 3.19** and **3.20**.

$$\rho\left(u\frac{\partial u}{\partial x}+v\frac{\partial u}{\partial y}+w\frac{\partial u}{\partial z}\right)=-\frac{\partial p}{\partial x}+\mu\left(\frac{\partial^2 u}{\partial x^2}+\frac{\partial^2 u}{\partial y^2}+\frac{\partial^2 u}{\partial z^2}\right) \tag{3.19}$$

$$\rho\left(u\frac{\partial v}{\partial x}+v\frac{\partial v}{\partial y}+w\frac{\partial v}{\partial z}\right)=-\frac{\partial p}{\partial y}+\mu\left(\frac{\partial^2 v}{\partial x^2}+\frac{\partial^2 v}{\partial y^2}+\frac{\partial^2 v}{\partial z^2}\right) \tag{3.20}$$

3.4 Transport Equations

The two equation models of turbulent transport in a fluid domain with turbulent energy and its dissipation rate are the most simple and robust. The transport equations allow for the turbulent velocity and length scales to be determine independently from another. The k-ε model is the most simple and robust of the two equation models. It is known to be the most widely used and accepted turbulent model to investigate fluid flows and heat transfer problems.

The model consists of the turbulent kinetic energy, k, and the rate of dissipation ε. The turbulent kinetic energy and dissipation rate are displayed, respectively, as shown by two **Equations 3.21** and **3.22**.

$$\frac{\partial}{\partial t}(\rho k)+\frac{\partial}{\partial x_i}(\rho k u_i)=\frac{\partial}{\partial x_j}\left[\left(\mu+\frac{\mu_t}{\sigma_k}\right)\frac{\partial k}{\partial x_j}\right]+G_k+G_b-\rho\varepsilon-Y_M+S_k \tag{3.21}$$

$$\frac{\partial}{\partial t}(\rho\varepsilon)+\frac{\partial}{\partial x_i}(\rho\varepsilon u_i)=\frac{\partial}{\partial x_j}\left[\left(\mu+\frac{\mu_t}{\sigma_\varepsilon}\right)\frac{\partial \varepsilon}{\partial x_j}\right]+C_{1\varepsilon}\frac{\varepsilon}{k}(G_k+C_{3\varepsilon}G_b)-C_{2\varepsilon}\rho\frac{\varepsilon^2}{k}+S_\varepsilon \tag{3.22}$$

Where,

$G_k \equiv$ generation of turbulent kinetic energy due to the mean velocity gradient

$G_b \equiv$ generation of turbulent kinetic energy due to buoyancy

$Y_M \equiv$ contribution of the fluctuating dilatation in compressible turbulence to the overall dissipation rate

$S_k \equiv$ user defined source term

$S_\varepsilon \equiv$ user defined source term

The turbulent viscosity μ_t, is found from **Equation 3.23**.

$$\mu_t = \rho C_\mu \frac{k^2}{\varepsilon} \tag{3.23}$$

The arbitrary constants in the above two equations have the following default values in Fluent: $C_{1\varepsilon} = 1.44$, $C_{2\varepsilon} = 1.92$, $C_\mu = 0.09$, $\sigma_k = 1.00$, $\sigma_\varepsilon = 1.30$. As explained in the ANSYS Fluent Manual, the default values listed above have been determined experimentally, using water and air as the main focus of the analysis. These values are acceptable for wall-bounded and free shear flows and are appropriate for a CFD study of solar panel racks positioned in a wall-bounded fluid domain.

CHAPTER 4

NUMERICAL MODELING

Numerical analysis involves solving a problem through the use of an algorithm and mathematical model. Numerical simulation and modeling is a technique that allows for highly complex, mathematical equations to be solved. Software that combines numerical techniques with the intricacies of fluid flow is utilized. ANSYS Fluent allows the user to solve a highly complex fluid flow problem. The software was built to model and analyze many types of laminar and turbulent fluid flows. The software has different packages and add-ons that allow the user to model various geometries with different mathematical models. The software comes with its own geometry modeling software, ANSYS Design Modeler. A third party computer aided design (CAD) program, such as SolidWorks, can be used to create the model geometry instead of ANSYS Design Modeler. The remaining add-ons include ANSYS Meshing and ANSYS Fluent. The meshing software, depending on the quality of the mesh, enables the user to achieve varying degrees of accuracy; the finer the mesh, the more accurate the solution. The processing and post-processing of the meshed model were performed in ANSYS Fluent. The algorithms and programs that were used in the study of the rooftop solar panel racks are discussed in the sections that follow.

ANSYS Fluent is equipped with several add-ons that enable the user to model and analyze complex fluid flows. The software also has the ability to couple the effects of heat transfer with fluid flow. However, the latter was beyond the scope of this thesis and will not be discussed.

ANSYS Fluent couples the equations of flow theory with mathematical models in order to solve highly complex fluid flows. ANSYS Fluent consists of two different flow solvers, each with their own strengths and weaknesses. The two flow solvers used in ANSYS Fluent are the pressure-based and density-based solvers. The pressure-based solver will be discussed in more detail in **Section 4.2**.

4.1 CFD Methodology

The procedure to set-up and run a successful simulation in ANSYS Fluent, for a fluid flow problem, consists of a series of steps that are completed sequentially. The procedure is outlined below.

1. Construction of the geometrical models using ANSYS Design Modeler or in another CAD program. For the scope of this thesis, the 2-D models were constructed using ANSYS Design Modeler and the 3-D models with SolidWorks.
2. Division of the fluid domain of the geometrical model into discrete volumes using appropriate meshing parameters and techniques via ANSYS Meshing. It is advantageous to have smaller volumes near the points of interest of the model and areas where the physical phenomena of the fluid will be more prevalent and important.

3. Determination and selection of the appropriate modeling technique available in ANSYS Fluent that best conforms to the conditions and phenomena of the flow situation of the problem.
4. Defining the boundary conditions and fluid properties.
5. Using the chosen solver in Fluent iterate the numerical model until a converged solution is achieved.

In order to set-up and run a successful model, there are a few sub-programs that are required. These programs include the pre-processor, solver, and post-processor. The pre-processor includes the building and meshing of the geometry in terms of boundaries and fluid domain. The programs that were used to model and mesh the geometry in this thesis included SolidWorks, ANSYS Design Modeler, and ANSYS Meshing. After the models were created, the mesh was applied using ANSYS Meshing. The main program, ANSYS Fluent was responsible for numerical simulation and post-processing of the results. The solver enables the user to numerically solve the mathematical equations as described in **Chapter 3**.

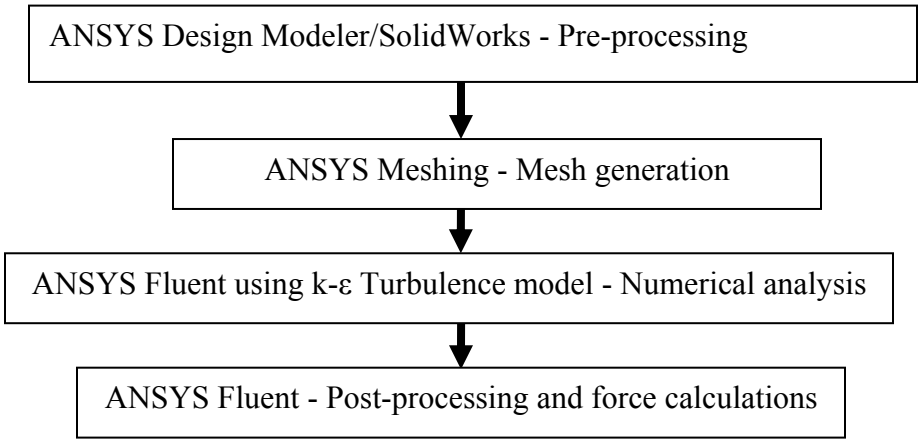

Figure 4.1 CFD methodology

The post-processor feature of ANSYS Fluent allows for the user to evaluate, visualize, and read the results obtained from the solver, qualitatively and quantitatively. **Figure 4.1** displays the methodology described above, in the form of a flow chart. Pre-processing and meshing, the first two steps as outlined in **Figure 4.1**, are described in detail below.

Pre-processing is the first step in the numerical analysis that originates with the design of the model. This can be done one of two ways; either by creating the geometry in ANSYS DesignModeler or by a CAD program such as SolidWorks or AutoCAD. For this project, once the model/geometry was constructed, it was necessary to develop the enclosure, or "flow field" of the model. For 2-D models a rectangular enclosed area served as the flow field and was placed around the geometries of importance. As for the 3-D models, a rectangular box was generated as the flow field and placed around the geometries. After the wall boundaries, geometries, and enclosed domains were defined, ANSYS Meshing followed.

ANSYS Meshing allows the user to choose and apply various meshing features and techniques in order to have a sufficient model for the solver and for accurate simulation results. The meshing program discretizes the geometries, i.e. the flow field box, into small cells or volumes depending on whether the model is 2-D or 3-D. The meshing applied to the flow field can be chosen from several options such as, uniform quadrilateral only, triangular only or quadrilateral plus triangular elements. An optimal meshing technique, in conjunction with a fixed size function, enables the user to attain very small elements on the surface and area surrounding the geometries that are within the skewness requirements in ANSYS Fluent. It should be noted that skewness is a ratio

of the size all the sides of the cell or volume, compared to one another. According to ANSYS Fluent, a mesh with a maximum skewness of less than 0.85 is considered good. Once the model is finely meshed, it is then possible for the model to be exported to ANSYS Fluent.

4.2 CFD Solver Techniques

The selection of the solver is very important for more accurate results when compared with experimental results and for fewer errors. The user must specify the type of solver, pressure or density based, and whether the flow is steady or unsteady. For the materials presented in this thesis, the solver chosen was pressure based and the flow was considered steady in order to obtain more realistic and accurate results from the simulations.

The pressure based solver uses a closed loop algorithm to solve the mathematical models, as described earlier in **Chapter 3**. The fluid flow was considered as a steady state flow in order to simplify the CFD simulations for the wind tunnel experiments. The pressure based solver will be discussed in the following.

Pressure-Based Segregated Algorithm

The pressure-based solver in ANSYS Fluent is used for most incompressible flows, whereas the density-based solver is used for compressible flows. Since the highest flow speeds the solar panel racks experience is well below the Mach number of 0.3 in which compressible effects need to be considered, the pressure-based solver is the best choice. The Mach number in which flows are considered to experience compressible

effects is 0.7. The highest wind speed under study was considered to be 110 mph, or hurricane type winds in California, which is Mach number 0.14.

The pressure-based solver uses an algorithm to solve for the governing equation, as discussed in **Chapter 3**, in a sequential order. The solution to the governing equations is an iterative process. **Figure 4.2** is an overview of the iterative process for the pressure-based solver.

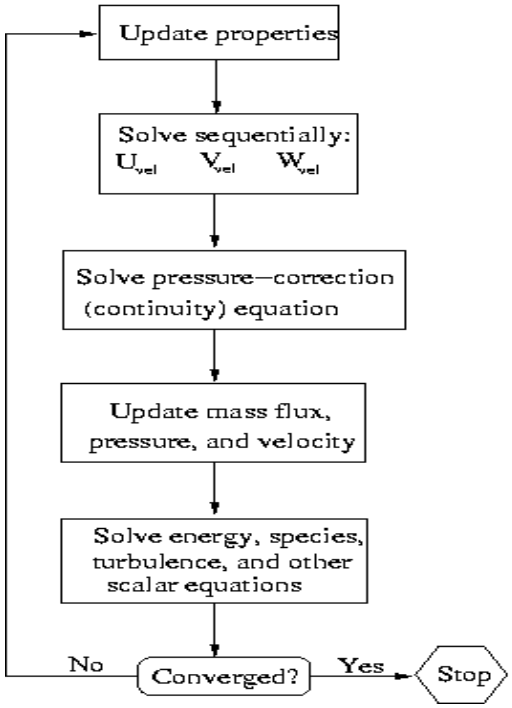

Figure 4.2 Pressure-based segreagated algorithm [Fluent Inc., (2009-2011)].

The "Update Properties" block at the top of **Figure 4.2** represents an initial guess. The initial guess is then used to solve for the momentum equation and then used to solve for the pressure correction as given by the governing equations. Once the solution to the pressure correction equation is consistently solved, the output is used to solve for the

velocity field, mass fluxes, and pressure sequentially. These solutions are then used to solve for any other remaining scalar quantities such as turbulence and energy.

Species transport was not included in the scope of this thesis as the fluid is considered pure - free of any chemical or other carrying species. Finally, the convergence criteria are checked, and if the solutions have met the criteria, the iterative process is stopped and the solution is converged. If not, the solution is put back into the iterative loop and the process repeated.

Discretization Technique

Fluent uses a discretization technique to turn a general scalar equation into an algebraic equation which enables the equations to be solved numerically. The governing equations are integrated about each of the volumes created during the meshing process. In doing so, the discrete equations satisfy the laws of mass conservation. **Equation 4.1**, shown below describes the discretization process for an arbitrary control volume, V.

$$\oint \rho\phi\vec{v} \cdot d\vec{A} = \oint \Gamma_\phi \nabla\phi \cdot d\vec{A} + \int_V S_\phi dV \tag{4.1}$$

Where,

$\rho \equiv$ density

$\vec{v} \equiv$ velocity vector

$\vec{A} \equiv$ surface area vector

$\Gamma_\phi \equiv$ diffusion coefficient for ϕ

$\nabla\phi \equiv$ gradient of ϕ

$S_\phi \equiv$ source of ϕ per unit volume

Equation 4.1 can be simplified for a fluid flow through a surface area. This simplified equation, is shown in **Equation 4.2.**

$$\sum_{f}^{Nfaces} \rho_f \vec{v}_f \phi_f \cdot \vec{A}_f = \sum_{f}^{Nfaces} \Gamma_\phi \nabla \phi_f \cdot \vec{A}_f + S_\phi V \tag{4.2}$$

Where,

$N_{faces} \equiv$ number of faces enclosing cell

$\phi_f \equiv$ value of ϕ convected through face of f

$\rho_f \vec{v}_f \cdot \vec{A}_f \equiv$ mass flux through the face, f

$\vec{A}_f \equiv$ area of face, f

$\nabla \phi_f \equiv$ gradient of ϕ at face f

$V \equiv$ cell volume

Fluent, by default, stores the individual values of ϕ at the center of each of the volumes. One problem that arises is that the faces values, ϕ_f, are required to determine that convective terms in **Equation 4.2**. In order to solve this problem, the face values are determined by interpolation. The interpolation method involves the use of the values from the center of the volume via an upwind scheme.

There are two upwind schemes that can be used for this interpolation process; a first order and second order. The first order upwind scheme assumes the cell-center values to be equal to the average value of the cell. In other words, $\phi_f = \phi$. The second order upwind scheme is used when a higher level of accuracy is preferred. The second order scheme, to determine the face values, uses a multidimensional linear reconstruction approach to achieve this higher level of accuracy. It involves the use of a Taylor Series

expansion of the volume centered solution about the centroid of each mesh element. The second order upwind scheme was utilized for the 2-D and 3-D analysis of the rooftop solar panel racks.

Convergence Criteria

The use of a numerical modeling technique requires ways to measure the validity and accuracy of the simulated solution. The way in which ANSYS Fluent determines whether or not a solution is valid, is by way of convergence criteria. The convergence criteria found in ANSYS Fluent depends on what type of model is chosen. Each model contains its own residuals that ANSYS Fluent monitors in order to determine a converged solution. These residuals, depending on the type of model selected, involve x- and y-components of velocities, k and ε that include continuity, turbulence, and energy.

As stated earlier in the chapter, ANSYS Fluent uses an iterative process to achieve the best solution. The error between the previous and current solution is determined after each iteration. A converged solution depends on the error between the two solutions. It should be noted that an absolute converged solution, one where the error between the current and previous solution is zero, is very hard to obtain. Also, it is not always practical to achieve an absolute converged solution. The default settings for the residuals in ANSYS Fluent were 10^{-3}. These default settings are good for some simpler problems, but for most complicated problems, smaller error settings are required for better accuracy and good convergence. As a result, the residuals for the simulations here were set to have convergence criteria of at least 10^{-6} units and in some cases 10^{-9} units for the respective fluid parameters.

CHAPTER 5

WIND TUNNEL TESTING

Wind tunnel instrumentation, experimental procedures of wind tunnel testing and data acquisition system embedded with LabVIEW are explained in this Chapter. The wind tunnel consists of an axial fan (Cincinnati Fan-Size 48, Mason, Ohio) that was powered by a 10 horsepower motor in a 4-ft diameter housing as shown in **Figure 5.1**. The circular fan was attached to the rectangular, 4 foot by 4 foot, transition section of the wind tunnel. The fan was run by a variable frequency drive (VFD) (Allen Bradley, Model PowerFlex-4M) that was connected to a data acquisition system [National Instruments, NI cDAQ-9172, module NI 9264]. The NI 9264 allowed the user to vary the input voltage to the fan from 0 to 10 V DC. Also, the frequency input for the VFD had an input range, from 0 to 80 Hz, that is capable of providing wind speeds, up to 27 miles per hour (mph), to the fan. The National Instruments hardware was run from a program created in LabVIEW v8.6 software. Also screenshot of the block diagram is shown in **Figure 5.2** that was created using LabVIEW software for fan control and load cell data acquisition. Other components used for the experimental wind tunnel set-up included four load cells [Futek, Model LCF300] and modules designed to communicate information between the computer and the data acquisition device [National Instruments, modules NI 9219 and NI 9237].

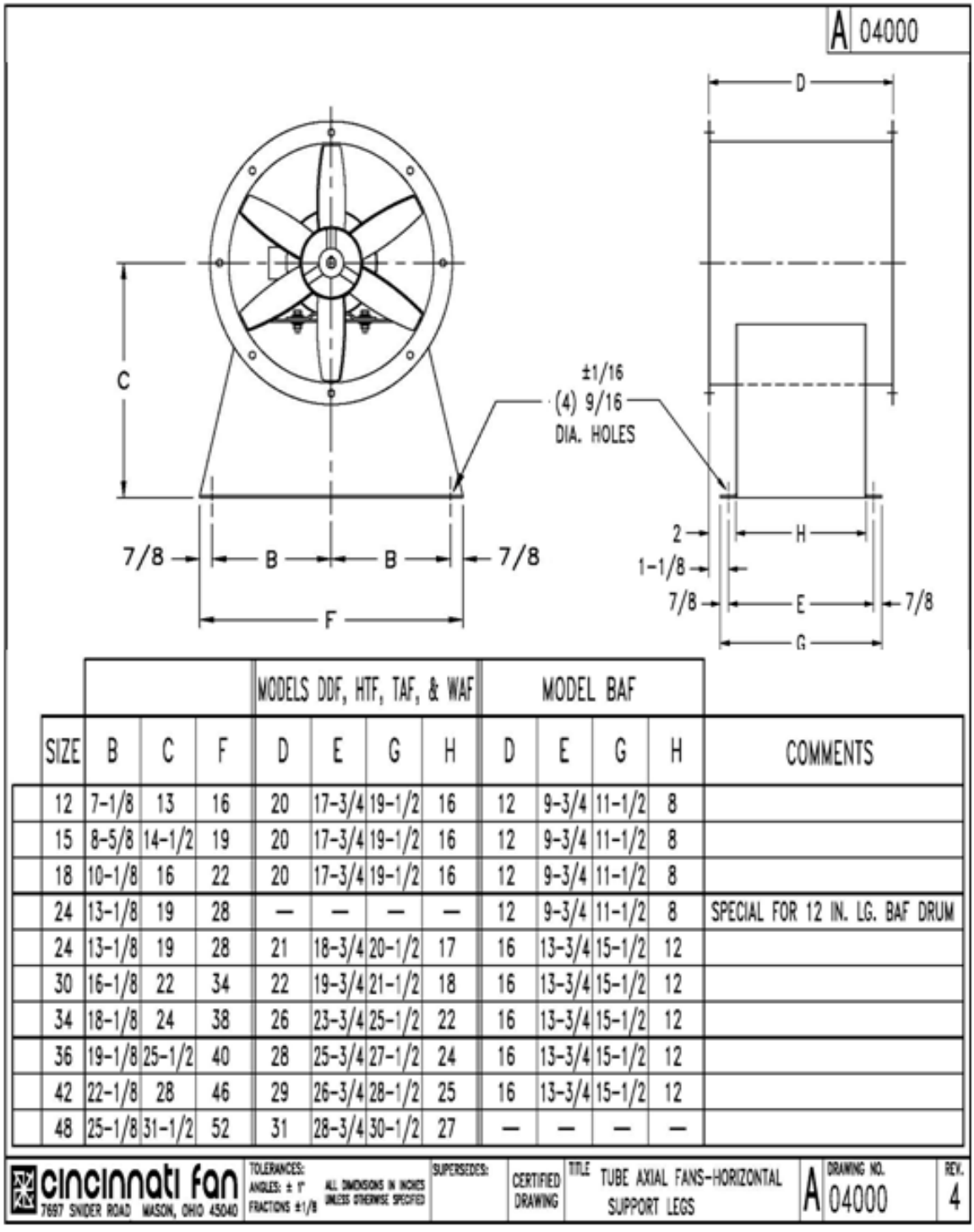

SIZE	B	C	F	MODELS DDF, HTF, TAF, & WAF D	E	G	H	MODEL BAF D	E	G	H	COMMENTS
12	7-1/8	13	16	20	17-3/4	19-1/2	16	12	9-3/4	11-1/2	8	
15	8-5/8	14-1/2	19	20	17-3/4	19-1/2	16	12	9-3/4	11-1/2	8	
18	10-1/8	16	22	20	17-3/4	19-1/2	16	12	9-3/4	11-1/2	8	
24	13-1/8	19	28	—	—	—	—	12	9-3/4	11-1/2	8	SPECIAL FOR 12 IN. LG. BAF DRUM
24	13-1/8	19	28	21	18-3/4	20-1/2	17	16	13-3/4	15-1/2	12	
30	16-1/8	22	34	22	19-3/4	21-1/2	18	16	13-3/4	15-1/2	12	
34	18-1/8	24	38	26	23-3/4	25-1/2	22	16	13-3/4	15-1/2	12	
36	19-1/8	25-1/2	40	28	25-3/4	27-1/2	24	16	13-3/4	15-1/2	12	
42	22-1/8	28	46	29	26-3/4	28-1/2	25	16	13-3/4	15-1/2	12	
48	25-1/8	31-1/2	52	31	28-3/4	30-1/2	27	—	—	—	—	

Figure 5.1 Axial fan used in wind tunnel testing (Cincinnati Fan-Size 48, Mason, Ohio)

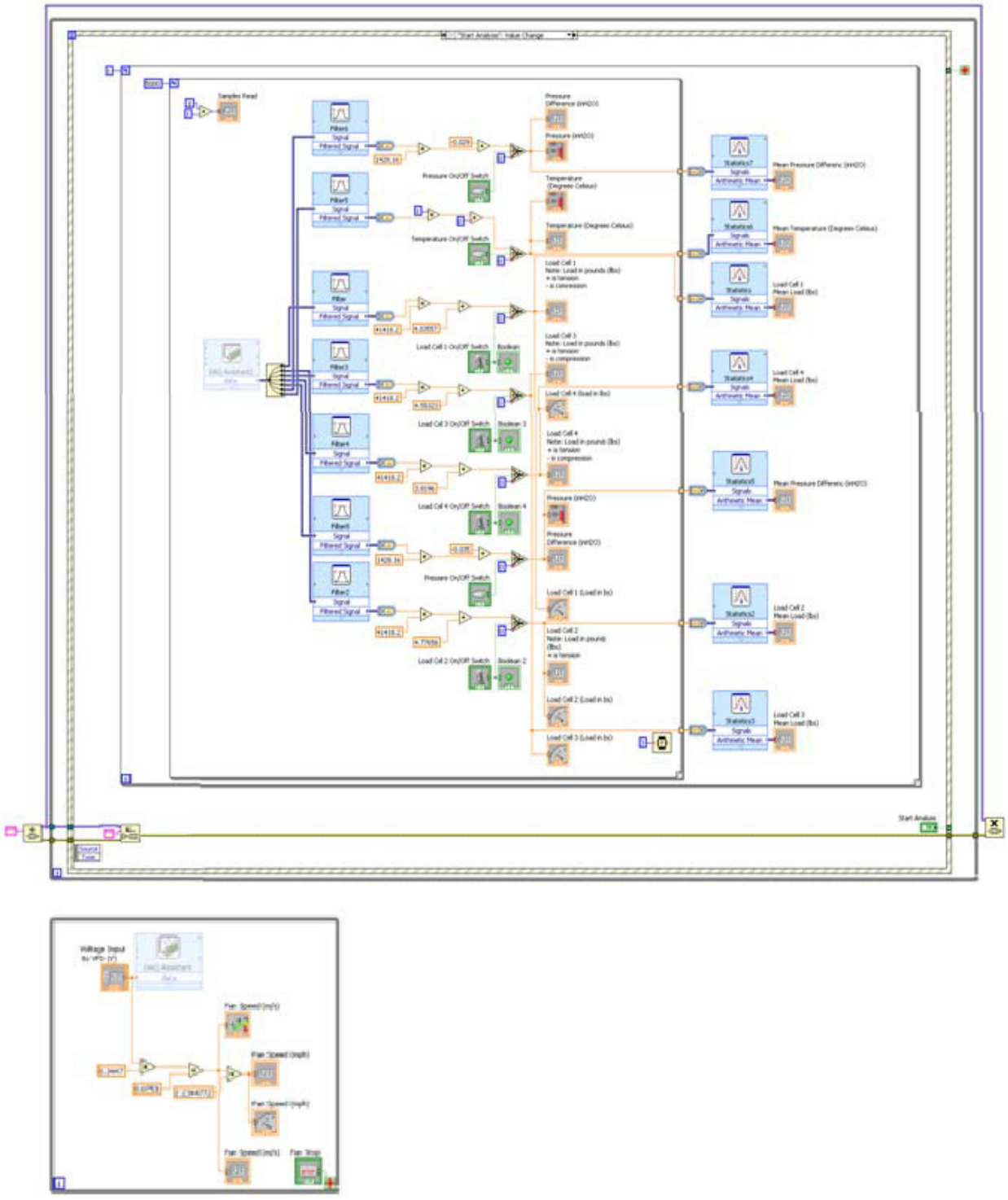

Figure 5.2 LabVIEW block diagram for wind tunnel experimentation. The programming was used to run the fan and measure the lift and drag forces for the various models that were tested in the wind tunnel.

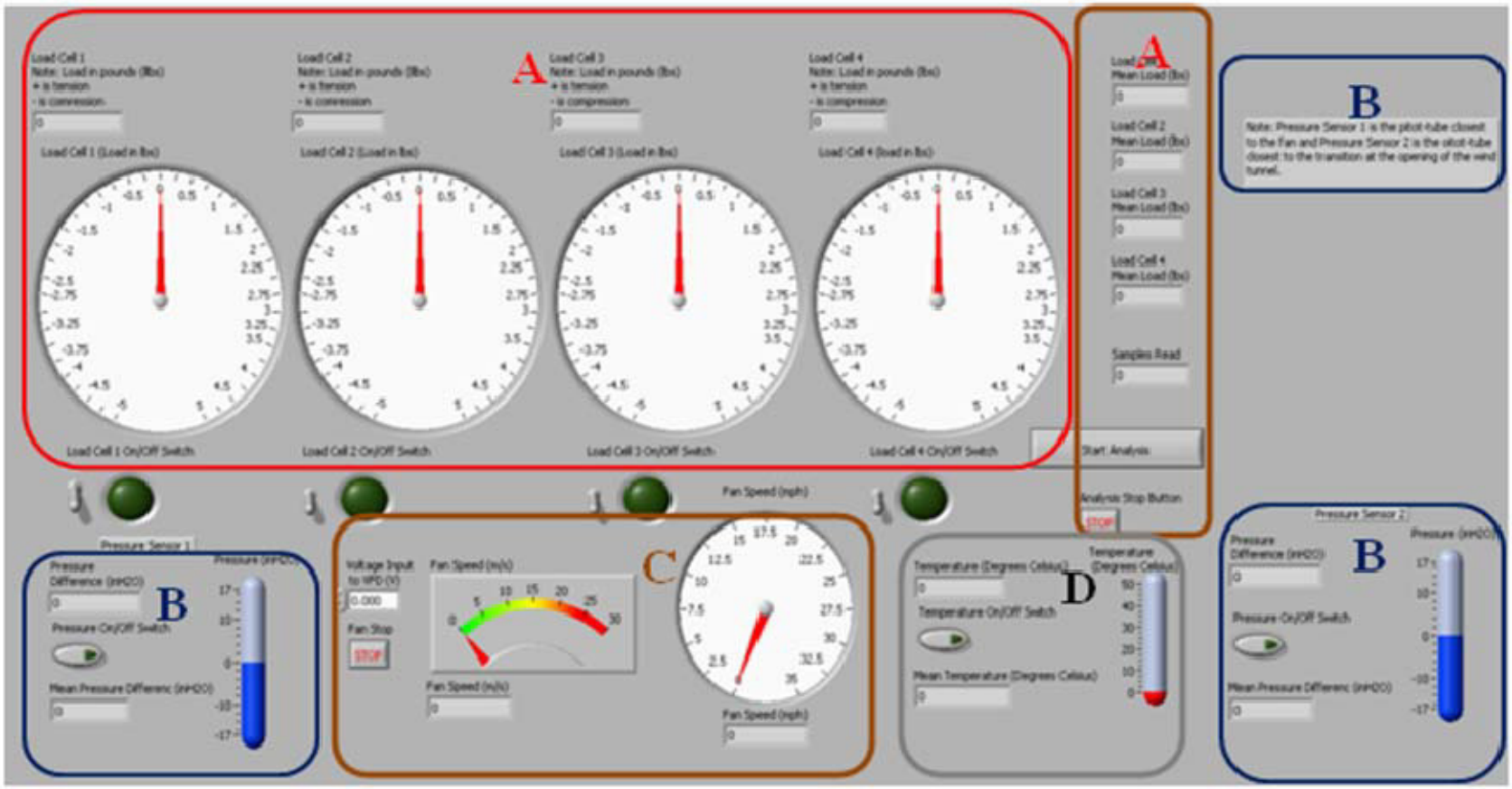

Figure 5.3 Front panel of LabVIEW

5.3 Front panel of LabVIEW design panel of LabVIEW design to measure

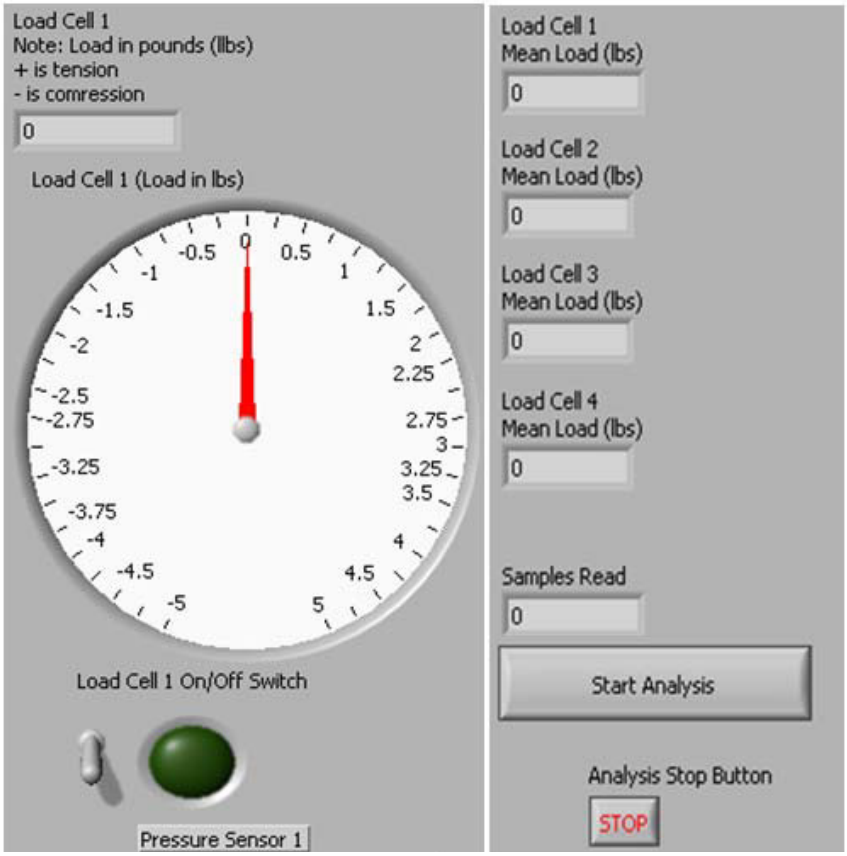

Figure 5.4 Load cell display in LabVIEW front panel (View-A)

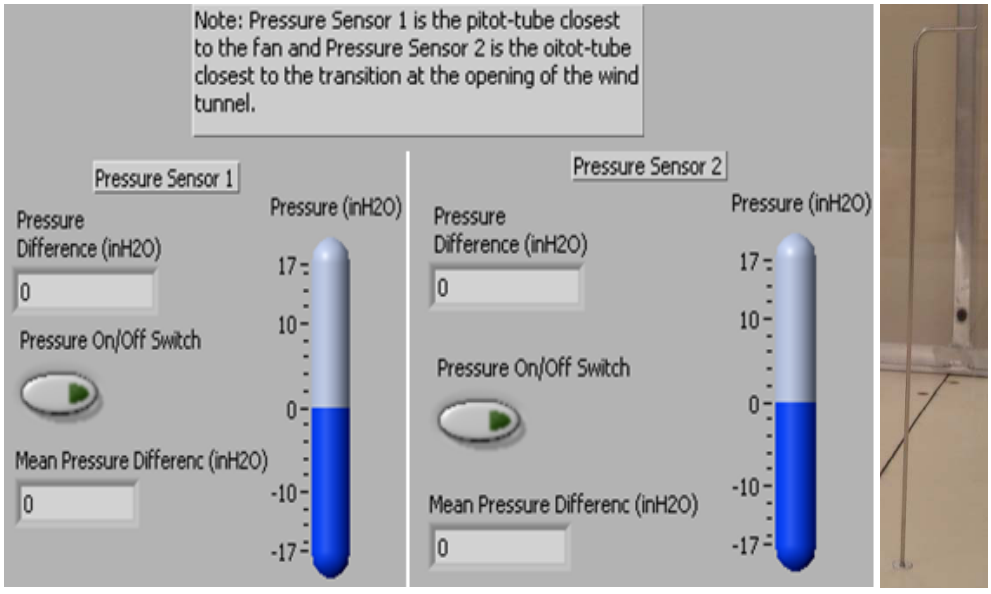

Figure 5.5 Pressure sensors display in the LabVIEW front panel (View-B) *with a photograph of Pitot tube (right)*

Figure 5.6 Fan speed control display in the LabVIEW front panel (View-C) *with a photograph of fan control dial of wind tunnel (right)*

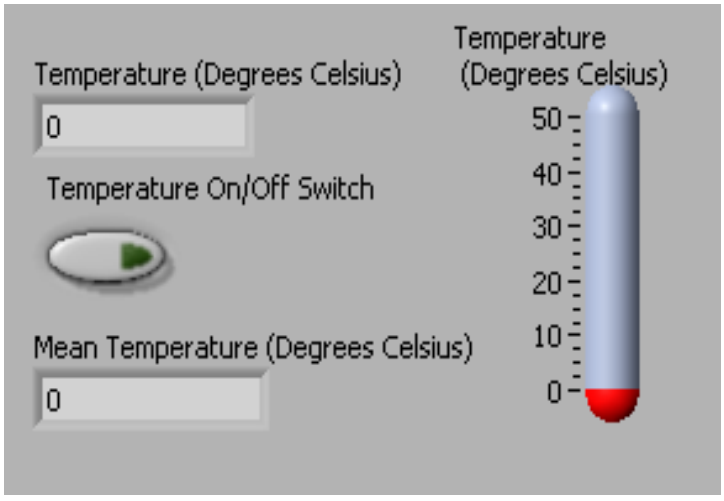

Figure 5.7 Temperatures display in the LabVIEW front panel (View-D)

Followed the block diagram as shown in **Figure 5.2**, corresponding front panel of LabVIEW design to measure loads in wind tunnel is shown in **Figure 5.3**. This panel includes instantaneous and mean force values with digital and analog displays for all four force load cells (A) as further shown in **Figure 5.4**. Pressures were monitored and measured closest to the fan and closest to the wind tunnel opening (B) as shown in **Figure 5.5**. The panel is also designed to control and measure the fan speed (C) as shown in **Figure 5.6**. Even though study for the temperature variations was out of the scope for this study, the temperatures (D) were not observed to significantly vary in all wind tunnel tests, but it can be recorded as shown in **Figure 5.7**.

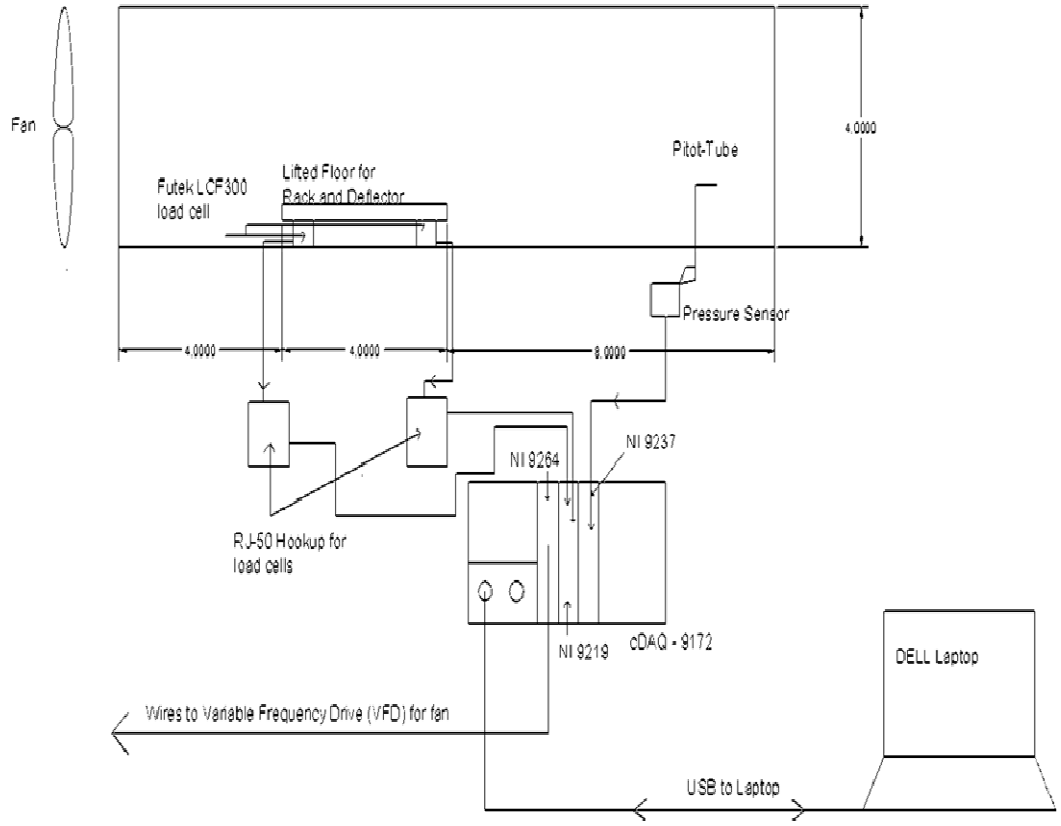

Figure 5.8 Wind tunnel set-up and instrumentation block diagram with accessories (not in scale, in ft.)

Figure 5.9 Wind tunnel instrumentation used for the measurement of

5.9 Wind tunnel instrumentation used for the measurement of wind

Wind tunnel block diagram and instrumentation is shown in **Figures 5.8** and **5.9** respectively. A photograph as shown in **Figure 5.10** below depicts the setup of four load cells that were placed on the testing floor. The test models were mounted on them for wind uplift force measurement. Similar setup was made for wind drag force measurement except the load cells were oriented at right angles compared to the position of load cells for lift force measurement.

Figure 5.10 Photograph of wind tunnel instrumentation showing load cells on the testing floor for wind uplift force measurement

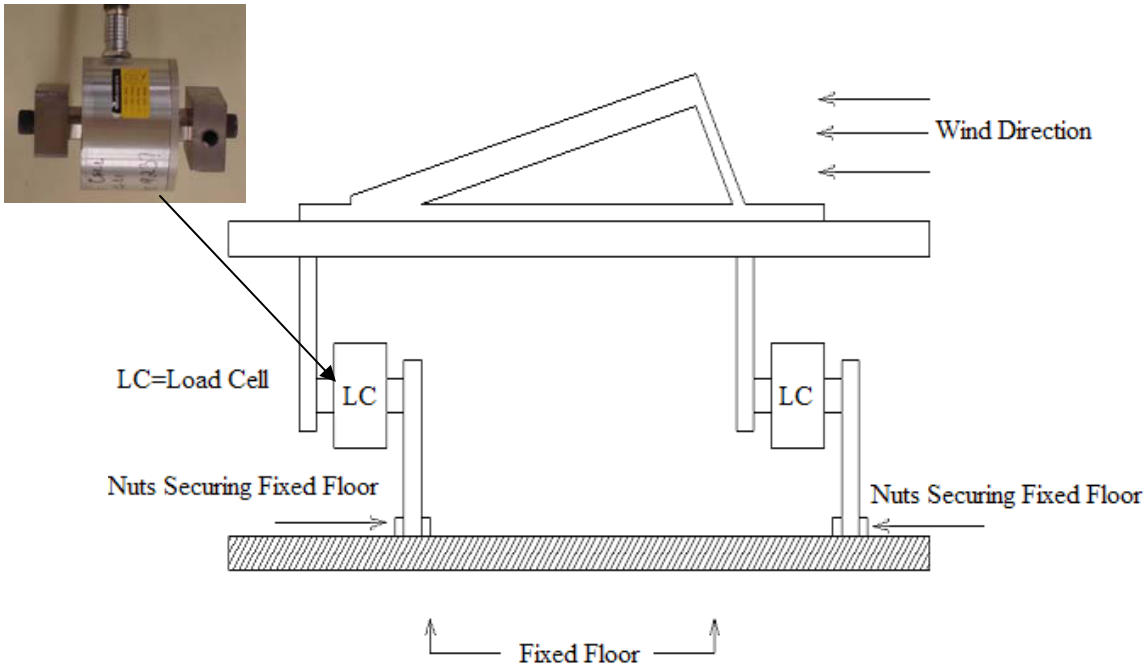

Figure 5.11 Load cell placement (horizontal) for the drag force measurement including a load sensor photograph

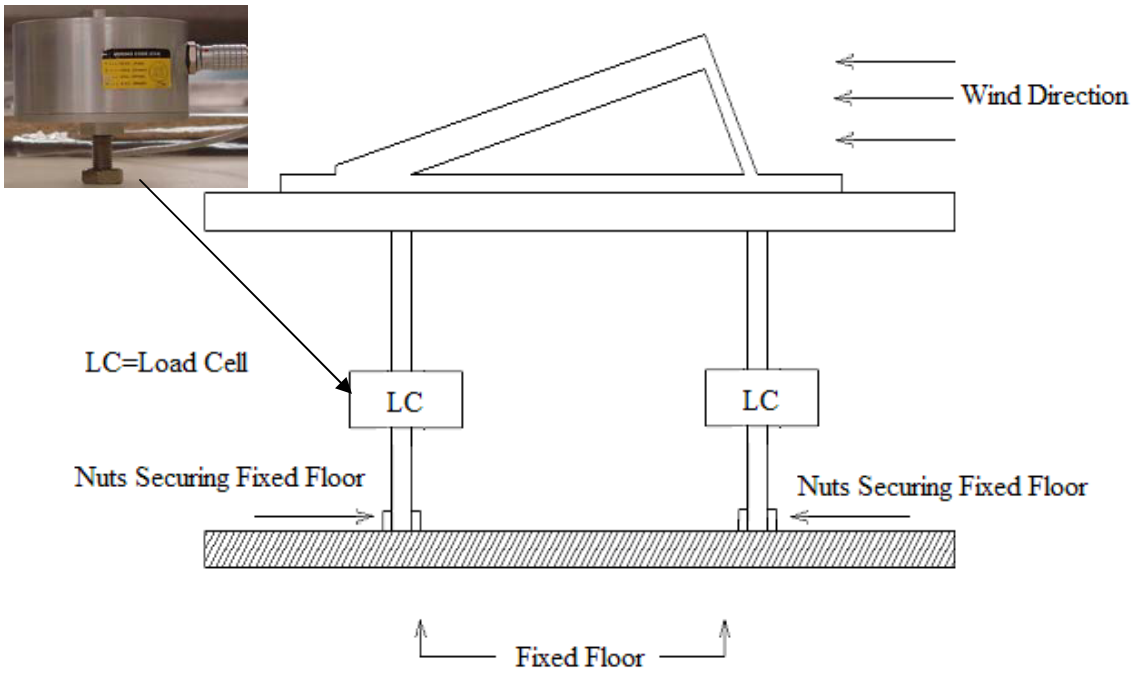

Figure 5.12 Load cell placement (vertical) for the lift force measurement including a load sensor photograph

Wind tunnel instrumentation used for the measurement of uplift and drag forces is as shown above in **Figures 5.11** and **5.12**. The experimental set-up for wind uplift and drag forces were not done simultaneously and were measured by two separate wind tunnel experiments. The load cells were aligned in a vertical and horizontal orientation for the measurments of the lift and drag forces, respectively. The setting of the wind tunnel allows the fan to generate wind speeds up to 27 mph within the wind tunnel testing space. Test models were placed on a melamine board and the melamine board was placed on top of four load cells. The board experienced uplifts and drag forces, which was experienced by the load cells. The load cells transmitted the data in the form of an electrical signal that was then received by the respective NI module and transmitted to the laptop. The load cell placement for the lift and drag measurements is shown in **Figures 5.11** and **5.12**.

It should be noted that non-simultaneous measurements of wind uplift and drag forces may yield some uncertainty and below 5% error in wind tunnel test data when compared to the measurement of wind forces on these models. In fact, rooftop solar panel racks simultaneoulsy experience lift and drag forces caused by high wind speeds. Measurements recorded by isolating one of the forces at a time, may yield the some error.

CHAPTER 6

RESULTS AND DISCUSSION

Based on the discussions in the previous chapters, the goal of this thesis work was to validate the CFD software via scaled wind tunnel tests in order to pick the optimal deflector design. The results from the wind tunnel tests provided good verification for the simulation results from the CFD software. The wind tunnel tests were performed in order to run future computer simulations for different geometries and obtain a reasonable level of accurate and confident results. The meshing parameters and set-ups for the 2-D analyses were consistent for all of the models. This choice was made for the various geometries, as described in **Chapter 2**, in order to compare and provide consistency for the results obtained; the same holds true for the 3-dimensional CFD models. Once all the models were simulated and tested, the results from ANSYS Fluent and the wind tunnel were compared and appropriate concluding remarks were made. The model set-ups and results are discussed in this section along with a brief conclusion and suggestions for future work to follow.

6.1 ANSYS Fluent Simulation

2-D Set-Up

The model that was generated and meshed in ANSYS Workbench was imported into ANSYS Fluent for the simulation phase of the analysis. Flow model and initial conditions were selected in Fluent before the simulation was started. These conditions include, but were not limited to, the selection of the flow model, turbulence

specifications, setting-up initial conditions and convergence criteria. **Figures 6.1** and **6.2** display the mesh characteristics for the models utilized in Fluent. The default constants generated in ANSYS Fluent for the chosen k-epsilon, turbulence model were not changed due to reasons described in **Chapter 3**. There are several steps that are taken in order to set-up, simulate, and post-process the results in ANSYS Fluent.

Details of "Mesh"	
Defaults	
Physics Preference	CFD
Solver Preference	Fluent
Relevance	0
Sizing	
Use Advanced Si...	On: Fixed
Relevance Center	Fine
Initial Size Seed	Active Assembly
Smoothing	Medium
Min Size	1.e-003 m
Max Face Size	Default (0.256720 m)
Max Size	Default (0.513440 m)
Growth Rate	1.020
Minimum Edge Le...	9.525e-003 m
Inflation	
CutCellMeshing	
Active	No
Advanced	
Defeaturing	
Statistics	

Figure 6.1 Initial mesh conditions in ANSYS Fluent

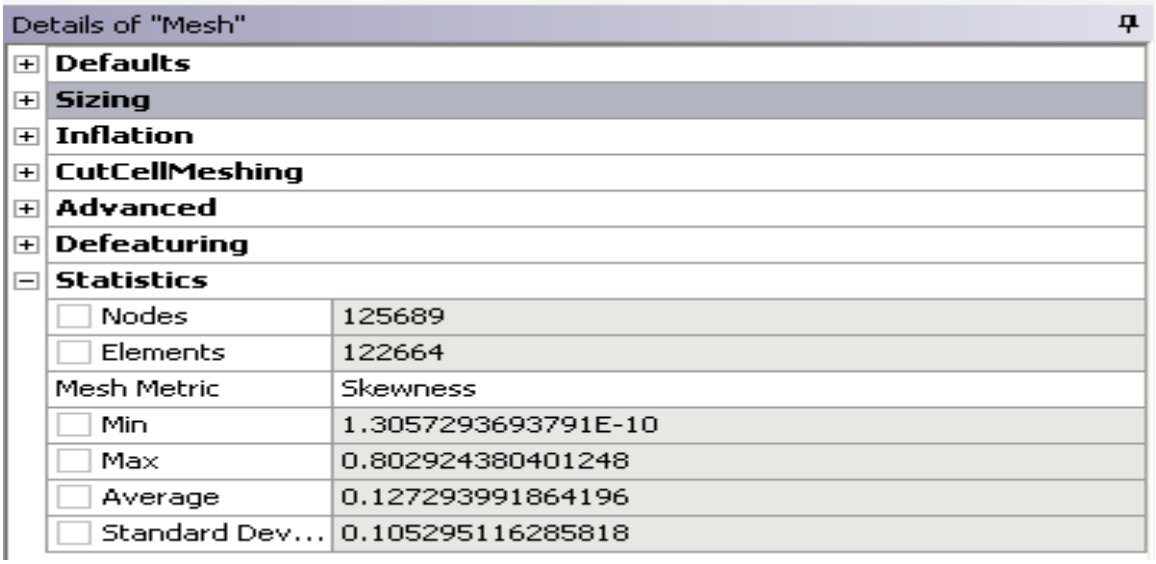

Figure 6.2 Mesh characteristics in ANSYS Mesh

The mesh of the model that was created in ANSYS Meshing was automatically imported to ANSYS Fluent when "Setup" was selected from the box in the project schematic. Once the mesh was imported, it was then necessary to select the proper solver and parameters for the physical model that suits the analysis. **Figures 6.3** and **6.4** were the initial set-up screen once ANSYS Fluent program was started.

Figure 6.3 Problem setup in ANSYS Fluent

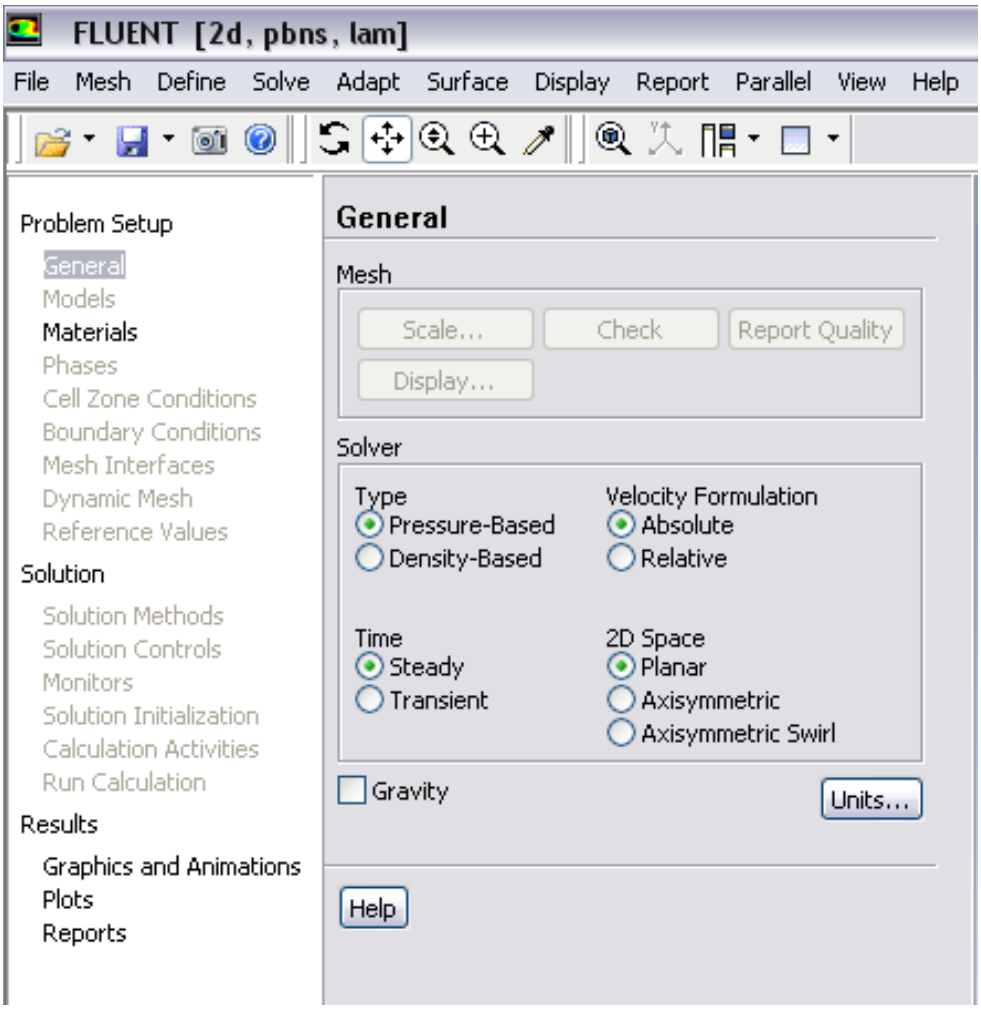

Figure 6.4 General problem set-up in Fluent (View- A from **Figure 6.3**)

The material properties of the geometries and the domains that were created in ANSYS Design Modeler needed to be defined as a fluid, solid, or a mixture. The rest of the set-up involved the setting of the initial conditions, the convergence criteria, and any other monitors to observe convergence of continuity, momentum, and turbulence. The residuals are the convergence criteria that ANSYS Fluent checks for a converged solution. These residuals included continuity, x- and y-components of velocity, k, and ε. The residuals were dependent upon the solver and physical model chosen at the beginning of the set-up. In addition to the residuals, the coefficients of lift and drag were

also monitored for convergence during simulation for validation. The last step was to initialize the flow field from the inlet boundary condition and set the amount of iterations that ANSYS Fluent would run before a converged solution was achieved. If the solution converged before the set amount of iterations, ANSYS Fluent automatically stopped. The steps for the simulations that are contained within this thesis are found below.

Solver

Type	Pressure Based
Velocity Formulation	Absolute
Time	Steady

Model

Viscous	
Model	k-ε (2 equations)
k-epsilon model	Standard
Near-Wall Treatment	Standard Wall Functions
Model Constants	$C_{1\varepsilon} \equiv 1.44$, $C_{2\varepsilon} \equiv 1.92$, $C_{\mu} \equiv 0.09$

Materials

Air	
Material Type	Fluid
Density (kg/m^3)	Default
Viscosity (kg/m-s)	Default
Cell Zone Conditions	
Operating Conditions	
Operating Pressure (Pa)	0

Boundary Conditions

Inlet	
Velocity Specification Method	Magnitude and Direction
Reference Frame	Absolute
Velocity Magnitude (m/s)	12.07
Component Flow Direction	(-1, 0, 0)
Turbulent Intensity (%)	Default (10%)
Turbulent Viscosity	Default (10)
Outlet	
Backflow Specification Method	Normal to Boundary
Gauge Pressure (psi)	0
Specification Method for k-ε	Intensity and Viscosity Ratio
Turbulent Intensity (%)	Default (10%)
Turbulent Viscosity Ratio	Default (10)
Wall	
Wall Motion	Stationary Wall
Shear Condition	No Slip
Roughness Constant	0.5

Solution Methods

Scheme	Simple
Momentum	2^{nd}
Turbulent Kinetic Energy	2^{nd}
Turbulent Dissipation Rate	2^{nd}

Reference Values

Compute From – Inlet

Monitors

Residuals – print, plot	1e-06
Drag – print, plot	(-1, 0, 0)
Lift – print, plot	(0, -1, 0)

Solution Initialization

Compute From – Inlet	Initialize

Calculation Activities

Autosave Every 1000 Iterations

Save Data File Each Time

Run Calculation	20,000 Iterations

3-D Set-Up

A similar set-up that was used for the 2-dimensional analysis was used for the 3-dimensional analysis with the exception of the type of analysis that was selected. Instead of 2-D analysis, 3-D analysis was selected.

6.2 CFD Results of Wind Loads

ANSYS Fluent determines the lift and drag forces in a way similar to that of the traditional methods found in text books. The traditional method of finding the lift and drag forces is found by using the fluid density and velocity of the medium in which the model is submerged, along with the projected area of the model against its respective plane. For example, if the lift force is to be determined on a given model, the projected

area of the model that would be of importance would be the area projected onto the x-z plane, given the standard Cartesian coordinate system. The last remaining variable to calculate the force would be the coefficient of lift for the given model. For simple geometries, the coefficients of lift and drag have been found over years of experimental data and can be found in any relevant text book. **Equations 6.1** and **6.2** are the main governing equations used to solve for the lift and drag wind forces.

$$F_L = \left(\frac{1}{2}\rho v^2 A_L\right) C_L \tag{6.1}$$

$$F_D = \left(\frac{1}{2}\rho v^2 A_D\right) C_D \tag{6.2}$$

Where,

$F_L \equiv$ Lift force

$F_D \equiv$ Drag force

$C_L \equiv$ Coefficient of lift

$C_D \equiv$ Coefficient of drag

$A_L \equiv$ Projected area on z-x axis for lift

$A_D \equiv$ Projected area on x-y axis for drag

Figure 6.5 depicts the projected area for the drag and lift coefficient calculation. The method in which ANSYS Fluent solves for the defined lift or drag forces is by summing the dot product of the pressure and viscous forces on each face with the specified force vector.

The specified force vector, in Cartesian coordinates, is the X-, Y-, and Z-components. In the case of this thesis the specified forces vectors would strictly be the X- and Y-components.

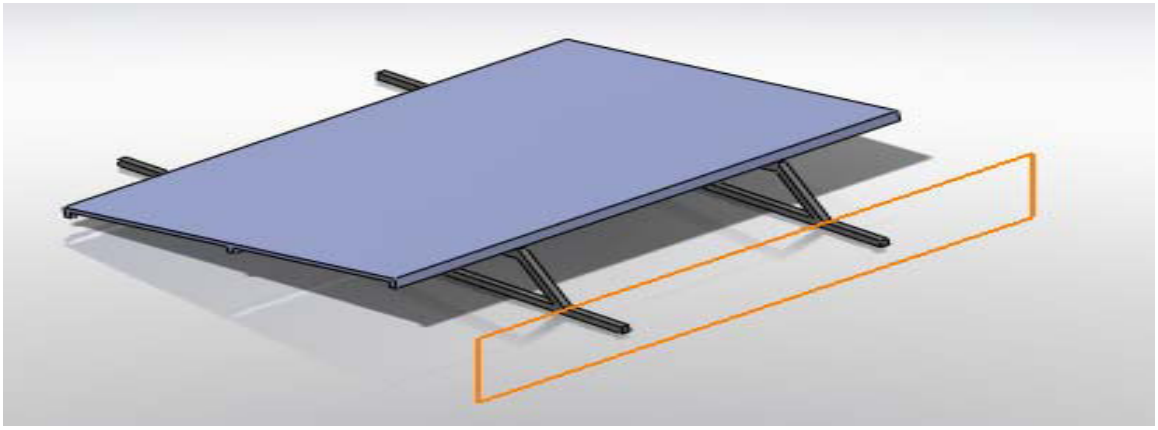

Figure 6.5 Projected areas of an inclined rack displayed for lift and drag forces. The shaded region beneath the panel is the projected area onto the x-z plane and the region outlined in orange is the projected area onto the x-y plane.

ANSYS Fluent determines the forces on a model using the following **Equation 6.3**.

$$F_a = \vec{a} \cdot \vec{F}_p + \vec{a} \cdot \vec{F}_v \tag{6.3}$$

Where,

$\vec{a} \equiv$ specified force vector

$\vec{F}_p \equiv$ pressure force vector

$\vec{F}_v \equiv$ viscous force vector

When comparing the two methods, the noticeable difference is the absence of the force coefficient (lift or drag) in the ANSYS Fluent equation. Although ANSYS Fluent

does not include this coefficient in its equation, the coefficient is found in a similar manner to the traditional method of solving for the lift and drag forces. In order to solve for the lift and drag force coefficients, simply solve for C_L and C_D in **Equations 6.1** and **6.2.**

2-D CFD Results

The preliminary results first generated by the three-dimensional CFD models and the two-dimensional results provided initial insight into the dynamics of flow above and around the conceptual solar panel arrangements with and without deflector. The finned-elliptic deflector identified the influence that a curved shaped deflector has on the flow characteristics of the wind before, on, and past the deflector. Since these characteristics are now known, it was possible to determine the lift and drag coefficients on the panel. The comparison between wind-tunnel and 2-D CFD results suggests that the flow field over, inside and around the solar panel may be influenced by three dimensional effects; geometrical approximation in terms of positioning and drawing the models for 2-D analysis could have also had an influence on the results. The wind penetrates throughout the gaps between the roof surface and the bottom surface of the model as well as the interior supports preventing uniform distribution of air flow. The supports caused strong three dimensional flow patterns.

Static pressure contours, velocity contours, and velocity vectors for flow over the 2-D CFD models (quarter scale and full scale) and 3-D models (full scale) are displayed in **Figures A.13 – A.30** found in the Appendix. The comparisons between the measured data and CFD data were good enough to validate the use of CFD calculations for comparative solar panel rack systems performance on the aerodynamic stability. Quarter

scale models used for 2-D analysis include single rack only, single rack with deflector, three racks only and three racks with deflector. In addition, the full scale models used for 2-D analysis were five racks only and five racks with deflector.

All of these simulations were performed at least three to five times to make sure there was good agreement between the simulation results for each 2-D model. The length of the simulations varied from overnight to a couple of days. There was a significant amount of time spent to first validate CFD codes with several other models of simple geometries relevant to this study. A simple cylinder, vertical flat plate, inclined plate, horizontal flat plate, sphere and other bluff bodies were simulated at three different speeds with the lift and drag coefficients being determined for each simulation. Compared to the theoretical coefficients of lift and drag, computational results had shown very close approximations in all of the models mentioned, below 15% error. Based on the code validation, ANSYS Fluent displayed a very close and reasonable approximation of wind loads within 10% error with experimental data and when compared with standard theoretical studies. Therefore, these studies confirmed the validity and capability of the ANSYS Fluent codes to be used to simulate wind loads for the solar panel rack and deflector models.

Table 6.1 displays the CFD results for a set of full scale models with input wind velocity =110mph. The use of the deflector for both arrangements, single rack and five rack model, wind uplift and drag forces were computed to be reduced by at least 50%; these results are found in **Table 6.2.**

Table 6.1 Reduction in wind loads predicted by CFD results for full scale models with input wind velocity=110mph.

Full-Scale Models	2-Dimensional CFD Results (lbf)	
	Lift Force, F_L	Drag Force, F_D
Single Rack Only	539	850
Single Rack and Deflector	-69	565
5 Racks Array	1662	1000
5 Racks Array and Deflector	764	670

3-D CFD Results

The static pressure contours displayed by 3-D simulations were modified from their 2-D counterparts by the presence of cross-flow circulations and the blocking effects of the internal solar panel rack support rails. Inclusion of these differences from the flow field in the calculations may lead to significant improvement in the computational predictions of wind loads. There was reasonable agreement found between the 2-D, quarter scale simulations and the wind tunnel simulations for both lift and drag forces. The comparison between wind tunnel test data and CFD data was good enough to validate the use of CFD simulations for future solar panel rack systems. Due to the requirements of higher mesh quality and the lengthy computational time, 3-D simulations were not effectively accomplished or sufficiently studied. However, preliminary works demonstrated the reductions of wind loads on the solar panel rack with the recommended deflector in the 3-D CFD studies. Two specific scenarios were studied in 3-D and included a single rack with deflector and 5-racks with deflector. The 3-D simulation

results were compared with the 2-D simulations and a reasonable agreement was observed. Detailed 3-D studies, similar to the 2-D studies presented in this thesis were not performed and are recommended for future work.

Table 6.2 Reduction in wind loads predicted by CFD results for full scale 3-D models with input wind velocity=110mph.

Full-Scale Models	**3-Dimensional CFD results showing percent reduction by using deflector**	
	Lift Force, F_L	Drag Force, F_D
Single Rack Only	-112.8	-33.53
Single Rack and Deflector		
5 Racks Array	-54.03	-32.99
5 Racks Array and Deflector		

6.3 Wind Tunnel Experimentation

The solar panel racks for wind tunnel testing were set-up in four simple steps and are outlined below.

Step 1 – Determine type of test (i.e. measure the lift or drag forces)

Step 2 – Determine type of model (e.g. rack only, deflector only, etc.)

Step 3 – Connect the DAQ system to the computer and calibrate sensors

Step 4 – Turn on fan and begin recording measurements

There were five different models that were each tested for lift and drag, giving a total of ten tests that were conducted. The five models included, single rack only, single rack with deflector, deflector only, three racks only, and three racks with deflector.

In the paragraphs that follow, a detailed description of steps 1-4is presented for the single rack only model. Two melamine boards were used during the set-up of the wind tunnel. The first melamine board served as to fully enclose the load cells inside the tunnel; negating the effects from pressure differences created from the air flow through the tunnel and entrainment of air. This entrainment of air could cause unwanted effects on the board. The first board was placed on four, 4-inch long bolts with nuts already attached, so as to serve as a platform for the board to rest on. Next, four more nuts were attached to the four bolts to secure the bottom (first) board in place. The four Futek LCF 300 load cells were then attached to the bolts to measure the vertical force on the model, or in other words the lift force. (Referring to **Chapter 2,** the position of the load cells for respective lift force measurement is displayed). The model was then attached to the second board before being attached to the load cells. Once secured, the model was put in place on the load cells. It should be noted that the load cells were not touching the nuts that secured the bottom board. The reason for this is so the bottom board would not interfere with the load cells and ultimately, supply erroneous results. The gap around the bottom board was then sealed with clear packaging tape in order to prevent the air outside the tunnel from being sucked-in and causing a false uplift on the model. The wind tunnel was sealed, and thus completed the first step of the experiment.

The connecting wires for the load cells, the variable frequency drive (VFD) for the fan, and the pressure sensors for the Pitot-tubes were attached to their corresponding module. (The modules included the NI 9219, NI 9237, and the NI 9264). The NI 9219 is a universal module that can be used as a full bridge, thermocouple, analog input, and

many other uses. In the case of the experiment, the NI 9219 was configured to be a full-bridge with an excitation voltage of 2.5 volts.

The wires from the pressure sensors were connected to the analog output zero (AO0) and AO1 channels, with the leads being inserted into terminals 3-6 of the respective channel. The NI 9237 was a full bridge module that was used for the load cells to provide the maximum 10 V excitation called for by the load cell manufacturer. The four load cells were connected to Channel 0 (Ch0), Ch1, Ch2, and Ch3 via the RJ50 Cable (10-pin modular plug to pigtail wires). The plug serves as a configuration set-up for the NI 9237. The wires were then attached to terminals 2 and 3 for the positive and negative input signals. Terminals 5 and 7 were for the positive and negative excitation voltage of the RJ50 cable. **Figures 6.6** and **6.7** are representative of the 3 NI modules in cDAQ 9172 along with the RJ50 cable, respectively.

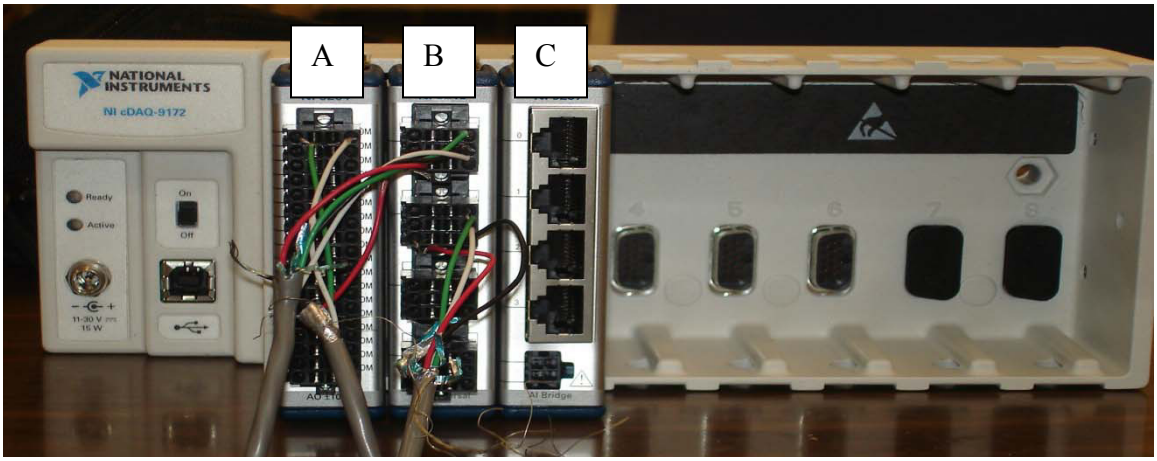

Figure 6.6 Data acquisition system **(**cDAQ-9172 with modules, A: NI 9264, B: NI9219, C: NI 9237)

The final module, the NI 9264, was used as the voltage input to the VFD to control the fan. The maximum supplied voltage was ± 10 volts. The wires were connected to the AO0 and COM terminals. Once everything was connected to the cDAQ-9172, the cDAQ-9172 was connected to the DELL laptop for the final stage of step 2. Once the corresponding program for the wind tunnel was opened, the load cells were zeroed-out and step 2 was completed.

Figure 6.7 RJ50 cable with attachment terminals for load cells

Finally, once steps 1 and 2 were completed, the fan was turned on and the analysis started. Measurements were taken at 4 different speeds, 15, 20, 25, and 27 mph. 5000 readings were taken and averaged for each load cell at each of the first three speeds mentioned above. The readings were averaged and the process was repeated two more times. A total of 15000 readings were taken for each of the 3 speeds. As for the last speed, 27 mph, only 1000 readings were taken and then averaged because the VFD would

shut the fan off before the program could finish the 5000 readings taken at the previous three speeds. Once the final measurement was taken at 27 mph, the analysis of the lift force on the single rack was completed and another model was able to be tested.

The above steps were repeated for the other four models with the exception of the attachment of the wires to the terminals of the cDAQ-9172, since they were already connected. In order to calculate the drag force the load cells were turned horizontally and were attached to the bolts as described in Chapter 2.

6.4 Wind Tunnel Test Data of Wind Loads

As described earlier, measurements were recorded at four different speeds: 15, 20, 25, and 27 mph. The wind tunnel test results are tabulated at the end of the Chapter and are plotted in **Figures 6.8-6.12**. It is to be noted that the load cells were first oriented to measure drag forces, then to measure lift forces for each test configuration and wind speed. Each load cell used in our wind-tunnel testing measures ±50 lbs (full-scale) with measurement uncertainty of 0.25% of full-scale reading. For all five test configurations of the scaled models, the lift and drag forces increased linearly as the wind speed increased from 15 mph to 27 mph. In **Figures 6.8–6.12**, the blue triangles represent the lift force and the purple circles represent the drag force. The solid and dotted lines represent the line of best fit for the drag and lift forces respectively. The summarized results outline the drag and lift forces for various experimental configurations. For deflector-only configuration, the minimum and maximum drag forces were approximately 0.55 lbs and 2.3 lbs respectively as shown in **Figure 6.8**, while the minimum and maximum lift forces were 0.48 lbs and 1.4 lbs. For rack-only arrangement (**Figure 6.9**), the minimum and

maximum drag forces were approximately 0.3 lbs and 1.2 lbs respectively, while the minimum and maximum lift forces were 1.2 lbs and 3.8 lbs.

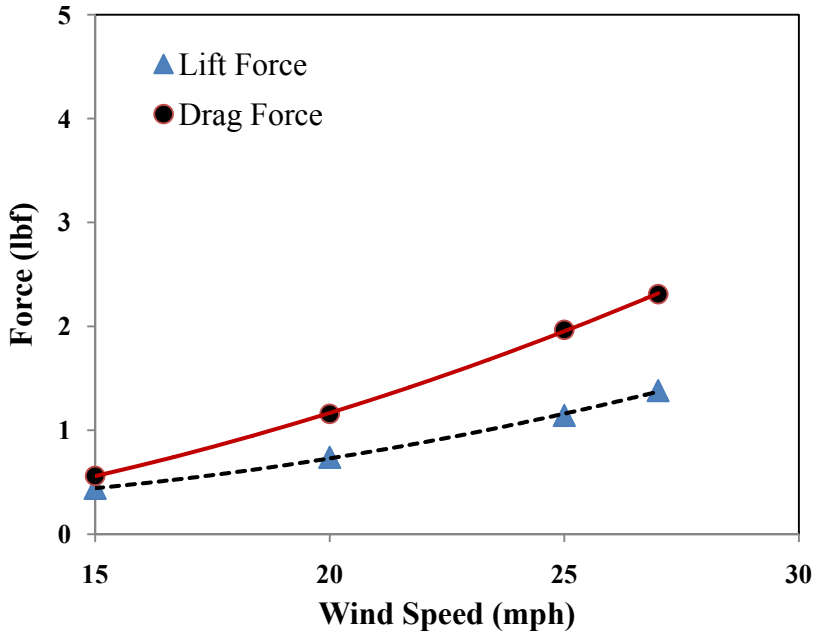

Figure 6.8 Wind force vs. wind speed for deflector-only in wind tunnel tests

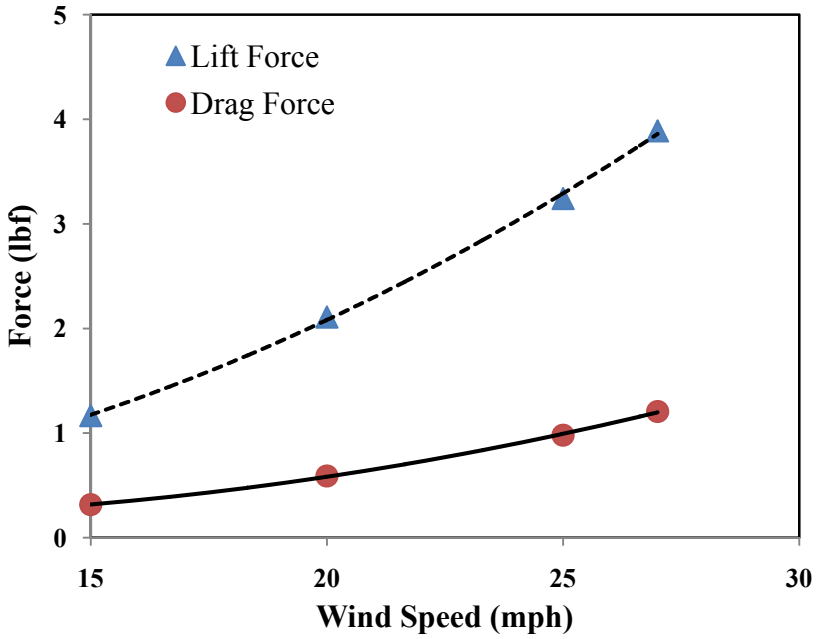

Figure 6.9 Wind force vs. wind speed for single rack-only in the wind tunnel tests

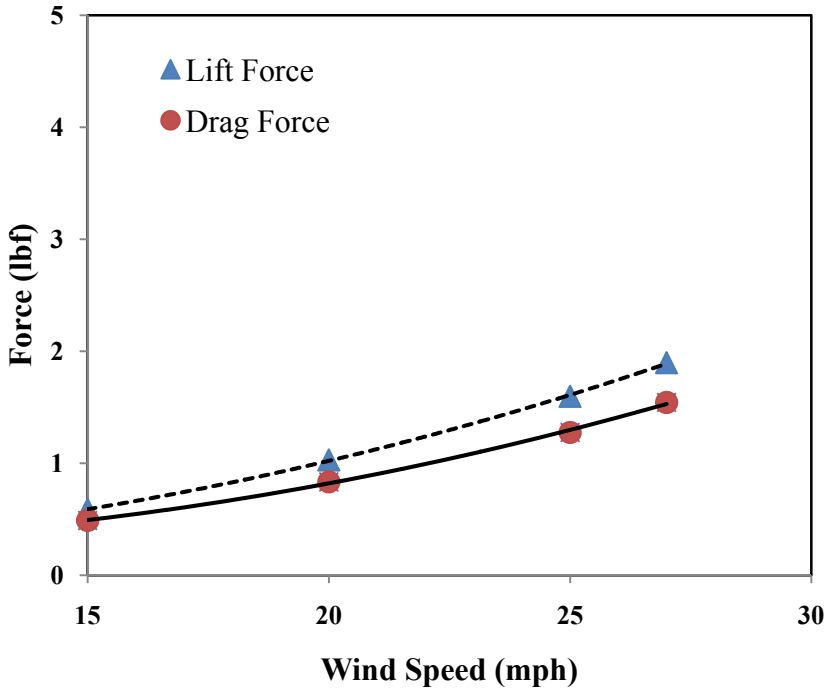

Figure 6.10 Wind force vs. wind speed for a rack and deflector in the wind tunnel tests

For single rack with deflector as shown in **Figure 6.10**, the minimum and maximum drag forces were approximately 0.5 lbs and 1.5 lbs respectively, while the minimum and maximum lift forces were 0.6 lbs and 1.7 lbs. Therefore, it can be concluded purely from the wind tunnel test data, that using the deflector reduces the lift forces for the rack-deflector arrangement by more than 50% for the speeds tested while the drag force does not change significantly. For 3-rack-only as shown in **Figure 6.11**, the minimum and maximum drag forces were approximately 0.45 lbs and 0.85 lbs respectively, while the minimum and maximum lift forces were 1.5 lbs and 4.6 lbs.

As explained earlier, for deflector-only configuration, the minimum and maximum drag forces were approximately 0.55 lbs and 2.3 lbs respectively as shown in **Figure 6.8**, while the minimum and maximum lift forces were 0.48 lbs and 1.4 lbs. Also,

for rack-only arrangement as shown in **Figure 6.9** can be compared with three racks arrangement as shown in **Figure 6.11**. Similarly, a rack and deflector arrangement can now be compared with three racks and deflector arrangement for wind forces. Results clearly show the addition of deflector minimizes the wind forces in both arrangements.

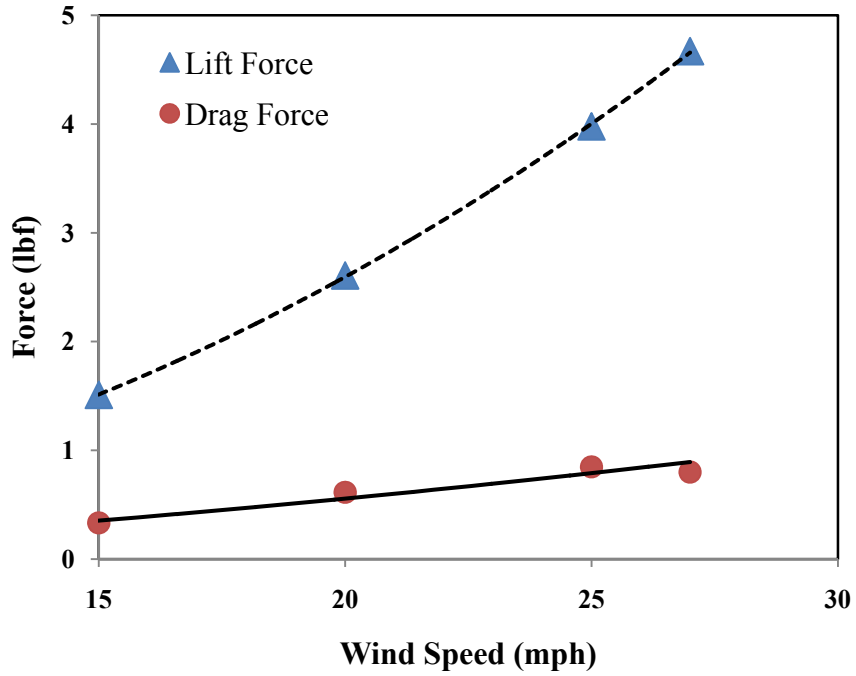

Figure 6.11 Wind force vs. wind speed for three-rack only in the wind tunnel tests

For 3-rack plus deflector model as shown in **Figure 6.12**, the minimum and maximum drag forces were approximately 0.45 lbs and 1.00 lbs respectively, while the minimum and maximum lift forces were 0.8 lbs and 2.5 lbs. Therefore, it appears that one deflector placed in front of the 3-rack array reduces the lift forces by up to 50% without much change in the drag force.

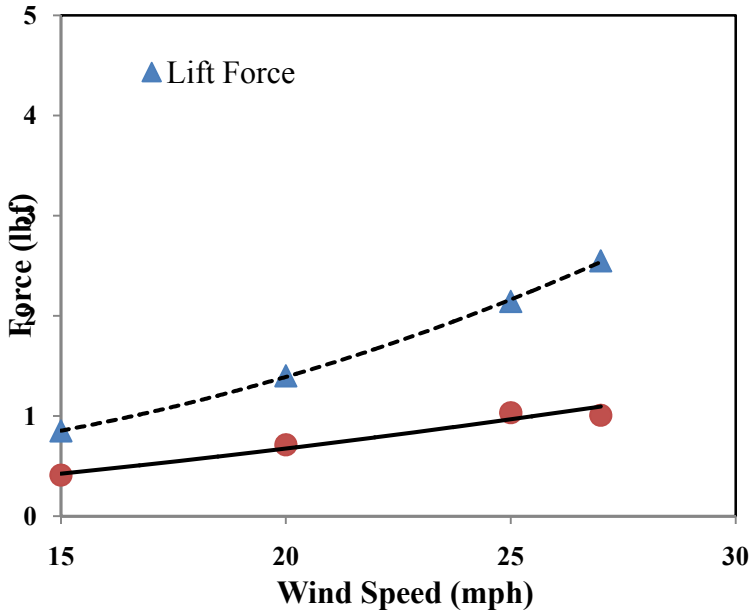

Figure 6.12 Wind force vs. wind speed for three-rack and deflector in the wind tunnel

6.5 Validation and Comparison of Simulation Results with Wind Tunnel Test Data

After checking the validity of the CFD codes, the quarter scale models were simulated and the results were compared side by side with the wind tunnel results. The findings are shown in **Table 6.3**.

Table 6.3 Wind tunnel test data and CFD results for quarter-scale models with input wind velocity=27mph

Quarter-Scale Models for V_{inlet}=27 mph	**Wind Loads (lbf)**			
	Wind Tunnel Data		**CFD Results**	
	Lift F_L	Drag F_D	Lift F_L	Drag F_D
Single Rack Only	3.88	1.2	2.8	2.73
Deflector Only	1.38	2.3	2.08	4.08
Single Rack and Deflector	1.89	1.54	1.76	2.48
3 Racks Array	4.67	0.8	5.99	4.09
3 Racks Array and Deflector	2.54	1.01	2.75	3.25

The percent difference between the CFD and wind tunnel results were calculated in addition to the percent reduction due to inclusion of a deflector. The percent reduction and percent difference were found as follows in **Equations 6.3** and **6.4**.:

$$\text{Percent Reduction (\%)} = \frac{F_{RD} - F_R}{F_R} \cdot 100 \tag{6.3}$$

$$\text{Percent Difference (\%)} = \frac{F_{CFD} - F_{EXP}}{F_{EXP}} \cdot 100 \tag{6.4}$$

Where,

F_{RD} = Respective drag or lift force for rack models with a deflector, experimental or CFD

F_R = Respective drag or lift force for models without a deflector, experimental or CFD

F_{CFD} = Respective CFD result for drag or lift force

F_{EXP} = Respective experimental result for drag or lift force

For a single rack, the reduction of the lift force due to the deflector was found by applying equation 5.1 and using data from the computational analysis. The percent reduction in lift force on single rack due to deflector: F_{RD}= 1.76 lbf and F_{RD}= 2.8 lbf

Substituting F_{RD} and F_R in **Equation 6.3**:

$$\text{Percent Reduction (\%)} = \frac{1.76 - 2.8}{2.8} \cdot 100 = -37.14\%$$

A similar process was followed for the drag force of the single rack model, as well as the lift and drag forces for the 3 rack model. The percent difference between the experimental and CFD results were also found by the same process, using the appropriate values. The percent difference and percent reduction for the models described in **Table 6.3** are shown in **Table 6.4**.

Table 6.4 Wind tunnel data vs. CFD results for quarter-scale models with input wind velocity=27mph.

Quarter-Scale Models for V_{inlet}=27 mph	**Wind Tunnel vs CFD (% Difference)**	**Experimental Reduction Using Deflector (%)**		**Computational Reduction Using Deflector (%)**	
	Lift Force, F_L	Lift Force, F_L	Drag Force, F_D	Lift Force, F_L	Drag Force, F_D
Single Rack Only	-27.84	-51.29	28.33	-37.14	-9.16
Deflector Only	50.72				
Single Rack and Deflector	-6.88				
3 Racks Array	28.27	-45.61	26.25	-54.09	-20.54
3 Racks Array and Deflector	8.27				

The use of the deflector reduced wind uplift by -51.29%, but the experiment showed an increase in the drag force of 28.33% when the deflector was added to the model. It should be noted that if the above values in **Table 6.4** have a negative (-) sign in front, it indicates a reduction if the values do not have a negative sign, it indicates an increase. The CFD analysis resulted in a net reduction of -37.14% and -9.16% for the lift and drag forces, respectively. A similar trend was found in the experimental and computational analysis of the three rack model with and without deflector. The

experimental wind uplift was reduced by -45.61% with the addition of the deflector, but showed an increase in the experimentally determined drag force of 26.25% when the deflector was added to the model. When the two methods were compared for the same model, the wind uplift was closely predicted. For a single rack model, the percent reduction was -54.29% and -37.14% for experimental and computational results, respectively. The percent reduction was even closer when the two methods were compared for the three rack model with deflector; -45.61% for experimental uplift and -54.09% for computational uplift.

In terms of drag results, the experimental results resulted in slight additions to the drag force, for both single rack and 3 rack models using deflector, the addition was around 25%. This addition in wind drag is expected as the addition of deflector with the rack arrays will somewhat increase the amount of drag force. When the respective drag and uplift forces are compared for both the scenarios of single rack only and 3 rack array, drag forces were ~ 70% smaller than the wind uplifts. This comparison explains that the reduction in wind uplifts is more crucial than the wind drag forces for design and installation purposes. Similarly, the drag forces found computationally were found to have been reduced by 9.16% and 20.54% for the single rack and three rack models, respectively, by the application of the deflector. Drag forces between the computational and experimental results did not agree with one another as there were some limitations that existed with two dimensional CFD simulations. These deviations in drag results may be less for 3-dimensional simulations.

CHAPTER 7

CONCLUDING REMARKS AND FUTURE WORK

Overall, the wind loads on the solar panel racks were greatly reduced with the addition of a wind deflector, as expected. The "wall" deflector was used as a way to prove the reduction of the forces, but was not considered to be a viable option. The wedge deflector had favorable results in reducing the wind loads on the solar panel racks, but the amount of down force on the roof exceeded the maximum amount for a load on a rooftop. It was decided to try a more rounded deflector, normal to the wind flow. A quarter circle profile was assessed, which then led to the elliptic profile shaped deflector with fins. The addition of the fins caused the flow to transition quicker to turbulent flow on the surface of the deflector, which in turn reduced the drag force. The elliptic deflector with fins proved to be the best profile, with respect to the other deflectors assessed, in reducing the wind loads on the solar panel racks. Also, the elliptic profile experienced the lowest lift and drag forces of all the deflectors experimented.

The k-ε turbulence model and the wind tunnel results had a reasonable agreement in the trends associated with the models with and without the deflector. The CFD results for the single rack only and single rack with deflector showed the same trend in reduction as the experimental results for the same situation. However, when the CFD results are compared directly with the experimental results, the CFD results deviated from the experimental results. This was due to the limitations of the 2-D CFD analysis.

It is expected the 3-D CFD analysis would provide a more reasonable agreement with the experimental analysis. Also, as stated before, the k- ε turbulence model was the only model considered for the CFD analysis of the research. The reasons for this being the k-epsilon model is the most widely used turbulence model between scientists and engineers. It is possible, however, using the k-ω or RNG turbulence models, to get closer to experimental results.

The main focus of this thesis was the investigation of the lift and drag forces on solar panel racks and how to combat these effects through a wind management system. There are still many opportunities to investigate for future work. Some suggestions would be to change the type and thickness of material of the racks. The racks were given the material properties of aluminum. The geometry of the racks can be changed, more specifically, the angle of inclination. The solar panel racks angled at 10^{o} were investigated because the racks were going to be installed in California. In that area of the United States the azimuth angle was found to be 10^{o}. The azimuth angle is the angle, measured from horizontal, which will provide the optimum energy absorption for solar panels. The rack orientation is highly recommended for future work because of the differences in azimuth angles between cities and states.

The other work that could be investigated would the effect that periodic flow has on the forces of the racks. In the scope of this thesis, steady flow was only considered. As stated earlier, only the lift and drag forces were calculated on the solar panel racks; the moment was not included. The moment would help to determine the force that would cause the racks to tip. The stresses in the racks due to the lift and drag forces could also be researched.

REFERENCES

American Institute of Architects (AIA), 2010, Addressing: http://www.architecture.uwaterloo.ca (visited on 10/27/2010)

Anderson, John David. *Fundamentals of Aerodynamics*. Boston: McGraw-Hill, 2001.

A. Radu and E. Axinte, Wind forces on structures supporting solar collectors, *J. Wind Eng. Ind. Aerodyn.* 32 (1989), 93 pp.

Barkaszi, S.F. and Dunlop, J.P., 2001, Discussion of Strategies for Mounting Photovoltaic Arrays on Rooftops, *Proceedings of Solar Forum 2001, Solar Energy: The Power to Choose*, April 21-26, Washington D.C., 6 pp.

Çengel, Yunus A., and John M. Cimbala. *Fluid Mechanics: Fundamentals and Applications*. Boston: McGraw-Hill Higher Education, 2010. Print.

Fox, Robert W., Alan T. McDonald, and Philip J. Pritchard. *Introduction to Fluid Mechanics*. New York: Wiley, 2004. Print.

G.A. Kopp et al., Wind loads on a solar array, Wind Struct. Int. J. 5 (2002), 393 pp.

G.S. Wood et al., Wind loads on industrial solar panel arrays and supporting roof structure, *WindStruct. Int. J.* 4 (6) (2001), 481 pp.

Healey, H.M., 2009, Florida's Winds Create Installation Problems for Solar Water Heating and Photovoltaic Modules on Buildings, *Introduction to Solar Energy*, Florida Alternative Energy Corporation, http://www.flaenergy.com/pic2r.htm, 2009, 2 pp.

J.D. Holmes, Wind Loading of Structures, Spon Press, London (2001) 72 pp.

Lee, S. and Bienkiewicz, B., 1995, Wind Engineering Study of Power Guard Roofing Technical Report for PowerLight Corporation, Wind Engineering and Fluids Laboratory, Colorado State University, Fort Collins, 192 pp.

M. Oliphant, Measurement of wind speed across a solar collector, *Sol. Energy* 24 (1980), 403 pp.

NAFCO International Inc, 2006-2011, Fond Du Lac, WI. Addressing: http://www.nafcointernational.com/engineering/wind_velocity_map.html (visited on 01/18/2010)

National Hurricane Center and USA National Hurricane Center, USA. Addressing: http://www.nhc.noaa.gov

Neff, D.E. and Bienkiewicz, B., 2000, Wind Tunnel Study of PowerGuard RT Arrays, Technical Report for PowerLight Corporation, Wind Engineering and Fluids Laboratory, Colorado State University, Fort Collins, February, 175 pp.

Neff, D.E. and Meroney, R.N., 2003, *Wind Performance of Photovoltaic Arrays*, Final Report, Wind Engineering and Fluids Laboratory, Colorado State University, 181 pp.

O'Brien, C., 2006, Roof-mounted Solar Photovoltaic Arrays: Technical Issues for the Roofing Industry, *Interface, Trade Journal of RCI, Inc.*, March, 13 pp.

Radu, A., Axinte, E., and Theohari, C., 1986, Steady Wind Pressures on Solar Collectors on Flat-Roofed Buildings, *J. Wind Engr. Ind. Aero*., Vol. 23, 249 pp.

S. Kalogirou, Solar thermal collectors and applications, Prog. Energy Combust. Sci. 20 (2004), 231 pp.

Spratley, W.A., 1998, Solar Rooftops as Distributed Resources, *The Electricity Journal* 11, pp. 40-50

U.S. Energy Information Administration (U.S. – EIA), 2011, *Electric Power Monthly* April Edition. Addresing: http://www.eia.doe.gov (visited on 05/01/2011)

APPENDIX

A.1 Physical Models for Wind Tunnel Testing

Note: All linear measurements are in inch and angular measurements are in degrees. Also note that the figures are not to scale.

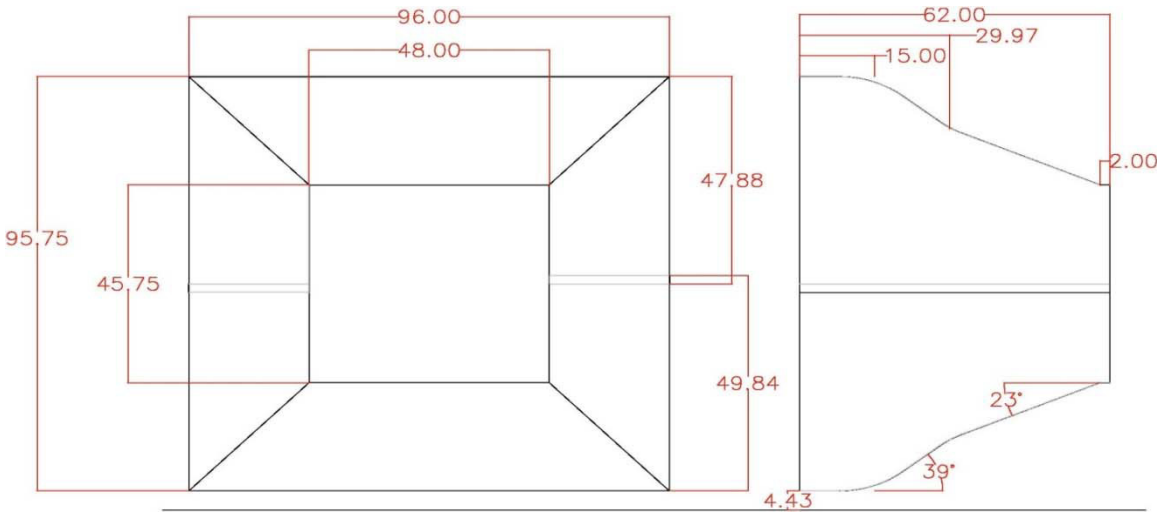

Figure A.1 Flow straightener (Northern States Metals)

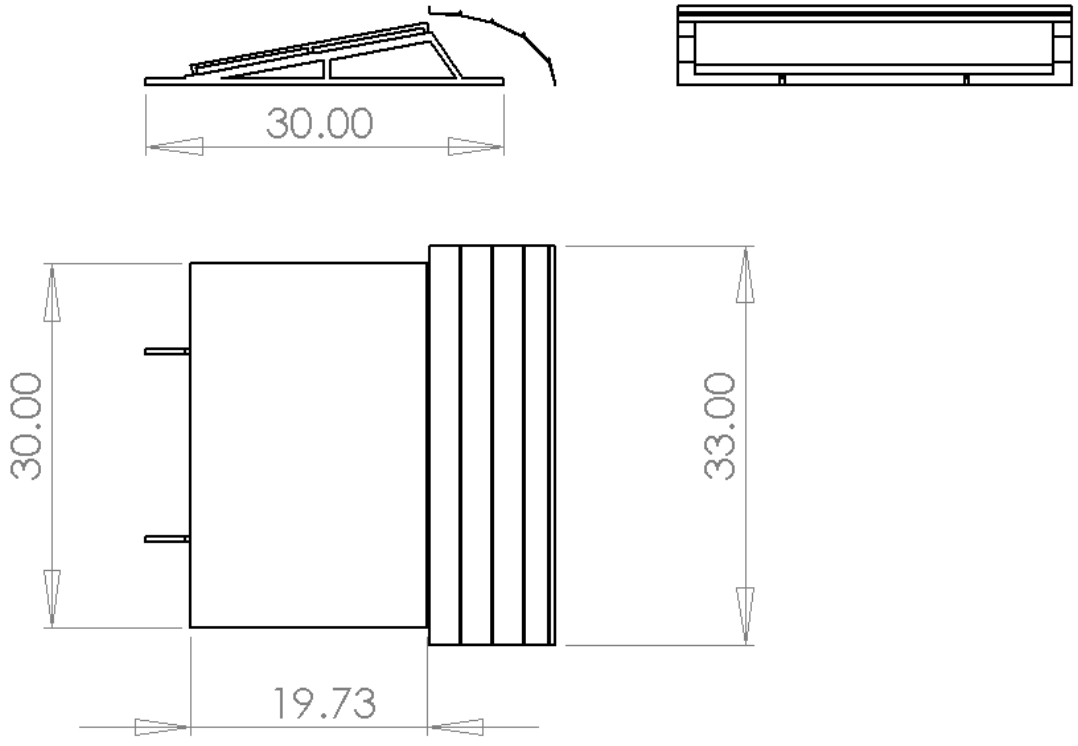

Figure A.2 Detailed drawing of quarter scale, single rack with deflector

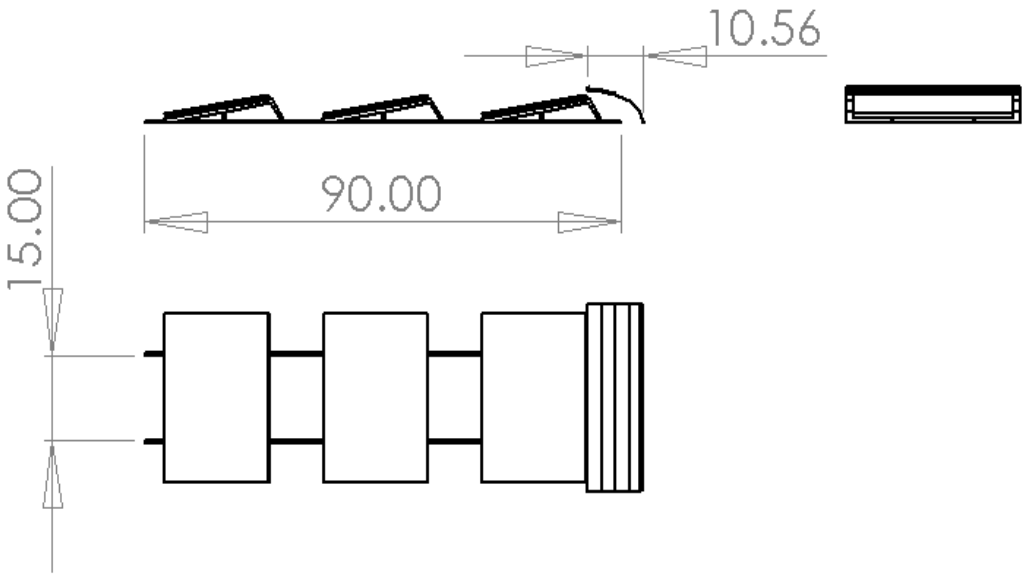

Figure A.3 Detailed drawing of quarter scale, 3 racks with deflector

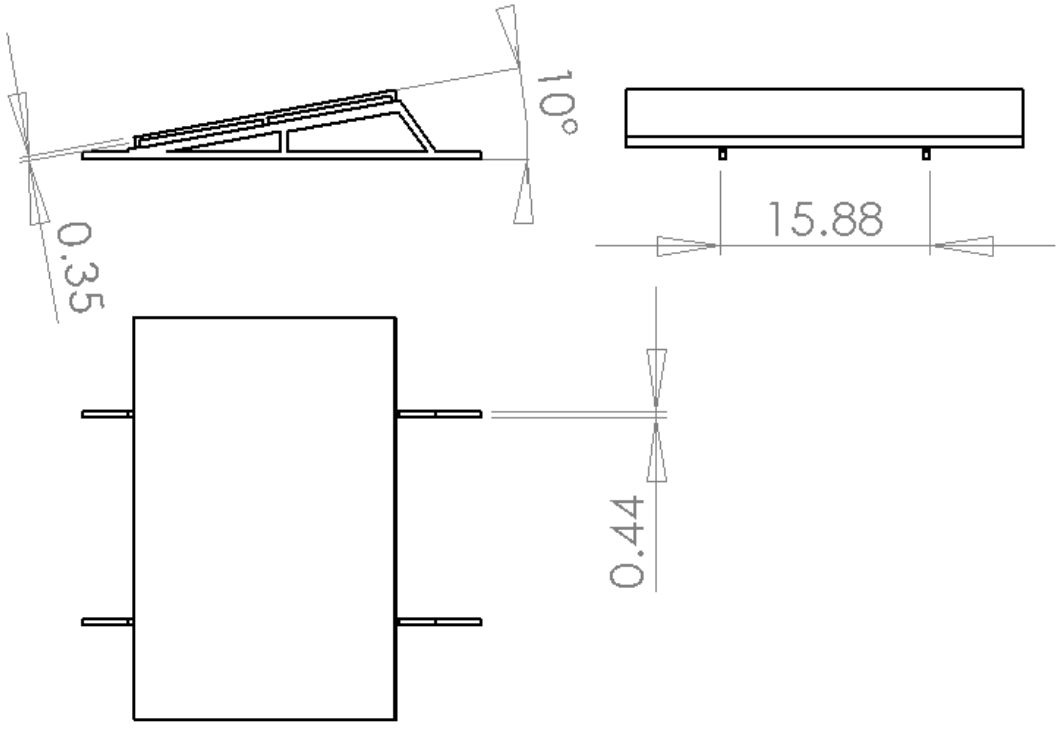

Figure A.4 Detailed drawing of quarter scale solar panel rack

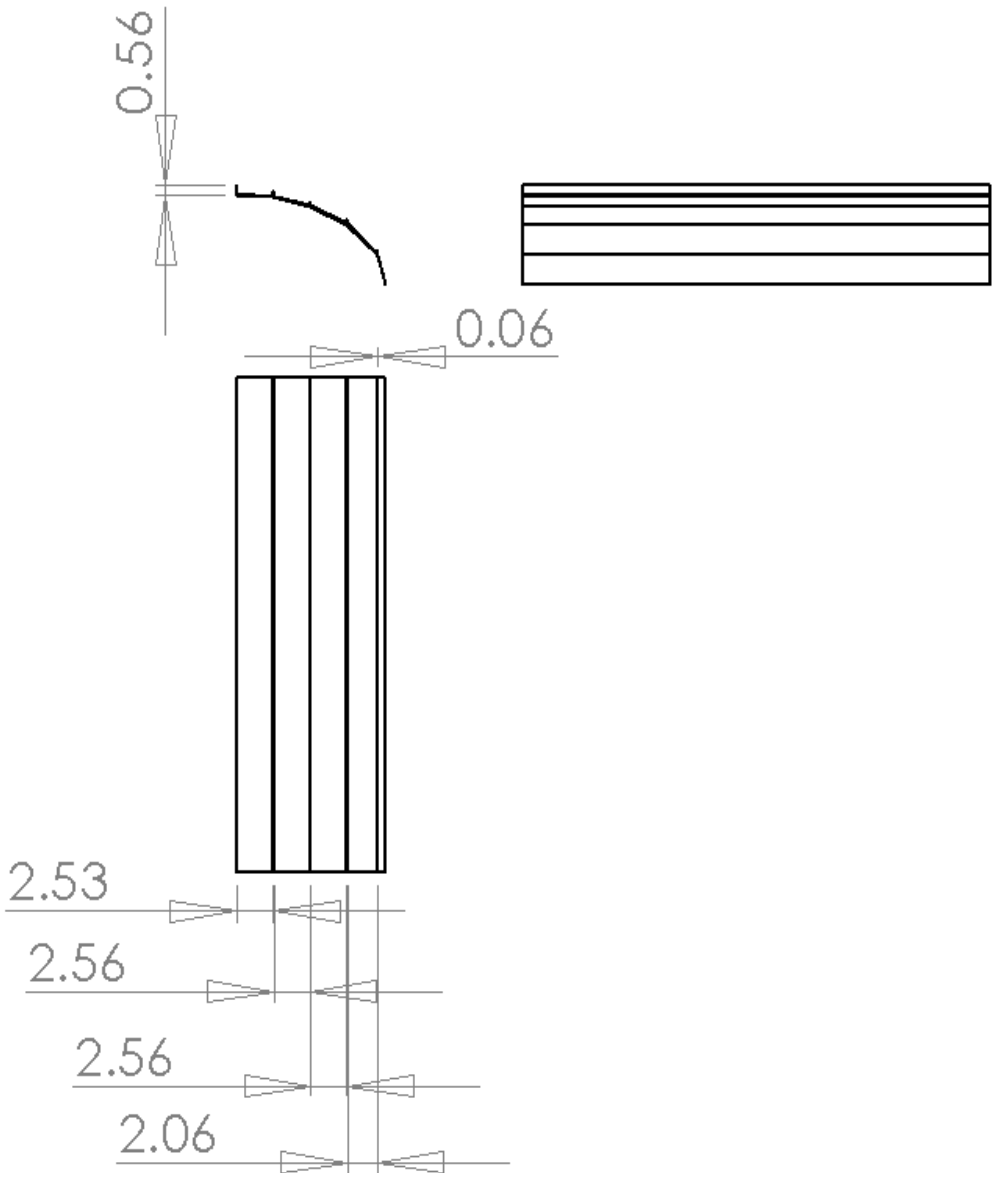

Figure A.5 Detailed drawing of quarter scale deflector

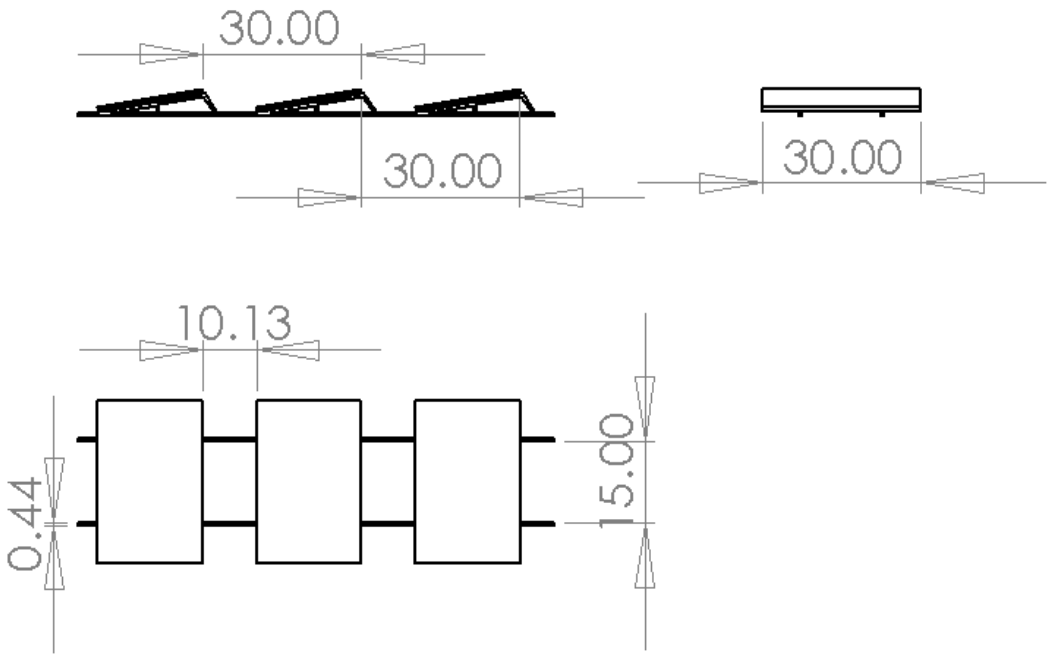

Figure A.6 Detailed drawing of quarter scale, 3 racks

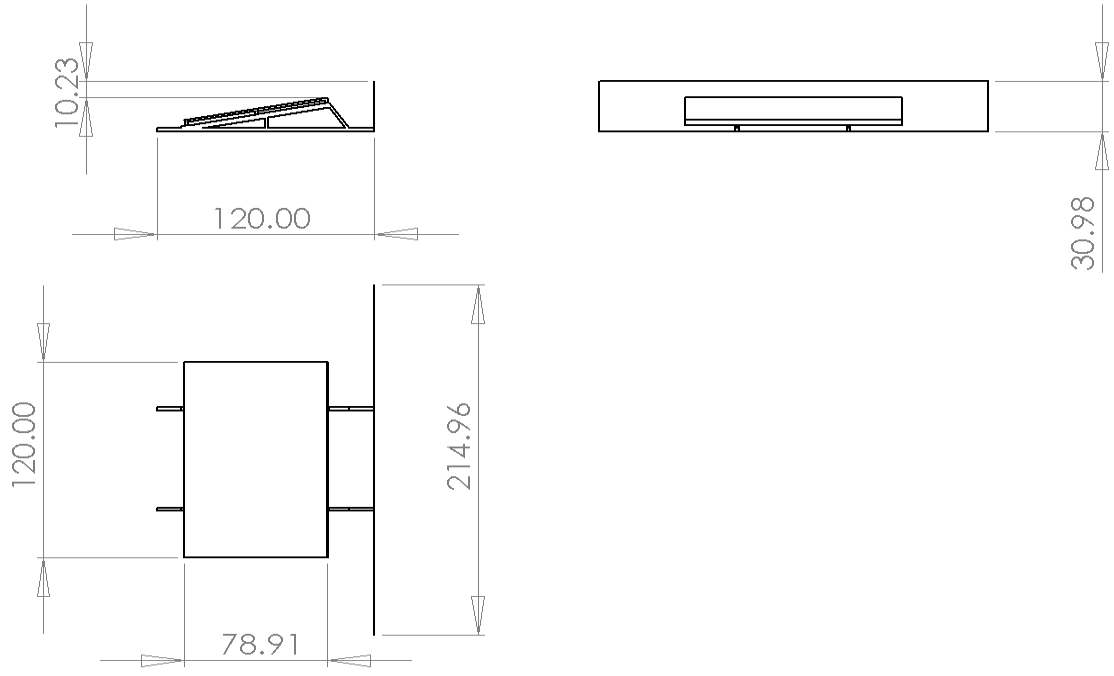

Figure A.7 Detailed drawing of vertical wall deflector at an angle $\theta = 90^{o}$ from horizontal

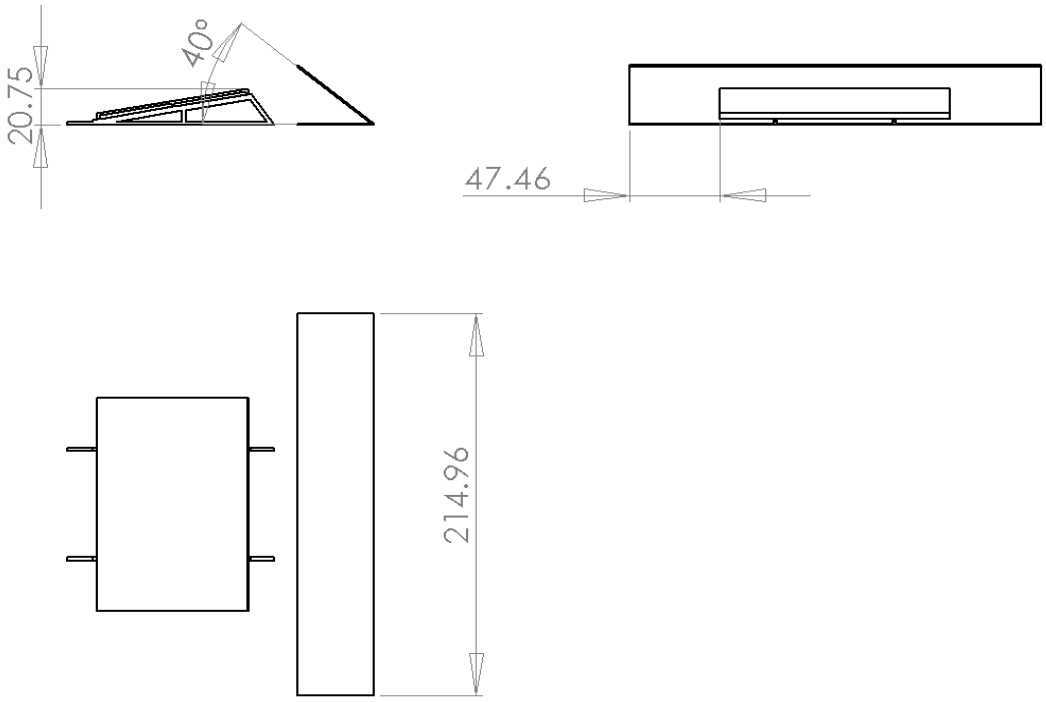

Figure A.8 Detailed drawing of inclined deflector at an angle $\theta = 40^{o}$

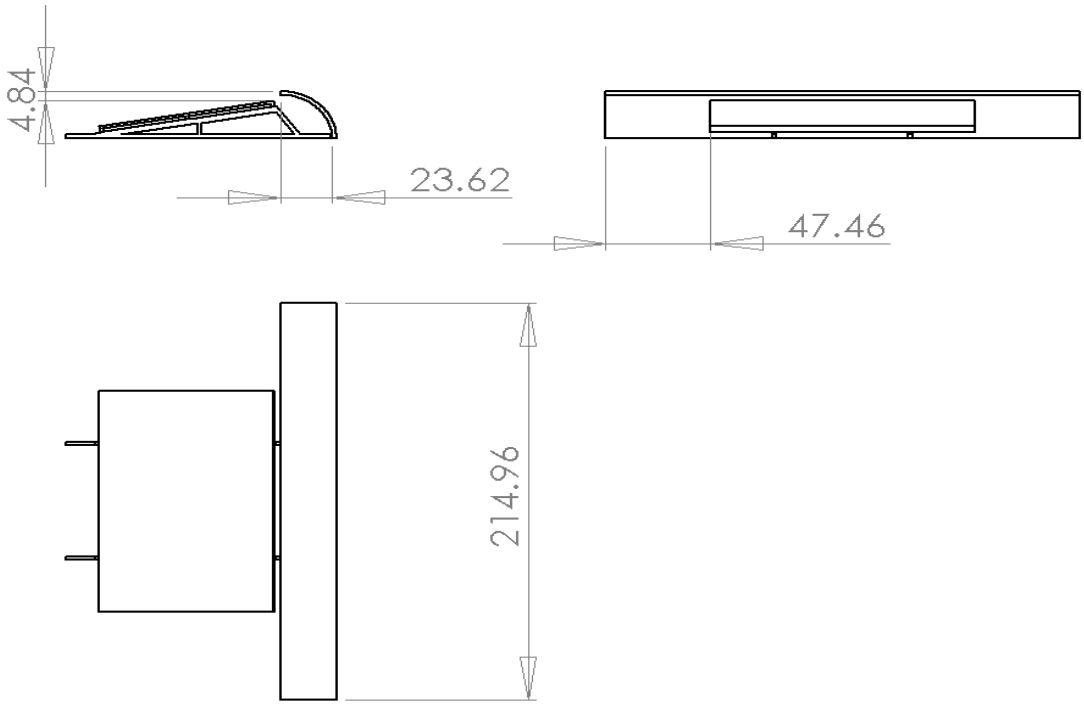

Figure A.9 Detailed drawing of full scale rack with quarter circle deflector

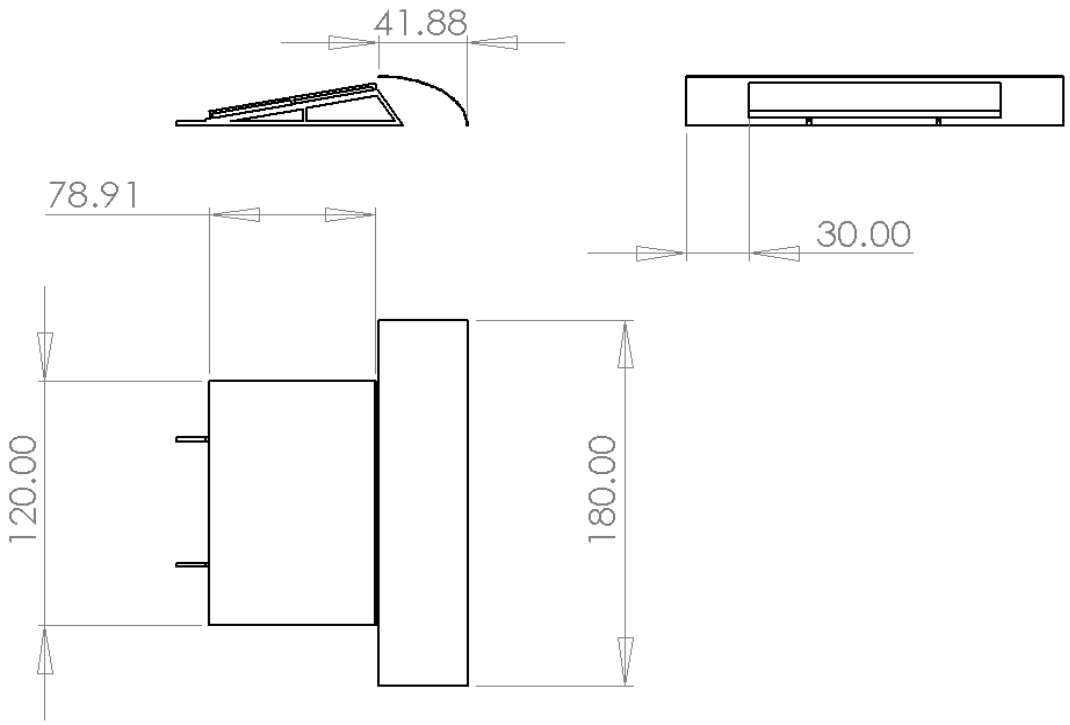

Figure A.10 Detailed drawing of full scale rack with elliptic deflector

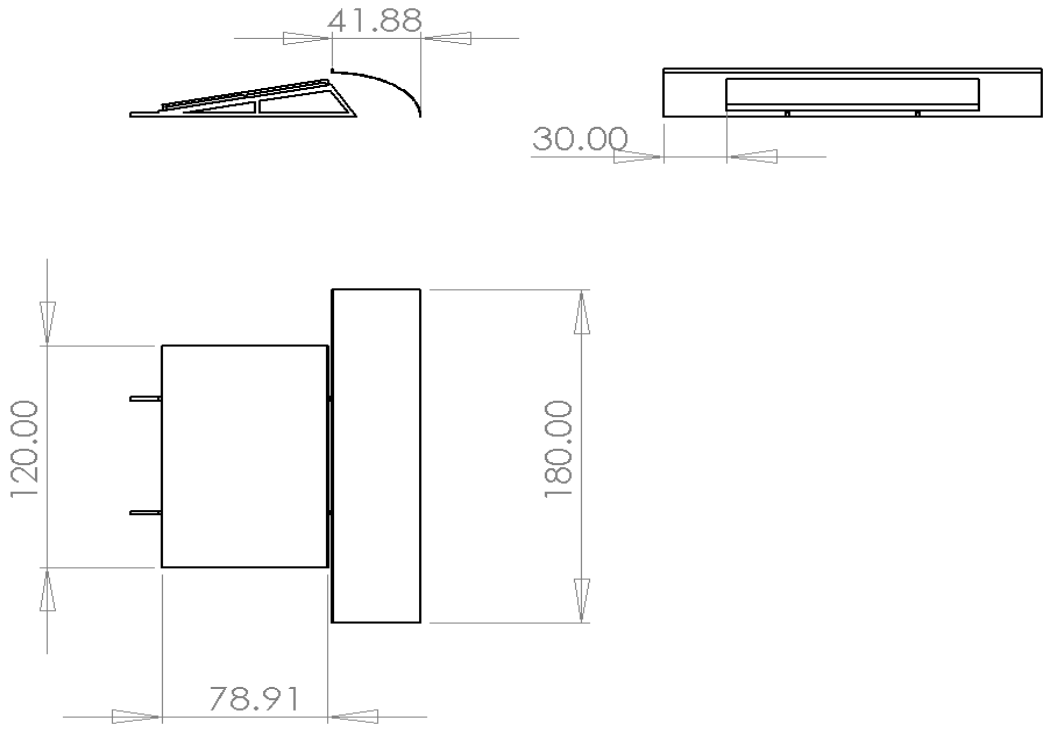

Figure A.11 Detailed drawing of full scale rack with elliptic deflector with 2” lip

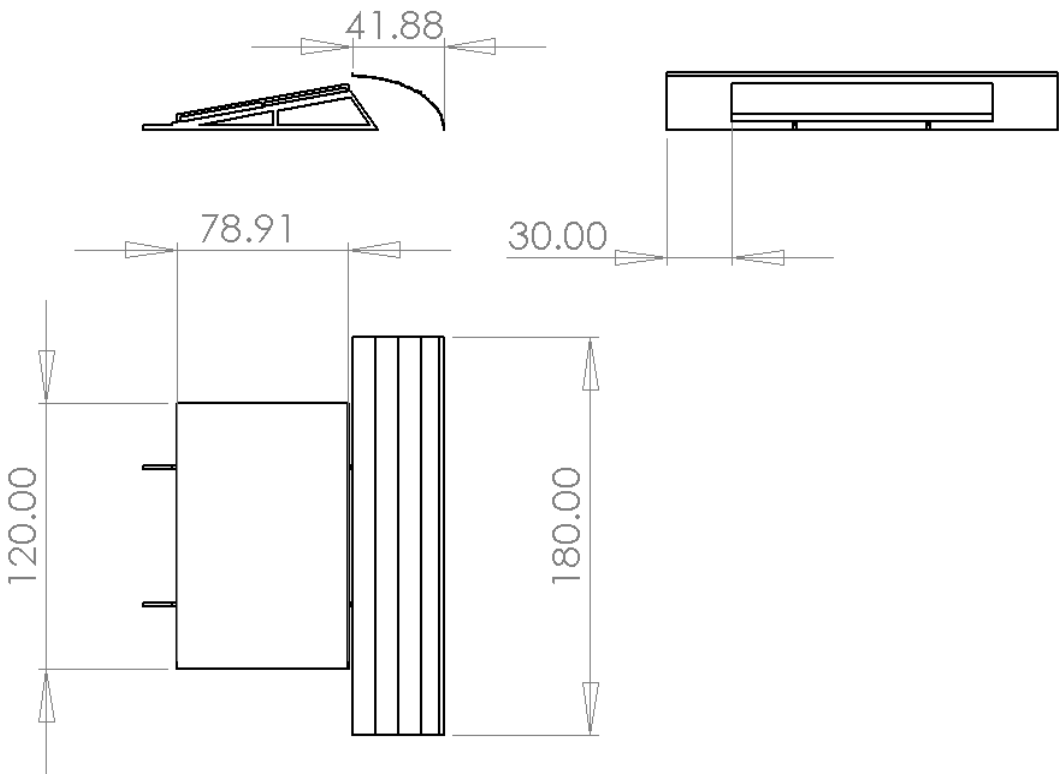

Figure A.12 Detailed full scale rack with elliptic deflector with 2” lip and fins

A.2 Results from Computational Simulations

Figure A.13 Mesh structured in 2D-full-scale 5 racks array with deflector arrangement (close-up

A.13 Mesh structured in 2D-full-scale 5 racks array with deflector arrangement (close-up included)

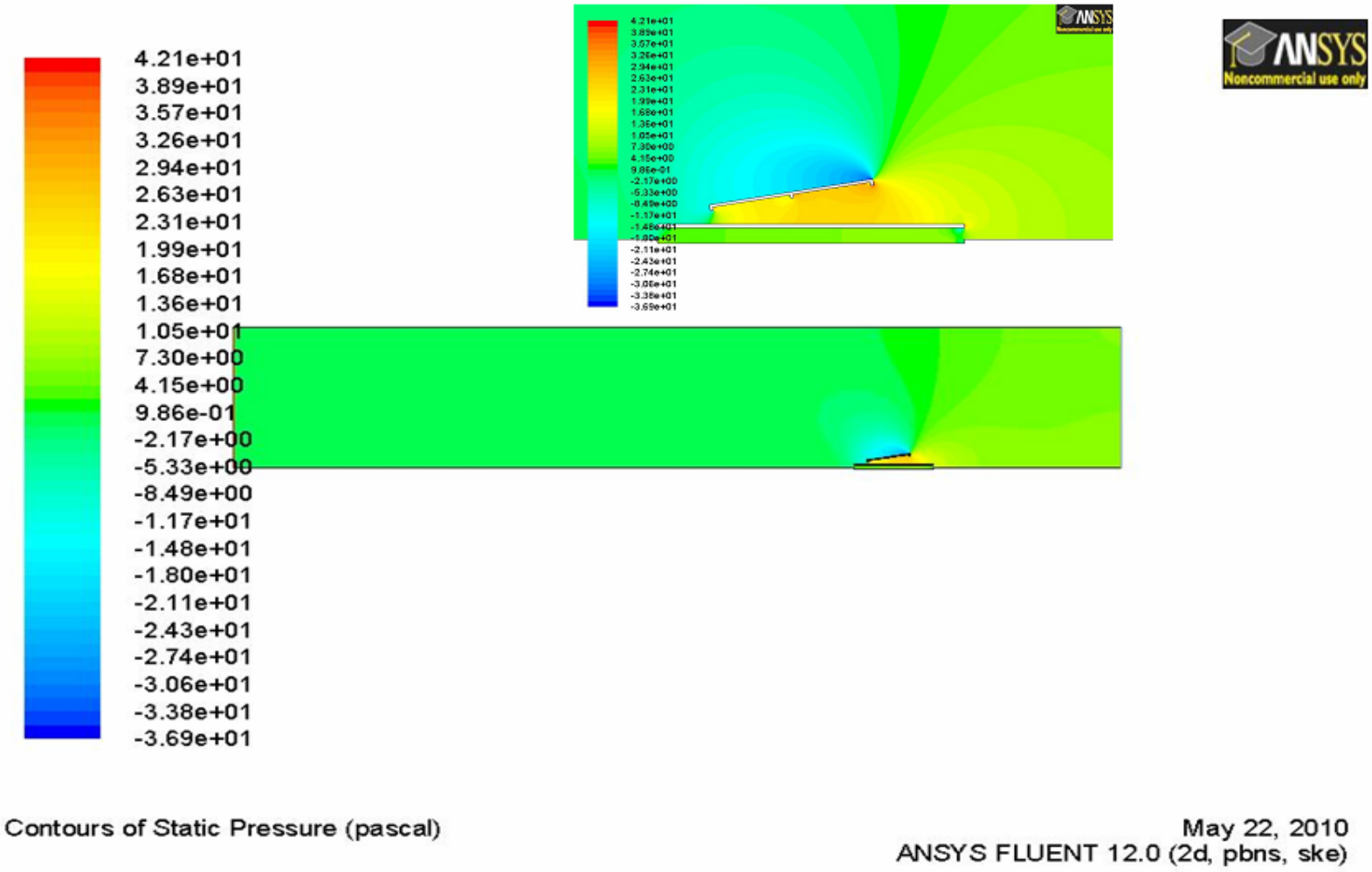

Figure A.14 Static pressure contours of quarter-scale single rack only arrangement (close-up included)

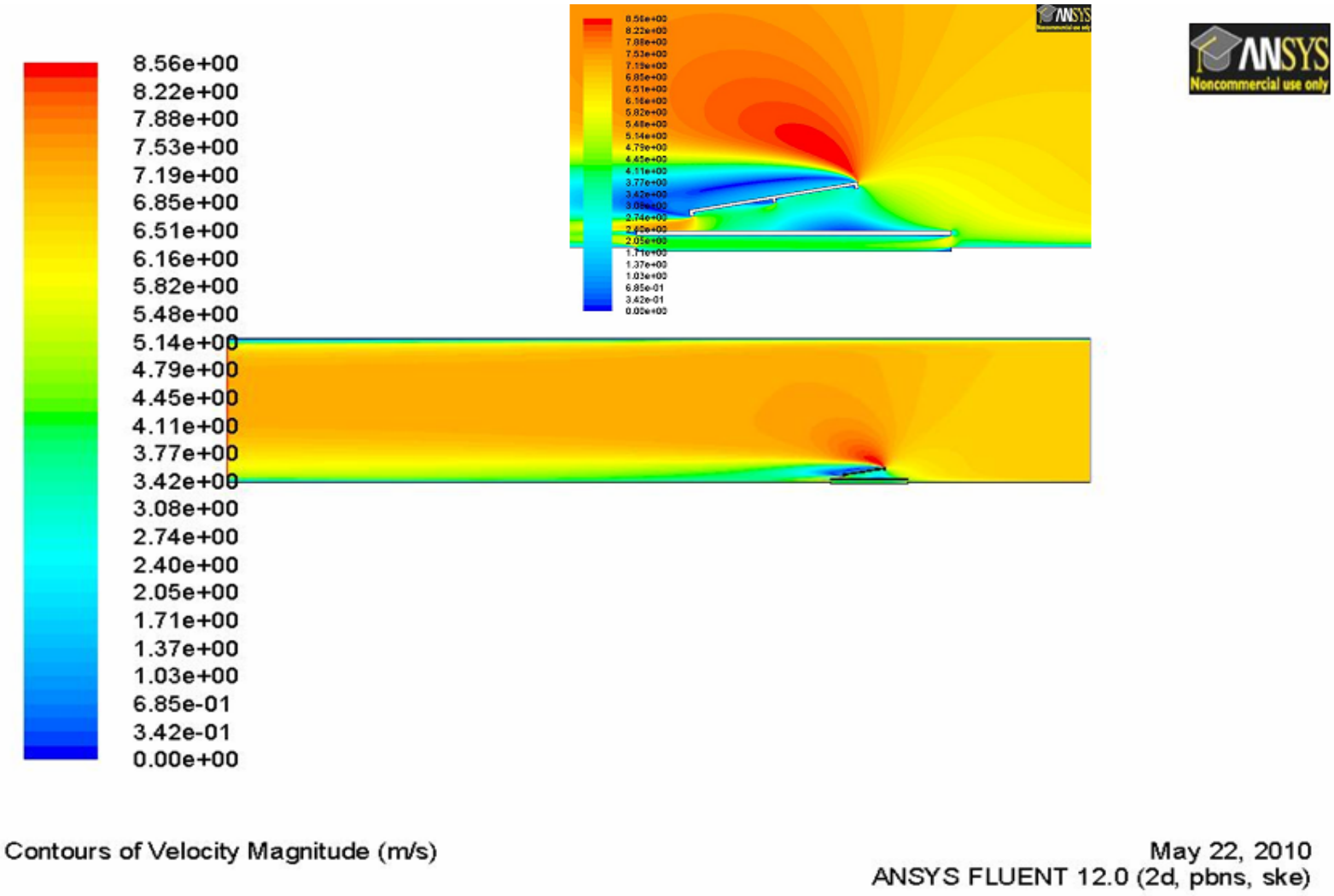

Figure A.15 Velocity contours of quarter-scale single rack only arrangement (close-up included)

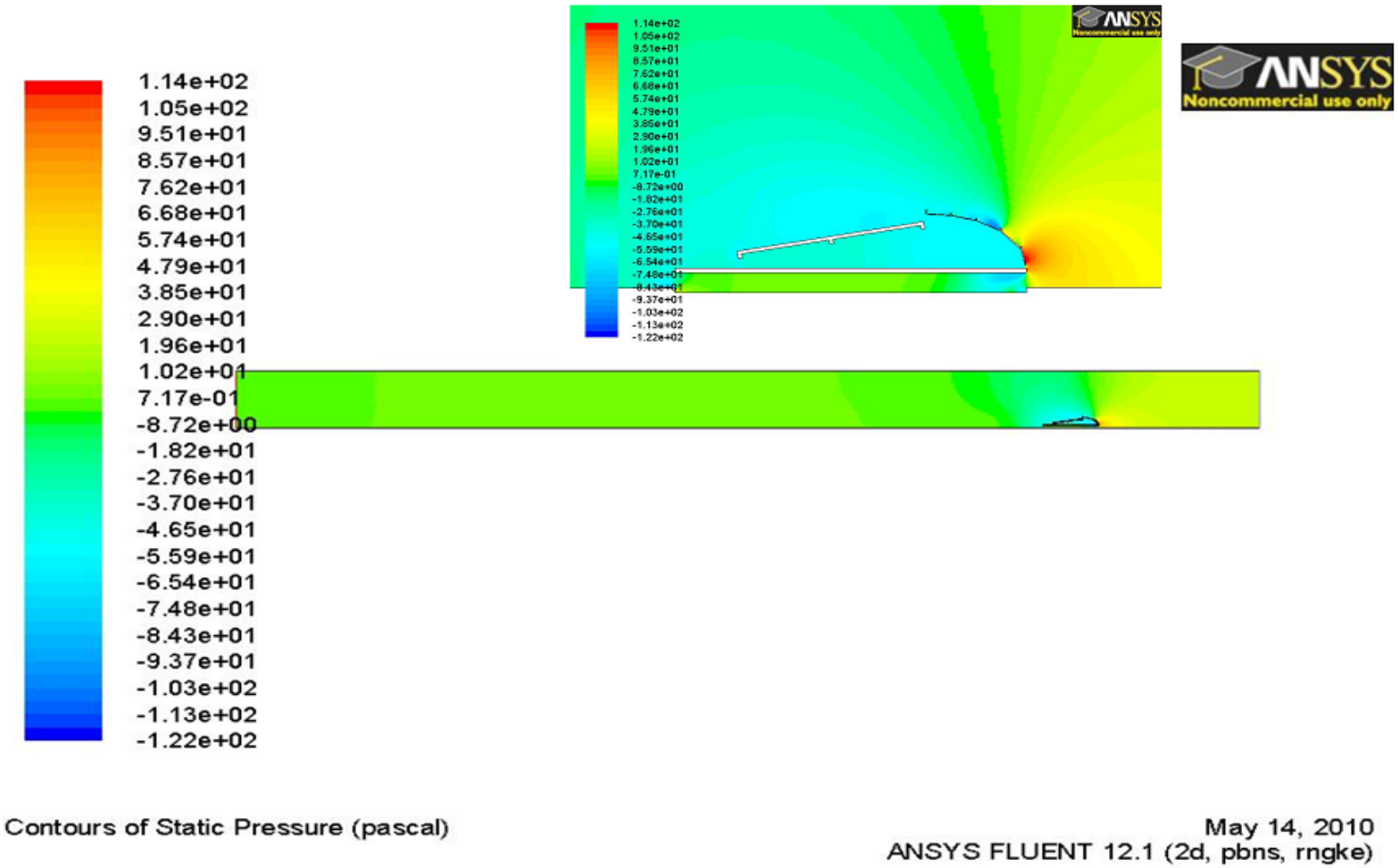

Figure A.16 Static pressure contours of quarter-scale single rack with deflector arrangement (close-up included)

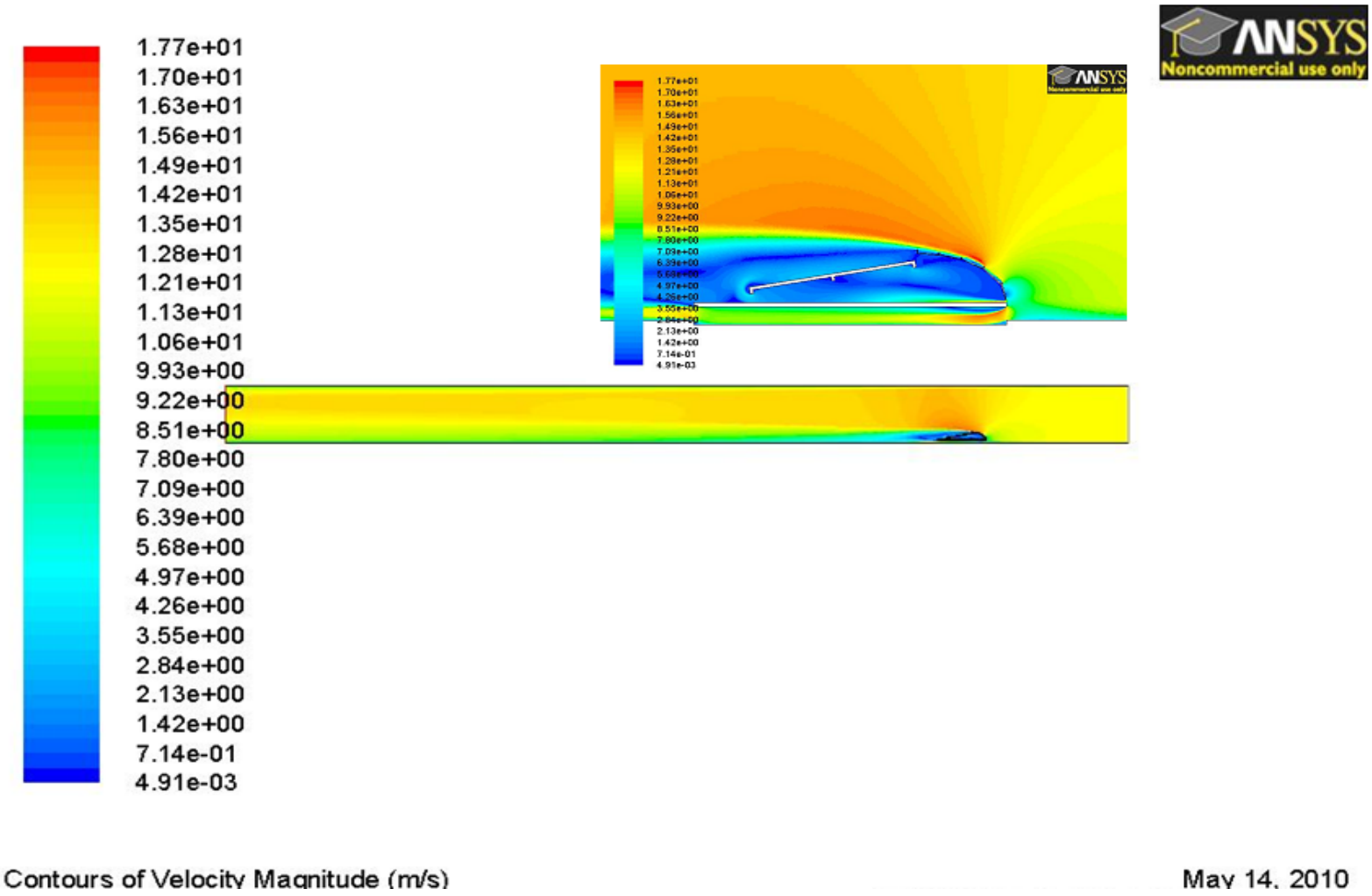

Figure A.17 Velocity contours of quarter-scale single rack with deflector arrangement (close-up included)

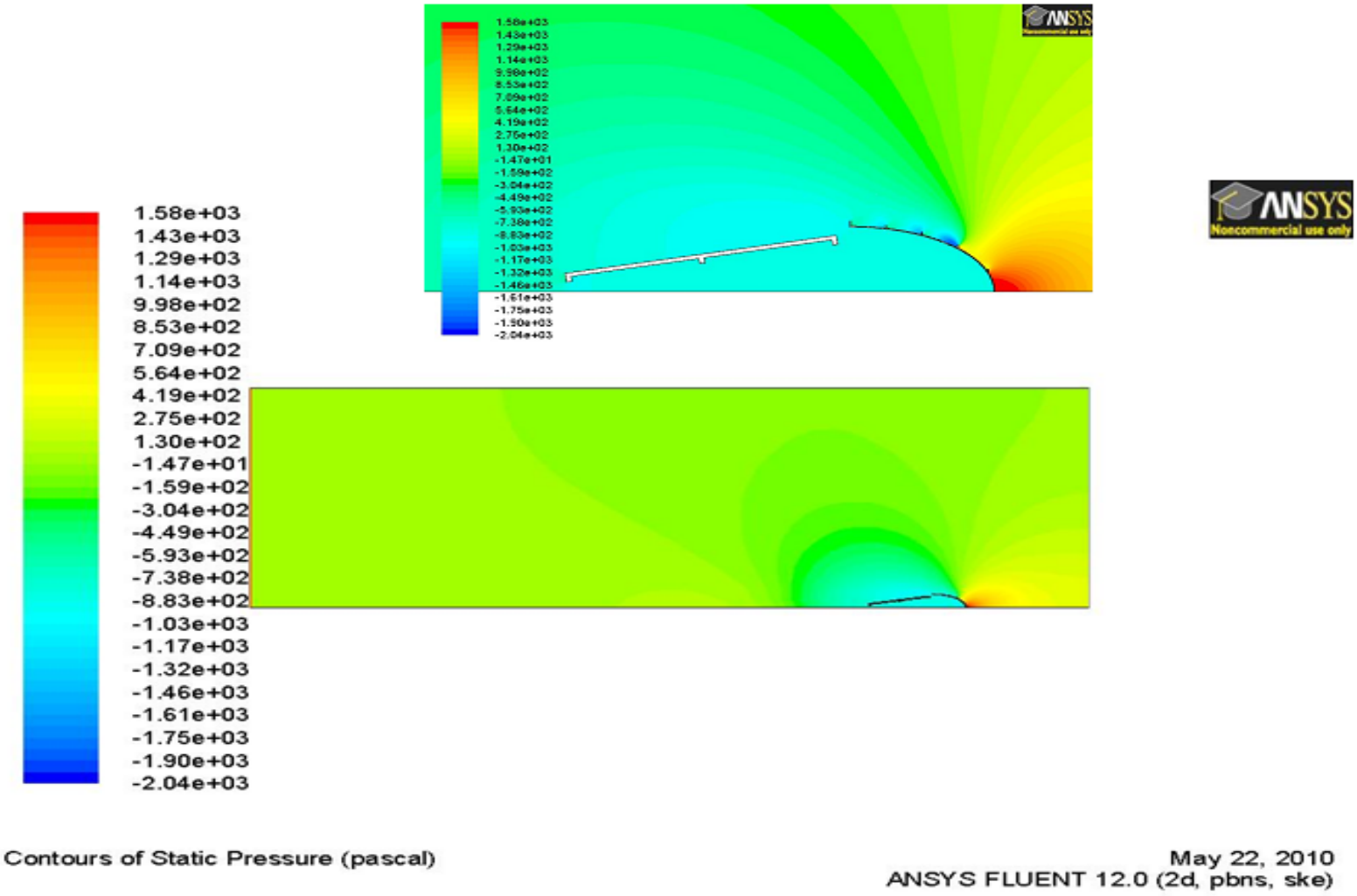

re A.18 Static pressure contours of full-scale single rack with deflector arrangement (close-up included)

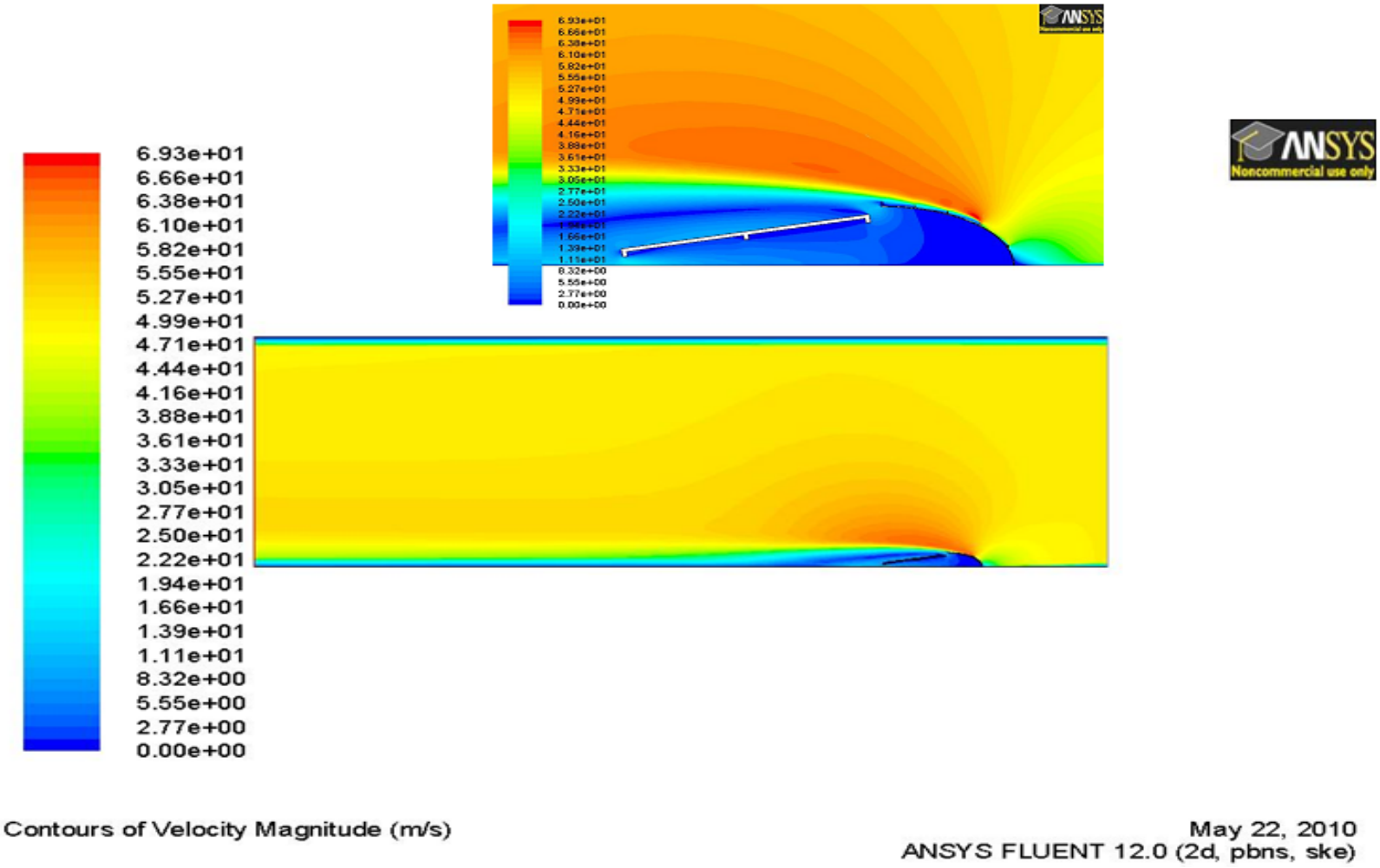

re A.19 Velocity contours of full-scale single rack with deflector arrangement (close-up included)

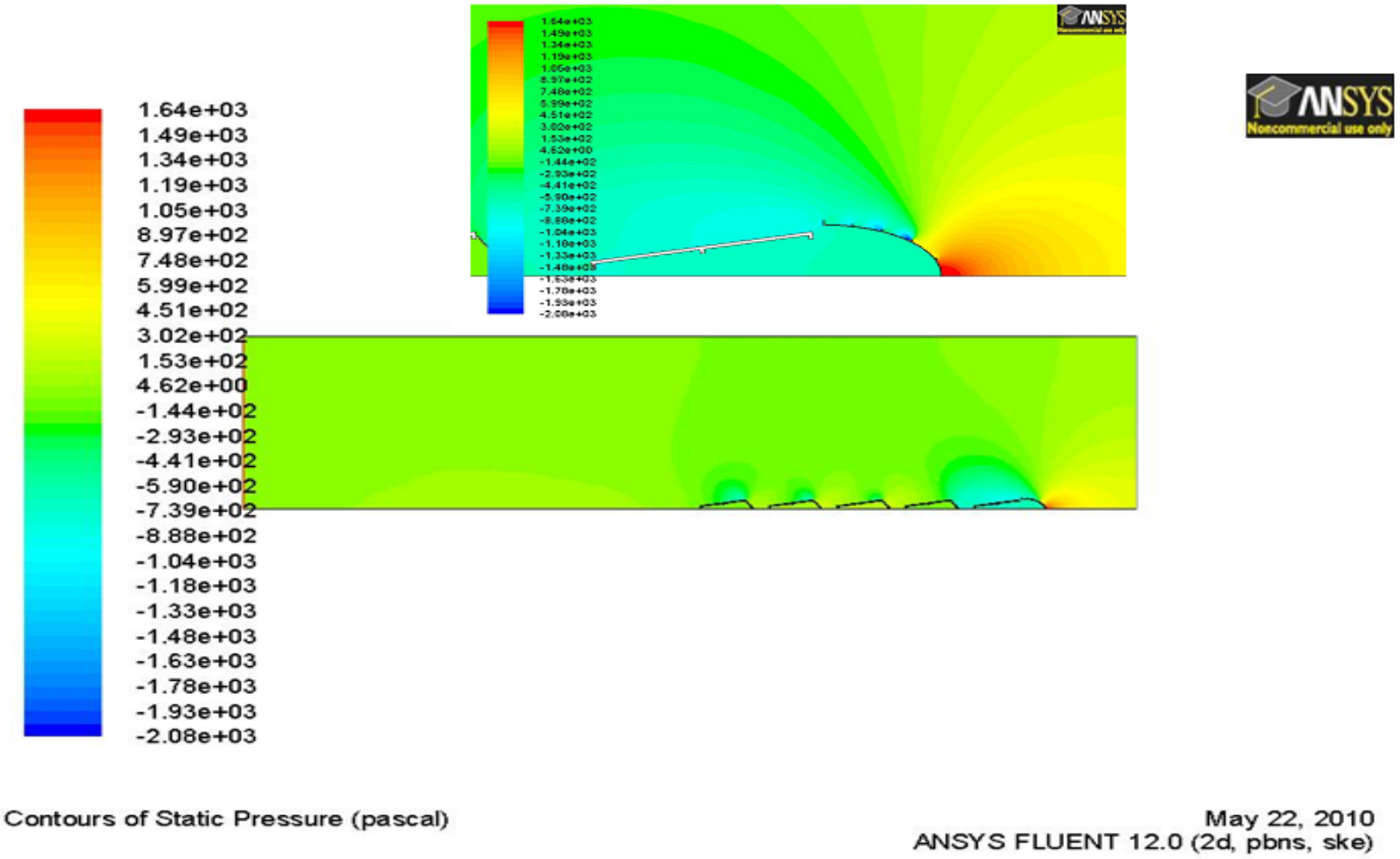

igure A.20 Static pressure contours of full-scale 5 racks array with deflector arrangement (close-up included)

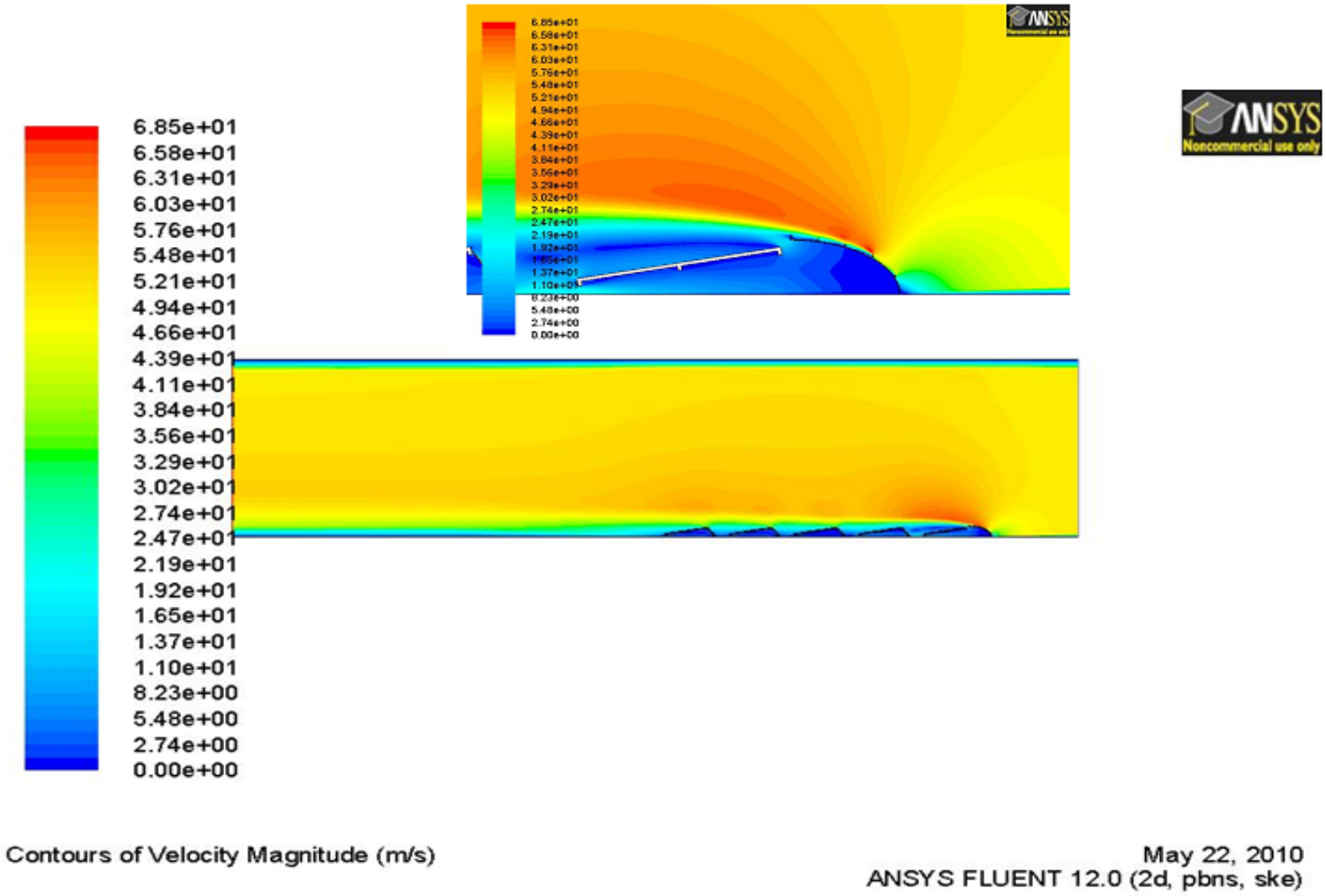

Figure A.21 Velocity contours of full-scale 5 racks array with deflector

A.21 Velocity contours of full-scale 5 racks array with deflector arrangement

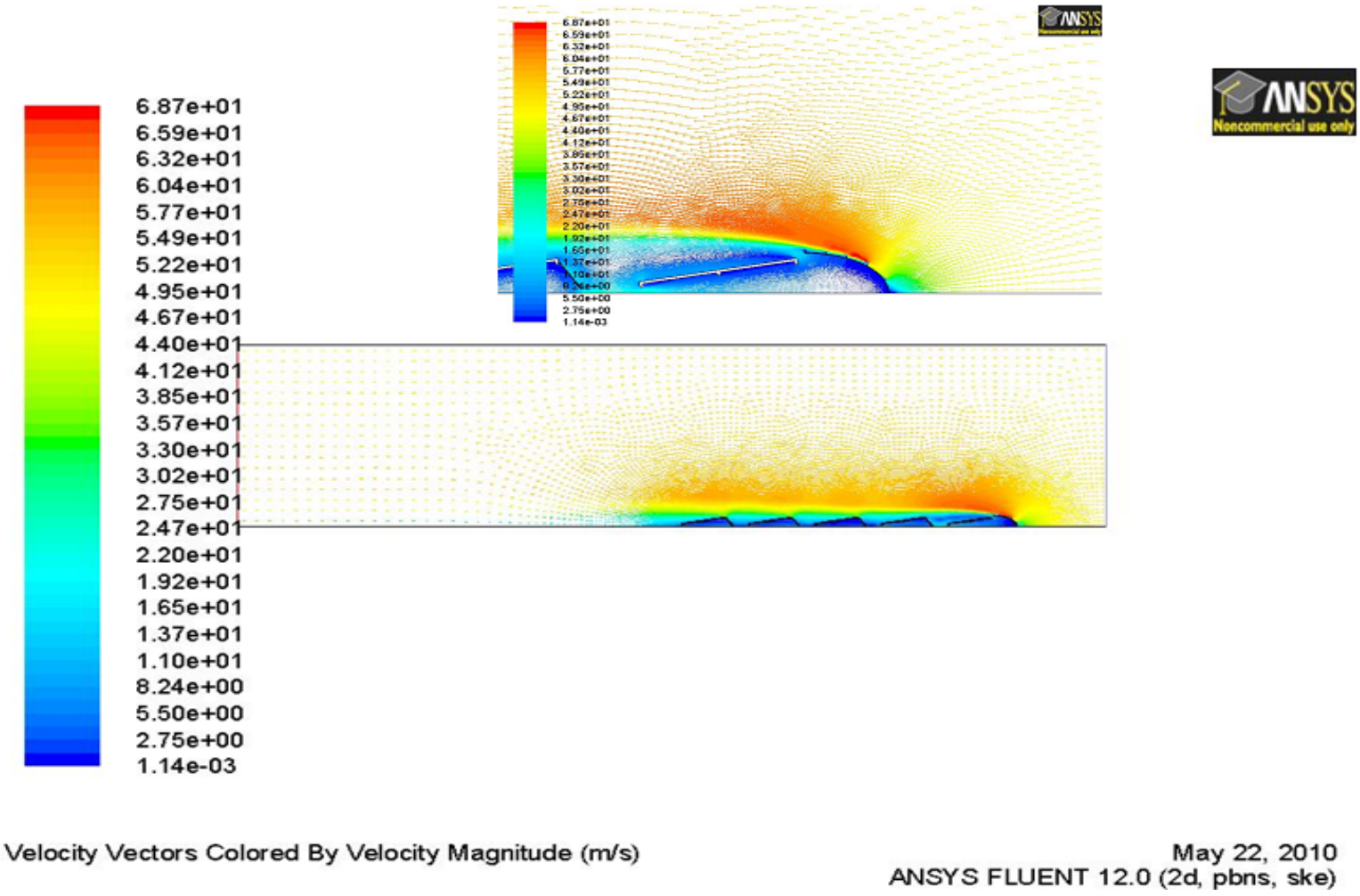

Figure A.22 Velocity vectors of full-scale 5 racks array with deflector arrangement (close-up

A.22 Velocity vectors of full-scale 5 racks array with deflector arrangement (close-up included)

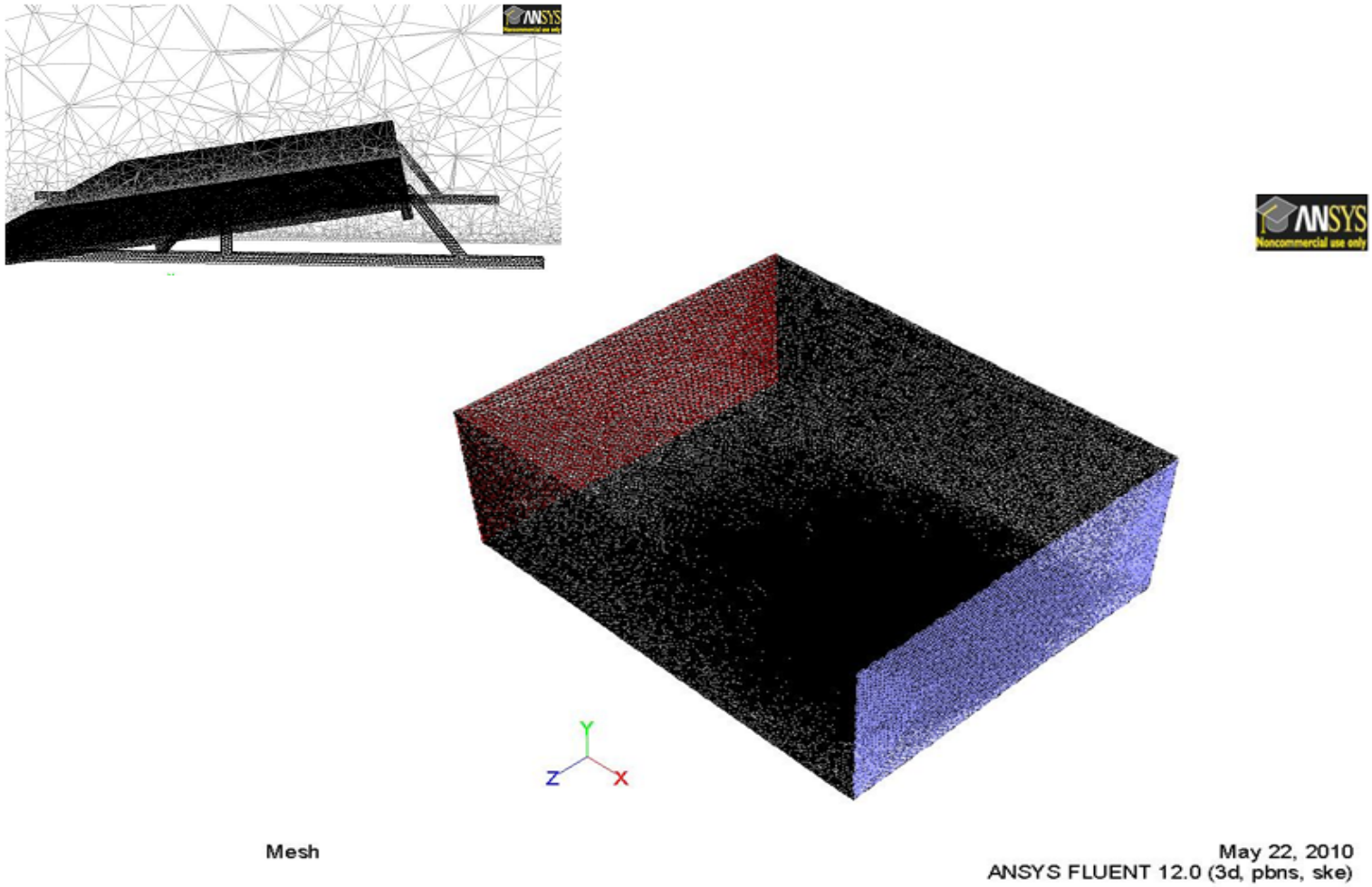

Figure A.23 Mesh structured in 3D-full-
A.23 Mesh structured in 3D-full-scale
Mesh structured in 3D-full-scale single

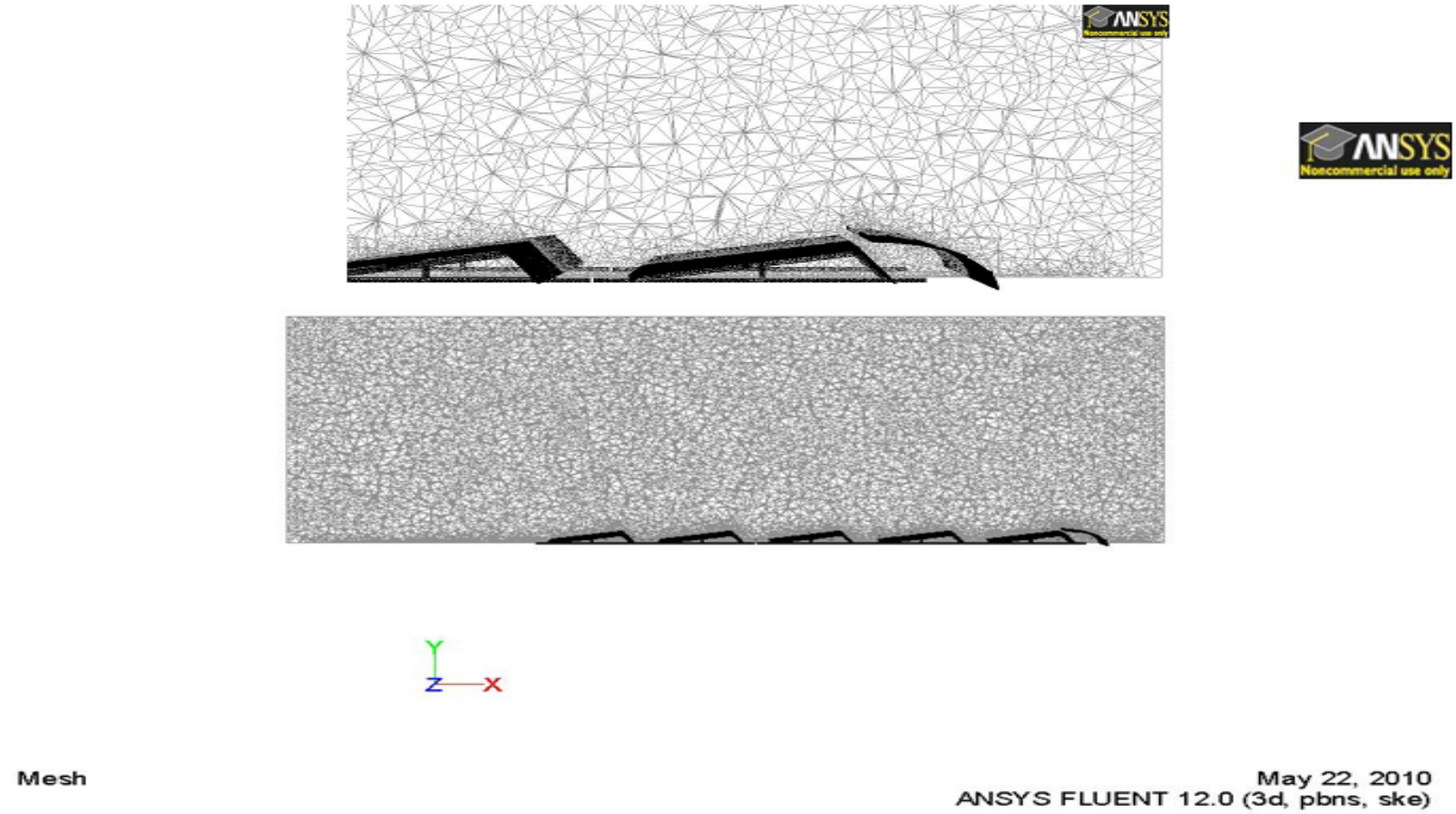

Figure A.24 Mesh structured in 3D-full-scale 5 racks array with deflector arrangement (close-up included)

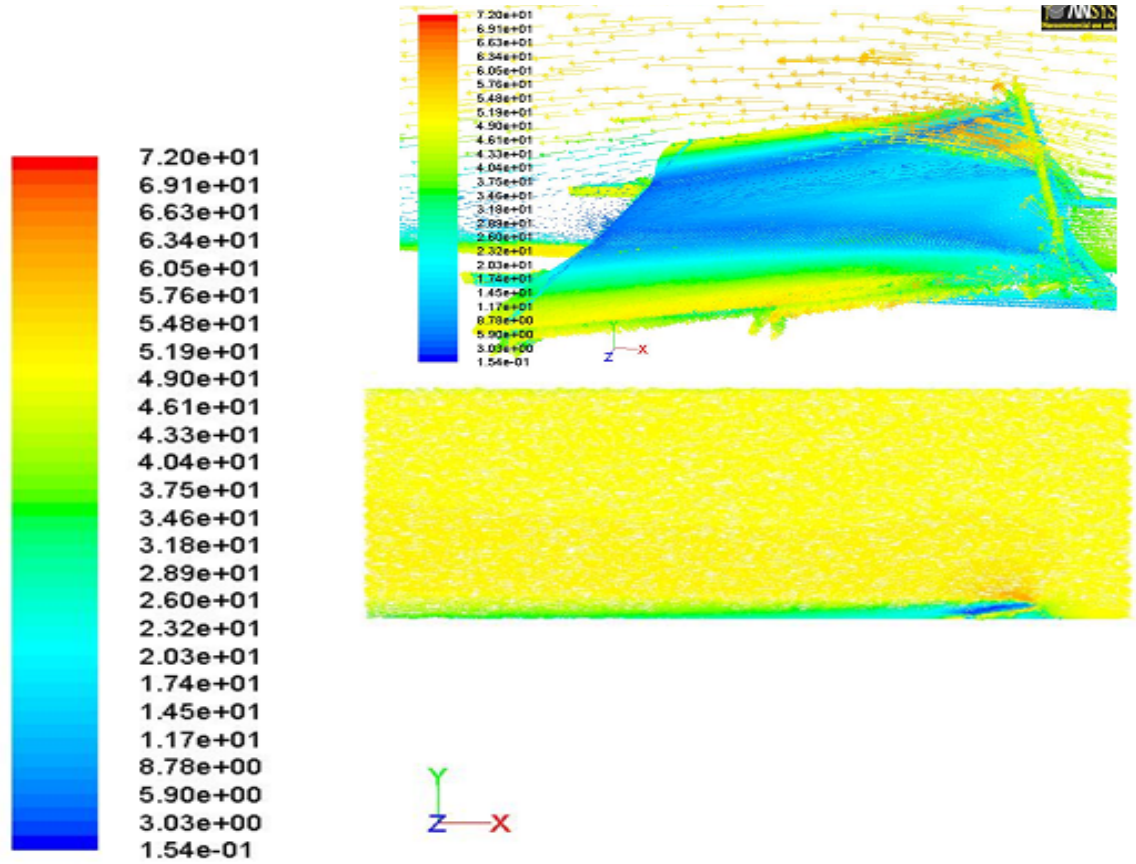

Figure A.25 Velocity vectors of full-scale single

e A.25 Velocity vectors of full-scale single rack only

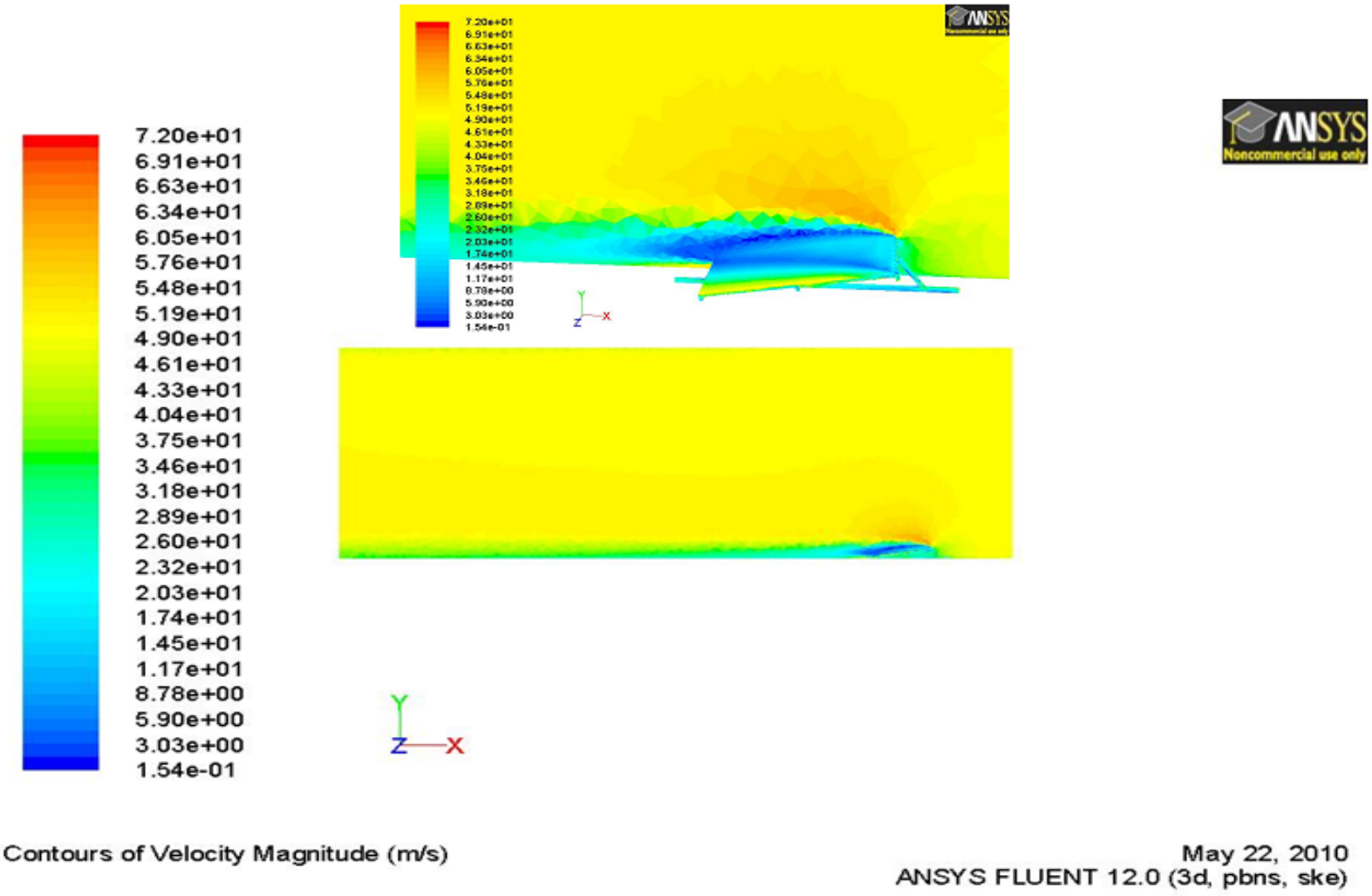

Figure A.26 Velocity contours of full-scale single rack

e A.26 Velocity contours of full-scale single rack only

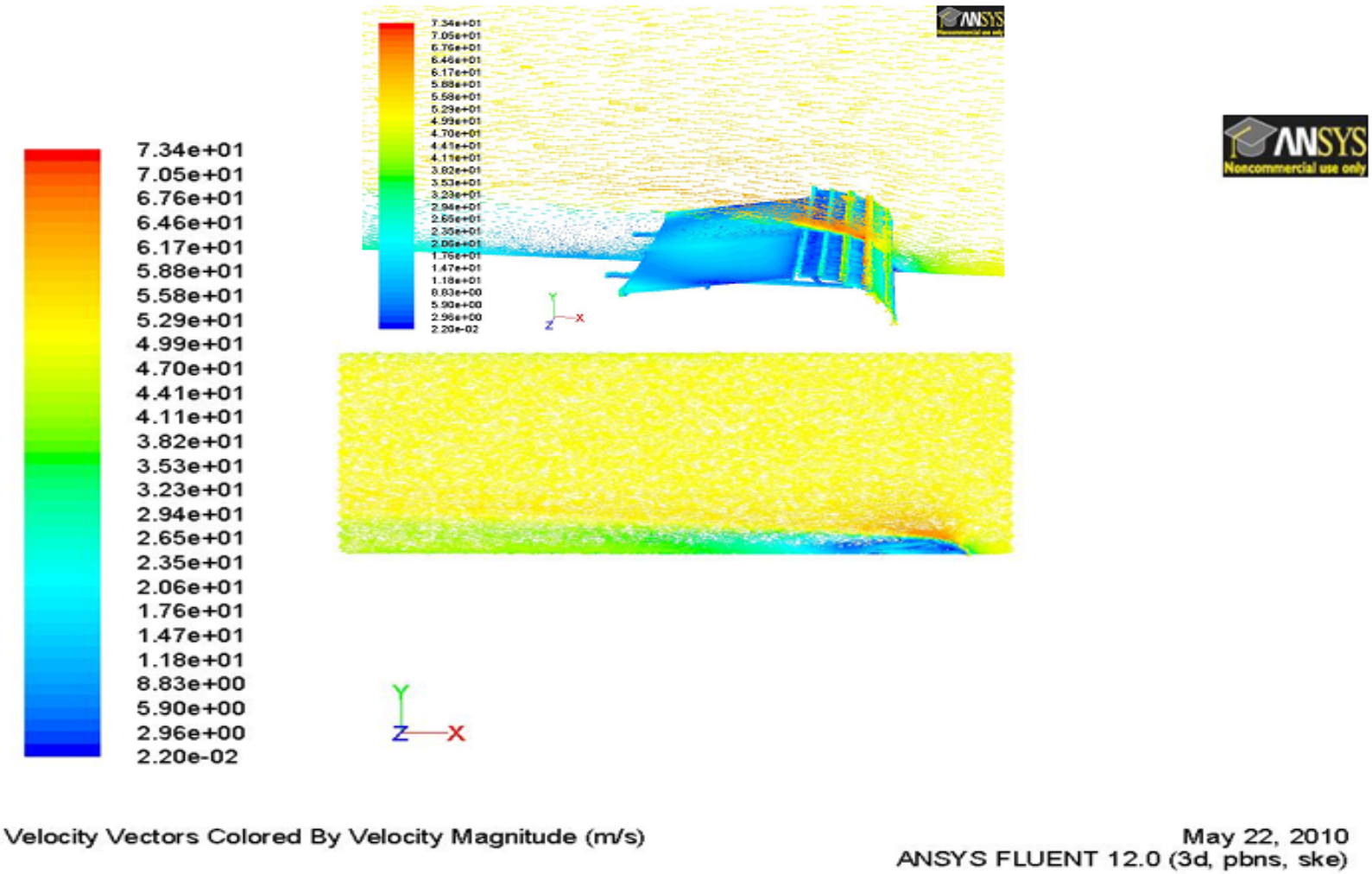

Figure A.27 Velocity vectors of full-scale single rack with deflector arrangement (close-up

A.27 Velocity vectors of full-scale single rack with deflector arrangement (close-up included)

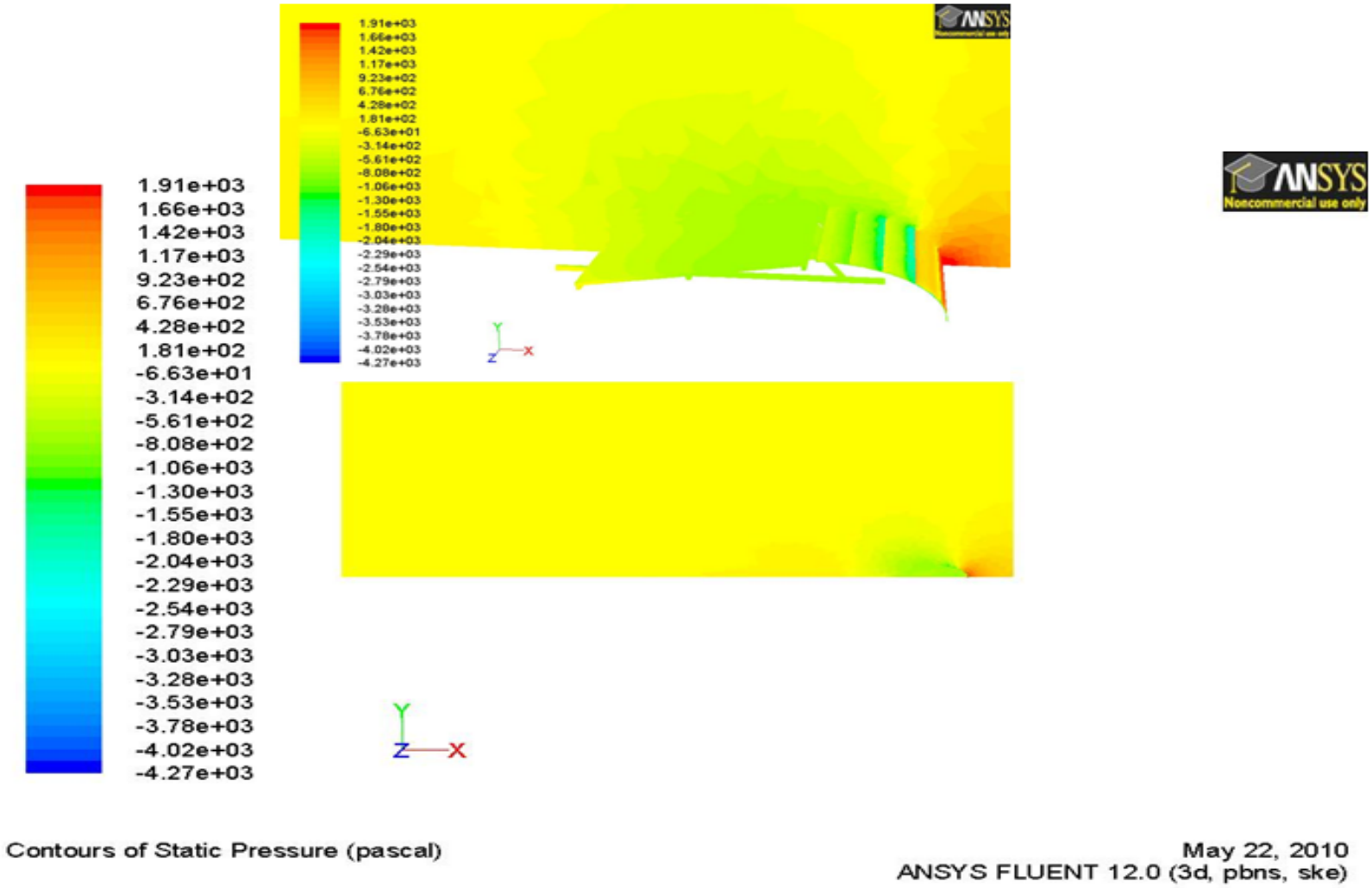

Figure A.28 Static pressure contours of full-scale single rack with deflector arrangement (close-up included)

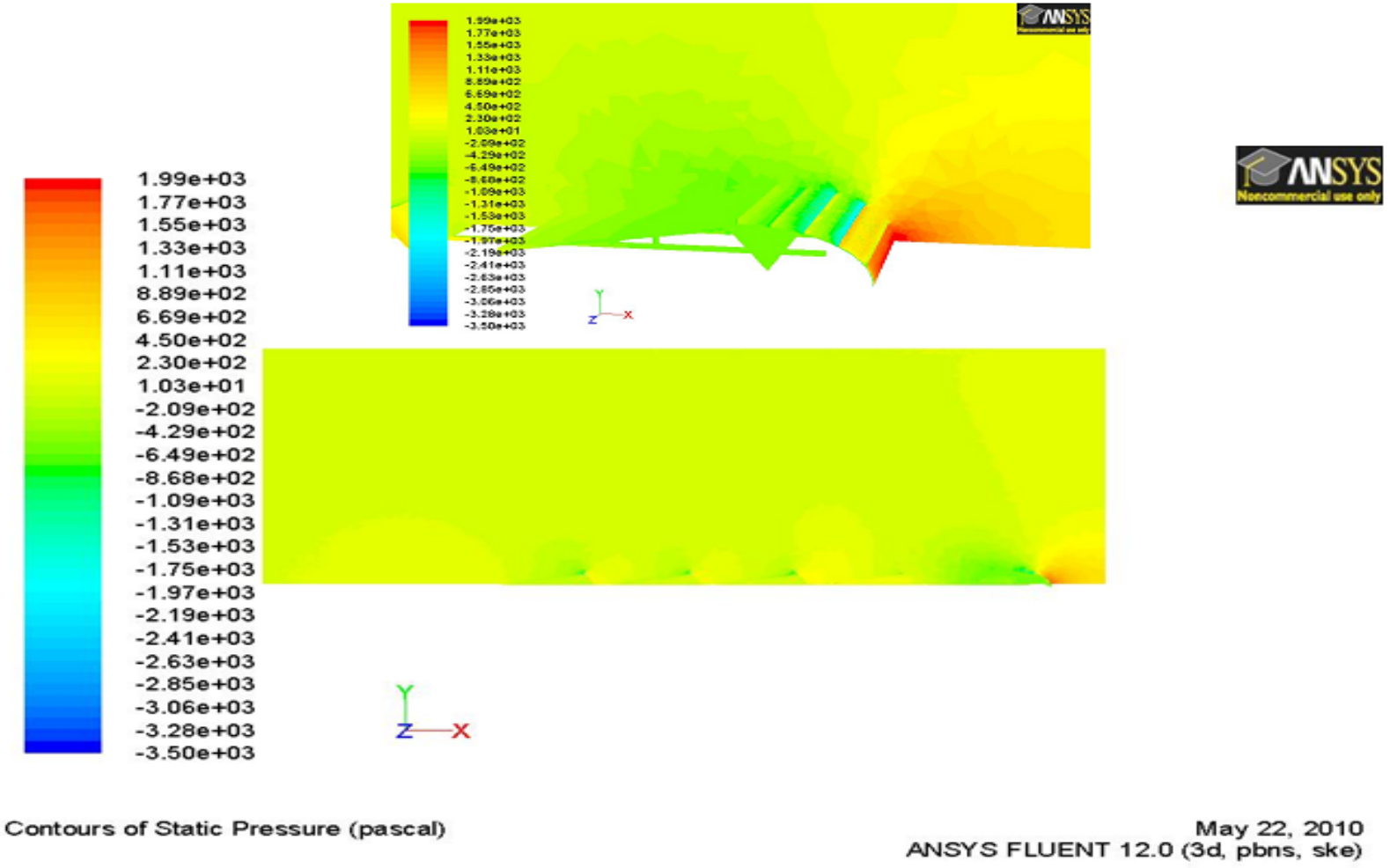

Figure A.29 Static pressure contours of full-scale 5 rack array with deflector arrangement (close-up included)

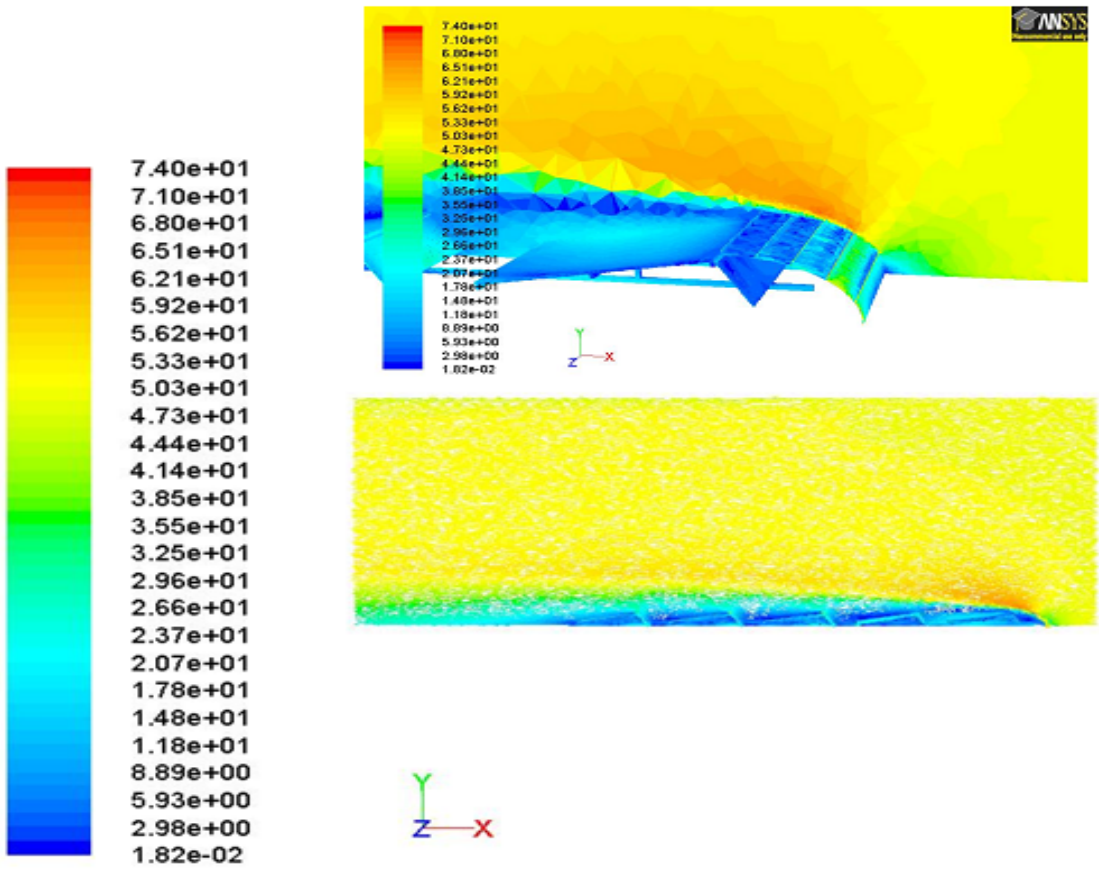

Velocity Vectors Colored By Velocity Magnitude (m/s)

May 22, 2010
ANSYS FLUENT 12.0 (3d, pbns, ske)

rack array with deflector arrangement (close-up included)